COMPUTER VISION ALGORITHM DEVELOPMENT AND BIOMEDICAL APPLICATIONS

by

VASANT KEARNEY

Presented to the Faculty of the Graduate School of

The University of Texas at Arlington in Partial Fulfillment

of the Requirements

for the Degree of

DOCTOR OF PHILOSOPHY IN BIOMEDICAL ENGINEERING

THE UNIVERSITY OF TEXAS AT ARLINGTON

May 2016

ACKNOWLEDGEMENTS

A number of people helped contribute to the work contained within this dissertation. I would first like to acknowledge my supervisor, Dr. Liping Tang, and all his post docs and graduate students, especially Dr. Jun Zhou, Yihui Huang, and Ashley Dacy.

I would also like to acknowledge my co-supervisor, Dr. Weihua Mao, and all of his post docs, Dr. Tsuicheng Chiu, Dr. Honghuan Liu, Dr. Lan Jiang. I would also like to thank some of the clinical medical physicists and radiation oncologists at UT Southwestern Medical Center, Dr. Susie Chen, Dr. Xuejun Gu, Dr. Jing Wang, Dr. John Yordy, and Dr. Lucien Nedzi.

I would like to acknowledge my committee members, Dr. Hanli Liu, Dr. Baohong Yuan, and Dr. Ashwin Nair, for playing an important role in shaping the structure and content of this dissertation.

ABSTRACT

COMPUTER VISION ALGORITHM DEVELOPMENT AND BIOMEDICAL APPLICATIONS

VASANT KEARNEY, PhD

The University of Texas at Arlington, 2016

Supervising Professor: Liping Tang and Weihua Mao

This study focuses on the development and analysis of novel computer vision algorithms for biomedical applications. Chapter 2 focuses on developing a 2D Canny edge-based DIR algorithm to register in vivo white light images taken at various time points. Using a mouse model, the accuracy of the canny edge-based DIR algorithm was tested using evaluation metrics, a ground truth synthetic scenario, and fluorescent gamma analysis. The results indicate that the Canny edge-based DIR algorithm performs better than all other algorithms.

Chapter 3 focuses on the development of a novel longitudinal fluorescent signal tracking algorithm using an *in vivo* mouse model. To test the accuracy of the fluorescent signal tracking algorithm, confined mutual information was used. The results indicate

that the automated fluorescent temporal implantation tracking algorithm performs better then rigid registration and DIR algorithms on tracking fluorescent signals *in vivo*.

Chapter 4 aims to develop a 3D serial sectioning method to track the dispersion of model drugs via slow release devices in various ocular implantation sites. To achieve this, an automatic retinal delineation algorithm was developed and tested. The automatic sectioning algorithm was shown to be significantly indistinguishable from manual retinal sections. 3D serial sectioning retinal drug dispersion can be accurately modeled automatically.

Chapter 5 is devoted to developing an automated landmark-guided deformable image registration (LDIR) algorithm between the planning CT and daily cone-beam CT (CBCT) with low image quality. The accuracy of the LDIR algorithm has been evaluated on a synthetic case and data of six head and neck cancer patients. The results indicate that LDIR performed better than all other algorithms.

In general, all of the above computer vision solutions help improve upon, mimic, or automate the human visual system for biomedical applications.

TABLE OF CONTENTS

LIST OF ABBREVIATIONS

Abbreviations	Term
DIR	Deformable Image Registration
CT	Computed Tomography
MRI	Magnetic Resonance Imaging
PET	Positron Emission Tomography
SPECT	Single Photon Emission Computed Tomography
SIFT	Scale-Invariant Feature Transform
LSA	Local Small Area
DVF	Deformation Vector Field
IC Demons	Intensity Dorrected Demons
Canny DIR	Canny Deformable Image Registration
RMSE	Root Mean Square Error
NMI	Normalized Mutual Information
FSIM	Feature Similarity Index Metric
EPO	Erythropoietin
CY5	Cyanine5
M1	Mouse 1
M2	Mouse 2
AMD	Age-Related Macular Degeneration
OCT	Optical Coherence Tomography
PNIPAM	Poly-N-Isopropylamide
FITC	Fluorescein Isothiocyanate
CUDA	Compute Unified Design Architecture
NLSD	Normalized Least Squared Differences
SSD	Sum of Squared Differences
CR	Completely Randomized
IV	Intravitreal
AS	Cornea/Anterior Sub-tenon
SC	Subconjunctival
ST	Sub-Tenon
CBCT	Cone Beam Computed Tomography
HU	Hounsfield Unit
GPU	Graphics Processing Units
LDIR	Landmark-Guided Deformable Image Registration
LSV	Local Small Volume
AP	Anterior-Posterior
SI	Superior-Interior

DECLARATION OF ACADEMIC ACHEIVEMENT

The research performed for this dissertation was conceived, conducted, analyzed, written, and submitted for publication primarily by the author of this dissertation with the following exceptions:

• All the mice in used in chapters 2 and 3 were handled, sacrificed, injected, implanted, and imaged primarily by Dr. Jun Zhou, Yihui Huang, and Ashley Dacy. Ashley Dacy and Dr. Jun Zhou, conducted most of the user feedback for MobileView and played major roles in the general direction and overall design of MobileView.

• In Chapters 4, all the rabbits were handled, injected, implanted, sacrificed by Dr. Hong Weng and the tissue images were taken by Dr. Yi-Ting Tsai. The general idea and overall end goal of chapter 4 was also developed by Dr. Yi-Ting Tsai.

• In Chapters 5, all the patient image sets were retrieved by Dr. Lan Jiang. The initial images were taken by Attending Physicians', Dr. Susie Chen, Dr. John Yordy, Dr. Lucien Nedzi. Dr. Susie Chen played a major role in the qualitative assessment of the deformed contour propagation. Dr. Xuejun Gu developed the original GPU based Demons algorithms.

CHAPTER 1

1. Introduction

1.1. Central Theme

The human visual system is well suited for biomedical image processing [1]. Our visual system can recognize and identify morphological nuances in the presence of shading, variable lighting, reflection, refraction, distortion, low contrast, motion, distance, and obfuscation [2]. However, there are drawbacks when relying on the human visual system for image processing, such as reproducibility, speed, and in some cases cost [3-5]. Over the past 25 years, biomedical engineering has become increasingly reliant on machine vision for image processing tasks [6]. Machine vision incorporates intensity, gradient, frequency, and phase information to access morphological, structural, and positional information about an image [7]. In a related yet separate field, computer vision has been developed which incorporates methods for processing and acquiring images. Computer vision focuses on understanding real world high dimensional data in an effort to produce symbolic or numerical interpretations, that manifest in the form of decisions [8-11]. A theme in the development of this field has been the transformation of visual images into a finite set of descriptions about the real world, which can then be used to drive aided decision making or fully automated decisions.

Fields such as radiation therapy, diagnostic imaging, and chemotherapy heavily rely on computer vision, in the clinic or during research and development. Understanding the distribution and accumulation of drugs within a small animal model or

during treatment of a human patient, is an essential part of chemotherapy. In diagnostic imaging, the formation of meaningful 3D imaging data can be derived from one dimensional RF signals for MRIs, 2D orbiting x-ray projections for CT, and 3D subtraction data in angiography. All of these methods rely on the use of geometry, statistics, learning theory, or physics models to disentangle symbolic information from image data [12].

The field of radiotherapy is particularly reliant on machine vision giving the potential occupational danger during treatment delivery. Patients are often isolated during the treatment process, while the clinician remains safe behind a radiation barrier. A robotic radiation delivery machine is then guided through a treatment protocol through the use of a priori or on-board imaging systems. Computer vision helps the treatment machine deliver radiation dose to the intended targets within the patient.

Computer vision often incorporates a class of mathematical solution strategies known as optimization [13, 14]. Often, the complex computational nature of biomedical imaging protocols renders them ill-conditioned for numerical solutions [15-17]. Because of this, computer vision problems are often cast into optimization routines, and solved inversely [18-20]. This style of image processing is useful in a wide variety of image matching algorithms such as morphological matching and deformable image registration (DIR) [21, 22].

3D biomedical imaging problems are inherently challenging for manual human processing [23, 24]. The human visual system is capable of 3D analysis but must do so in a disjoint manner. Humans can only view 2D segments of an image and must interpret

the 3D structure using lighting, shading, depth, and transparency effects [25-27]. Machines can directly store and perform analysis of any order of dimensionality, allowing them to overcome the 2D barrier that the human visual system suffers from [28]. This memory architecture enables 3D biomedical imaging methods, including 3D rendering of serial sectioning, and CT DIR algorithms. This work uses computer vision's computational architecture, while simultaneously mimicking features of the human visual system, to solve biomedical imaging problems.

My thesis work can be broken up into 4 studies which are all comprised of one central theme. All studies incorporate computer vision and optimization strategies to solve biomedical image processing problems for drug delivery modeling, small animal in vivo longitudinal tracking, and clinical radiation oncology inter-fractional motion management.

1.2. Overview of the Chapters

Chapter 1 is an overview of computer vision, and it describes how the individual problems associated with each chapter relate to the central theme.

Chapter 2 is devoted to tracking the time evolution of anatomical changes that occur between imaging fractions using an in vivo small animal model. White light images are used to derive structural information changes. These structural changes are used to infer functional changes between imaging fractions. This strategy allows for non-invasive, non-ionizing, structural anatomical motion tracking throughout time.

Chapter 3 focuses on multiple implantation site tracking throughout time. Structural motion information derived from study 1 is used to facilitate implantation tracking, in the presence of diffusion and migration of the fluorescent tracers. Morphological similarity matching is used to quantize the dynamic functional changes that are decoupled from their corresponding structural motion. A signal extraction technique, derived from near-neighbor implantation tail estimation, is used to estimate the implantation delineation, in the presence of multiple implantation sites.

Chapter 4 maps the drug delivery distribution of nanoparticles within the eye using an *ex vivo* model. Automatic tissue segmentation of the various anatomical structures of the eye are used to extract the drug distribution spatially and temporally, throughout many days using serial sectioning. This model allows for quantification of drug accumulation in various tissues throughout time and allows for a deeper understanding of the drug release and drug distribution behavior amongst various delivery methods.

Chapter 5 automatically accounts for the anatomical deformation that occurs between radiotherapy treatment fractions. An optimization routine embedded in a computer vision protocol is implemented to retrospectively track the changes that happen in a patient's body, such as weight, tumor size, and patient set up error. This information can be used either as part of an adaptive radiotherapy protocol or to retrospectively evaluate the quality of a delivered treatment course. This study is designed to fit into the adaptive radiotherapy paradigm shift that is currently underway in radiation oncology.

Each chapter is formatted and structured according to their respective target journals. Chapter 5 was published in *Physics in Medicine and Biology*, chapter 4 and chapter 2 will be submitted to peer reviewed journals. A manuscript is in preparation for Chapter 3. A target journal will be determined at a later time. The content within chapters 2, 4, and 5 are near exact replicates of material published in, or soon to be submitted to, their respective peer review journals [29, 30]. Some of the ideas in this dissertation are derived in part based off previous work not mentioned explicitly in this dissertation [31-37].

CHAPTER 2

WHITE LIGHT DEFORMABLE IMAGE REGISTRATION

2.1 Introduction

Optical imaging systems are a crucial modality for observing *in vivo* functional changes. Optical imaging techniques have emerged to track organ system responses to endogenous or exogenous changes. Small animal optical imaging *in vivo* models are often used to test drug accumulation, drug response, toxicity, metastatic behavior, tumor progression/regression, changes in metabolism, and inflammatory response [38, 39].

In vivo imaging modalities that are non-invasive are often preferred for small animal longitudinal studies [40]. Generally, non-invasive imaging systems can be divided into structural and functional modalities. Structural modalities provide anatomical and morphological information, such as computed tomography (CT), magnetic resonance imaging (MRI), white light optical imaging, and ultra sound. Whereas functional modalities, such as positron emission tomography (PET), single photon emission computed tomography (SPECT), and optical imaging (fluorescence and bioluminescence), provide biological molecular activity information. All of these imaging modalities come with their own unique blend of advantages and limitations.

Micro CTs can have high spatial resolution and fast acquisition times [41]. However CTs, can be expensive and are associated with increased hazards, such as ionizing radiation exposure [42]. To achieve high contrast and spatial resolution large photon fluences are required which leads to high integral radiation dose for the subject,

which can affect the immune system and potentially influence the outcome of some *in vivo* studies [43-45]. MRIs can produce high quality 3D images without the use of ionizing radiation. However, MRIs can have long image acquisition times, suffer from low spatial resolution, require special electromagnetic shielding, and are expensive [46]. To achieve high spatial resolution while simultaneously preserving good signal to noise rations, long slice acquisition times are required. Ultrasound imaging techniques can acquire images at high image acquisition frequencies. However, ultrasound imaging can be cumbersome to use during in vivo imaging procedures. Also, high spatial resolution, low contrast, full small animal imaging can be challenging with this modality [47]. White light imaging techniques are non-ionizing, very low cost, easy to mobilize, and have fast image acquisition times. However, white light imaging techniques are limited to surface information, and are sensitive to lighting and shading variations [48]. For these reasons, white light imaging modalities are not currently used for quantitative longitudinal studies.

PET scanners have been developed for use in small animals. However, in order to obtain high spatial resolution with high signal contrast, high radiation doses are needed, which have the potential to damage healthy tissues [49]. High costs and additional regulation due to the presence of radioactive tracers are also factors for PET imaging. SPECT is similar to PET in its use of a radioactive γ-ray tracer material but are much cheaper than PET scans, as longer half-life radionuclides can be used. Fast acquisition times are possible with SPECT, allowing for cardiac or respiratory image gating. However, since SPECT does not rely on coincidence timing, it suffers from poor spatial resolution (about 1cm), which makes SPECT not suitable for small animal imaging [50].

Optical imaging using fluorescence or bioluminescence can have fast acquisition times and achieve high spatial resolution [40]. Optical imaging modalities do not rely on radioactive tracers so are subject to less stringent regulations. Fluorescent tracer molecules can be less costly and less biologically harmful than their radioactive counterparts. An optical imaging small animal model can be made portable with greater ease than PET or SPECT imaging modalities [51]. However, optical imaging techniques can only image near surface signals and must rely on reconstructive techniques for 3D localization [52].

To help facilitate cross institutional collaboration, commercial demonstration, and proof of principal modeling, portable multimodal structural and functional imaging systems have begun to gain attention [51]. As the demand for portable imaging systems has increased, low cost optical imaging modalities have become increasingly attractive [53, 54]. However, it is currently very difficult conduct longitudinal quantitative optical imaging-based studies as anatomical mapping from day to day is challenging [55].

In order to track inflammatory responses, immunological behavior, or metastatic behavior, images must be assessed at various time points along a span of time sufficient to characterize the time dependent biological event. To quantitatively measure signal and compare it in a meaningful way, corresponding regions between images taken at different time points must be compared. To compare corresponding regions between images, structural information must be used as a surrogate to track functional information.

Conventional small animal *in vivo* tracking methods include direct voxel/pixel to voxel/pixel tracking based on intensity and gradient information or atlas matching, which

relies on an a-priori digital model [56-58]. The atlas matching method relies on iteratively deforming a digital mouse model to match simulated x-ray projections with measured x-ray projections. The deformations of the digital mouse are typically optimized using a steepest decent model until convergence is reached [59, 60]. This method has two major drawbacks, it relies on x-ray information which makes it unusable for a pure optical system and it will not meaningfully converge if the solution space of the optimization problem is non-convex [61]. Also, recalculating the simulated x-ray projections at every iteration is extremely computationally expensive, and thus very time consuming [62].

Another class of algorithms utilizes feature extraction methods for image registration. These methods rely on steepest decent optimization to minimize a non-linear least squares function [63]. This style of registration includes facial recognition, facial expression extraction, finger print identification, and palm print recognition. These distinct feature methods are all based on the scale-invariant feature transform (SIFT) method [64-67]. Local gradient information around each district feature is transformed into a representation that allows for high levels of local shape distortion and change in illumination. Using district features, as opposed to conventional deformable image registration (DIR) techniques, allows for less susceptibility to noise, and lighting variations. However, distinct feature extraction techniques currently rely heavily on disjointed features, which causes sparsity in features within the image [68]. This is in part caused by a stability feature removal step, which helps ensure feature reliance. In the case of white light image registration, it is favorable to use complete edges of an image instead of using a scattered subset of features [69-75]. If each point along the

canny edge is treated as a feature, then edge continuity can be used for stability discrimination. The differences between the SIFT method and the canny edge feature extraction method is demonstrated in figure 2.3.

Figure 2.3. SIFT method (left). Canny edge feature extraction method (right).

Small animal white light based DIR is uniquely challenging, as minor changes in the mouse's anatomical position can lead to big changes in shading and lighting. Similarly, features such as implantation swelling, and lesions on the skin can vary from day to day. Weight loss or weight gain can also make tracking the surface of a mouse difficult.

Conventional DIR algorithms using uniform grid based approaches can be error prone in regions with low contrast information such as the smooth surfaces on the skin or low quality regions of the image. However, strong features on the mouse skin surface such as the ridges of the spine, shoulders, ribs, and hind legs can often be seen even in the

presence of lighting, shading, and noise variation. Recently, a new form of non-grid based DIR algorithms have emerged, called Landmark-Guided DIR, which uses a sparse subset of points to deformably register noisy images [29]. This style of registration is well suited for images that have high noise contamination and large intensity inconsistencies between time points.

This paper demonstrates the feasibility of using canny edges, embedded in a sparse DIR framework, to overcome the challenges of small animal *in vivo* white light based anatomical tracking.

2.2 Methods and Materials

2.1.2 In Vivo Setup

All images were acquired using Progenitec's portable imaging device (Progenitec Inc., Arlington, Tx). White light and fluorescent images where acquired using a 50~100 um pixel size. Fluorescent images where obtained using a 635nm LED source at 30mA for 60 seconds.

7 *BALB*/c, 8-10 week old mice were subcutaneously injected with CY5 tagged EPO. CY5 is a near infrared fluorescent dye with an emission wavelength of 630-700nm [76]. All mice were imaged in prone position.

2.2.3 The Algorithm

A cross correlation based algorithm was used to rigidly register the image at time zero ($I_{stsatic}$) with an image acquired at a later time (I_{moving}). Once a rigid registration is determined, canny edges are generated on the I_{static} set [69, 72-74]. The canny edges are then separated using connected component analysis [77]. The separated canny edges can be seen in figure 2.4.

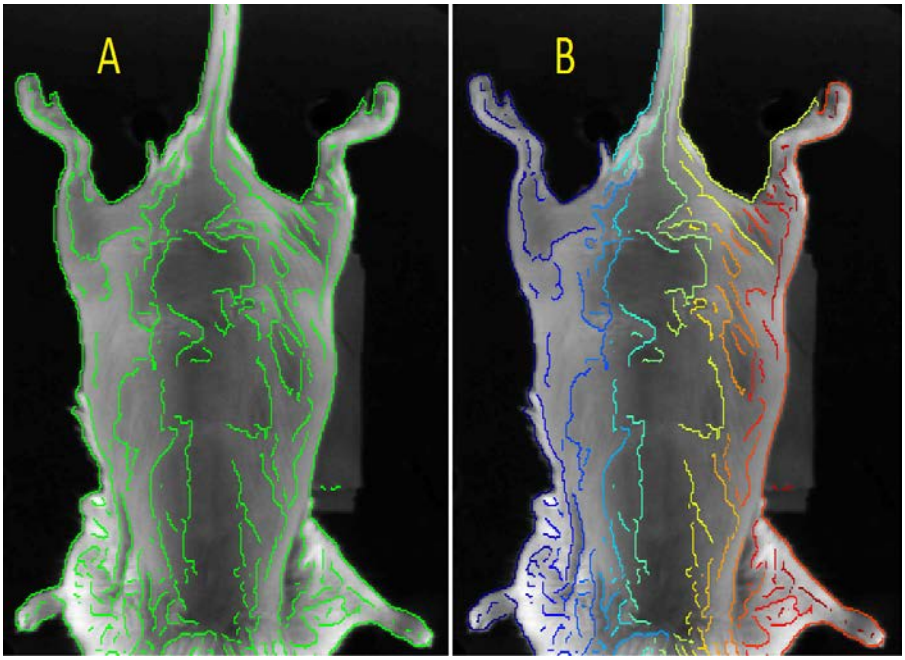

Figure 2.4. Canny edges superimposed on the static image (A). Color coded separated canny edges, are shown superimposed on the static image.

Each point (P) associated with the canny edges is used to match corresponding regions between I_{static} and I_{moving}, as these edges will all have strong gradient information associated with them. To help ensure that the canny edge does not represent noise, a line filtration algorithm is implemented. The line (L) must be above a certain length α. Once

a set of filtered canny edges is defined, a local small area (LSA) around each P on the static image LSA_{static} is defined with an initial size of 500μm x 500μm. Each LSA is registered to a corresponding area on the moving image LSA_{moving}. A optimization scheme is implemented to determine the optimal (i,j) shift of each LSA_{moving} until $E(i, j)$ is minimized for every P, where

$$E(i, j)^P = \left\| (\nabla LSA_{static} - \nabla LSA_{moving}^{i,j})^2 (LSA_{static} - LSA_{moving}^{i,j})^2 \right\|$$
$$i^P, j^P = \arg\min E(i, j)^P$$

The set of offsets i^P and j^P are then tested for stability. The deformation vectors at all points along an individual canny line are tested for smoothness by comparing neighboring offsets. If $\left| i^p - i^{p\pm1,2} \right|$ or $\left| j^p - j^{p\pm1,2} \right|$ is greater than δ than the p^{th} point is considered unstable and is subsequently removed. Figure 2.5 shows the original set of control points derived from the canny edge, with the corresponding stable set of control points.

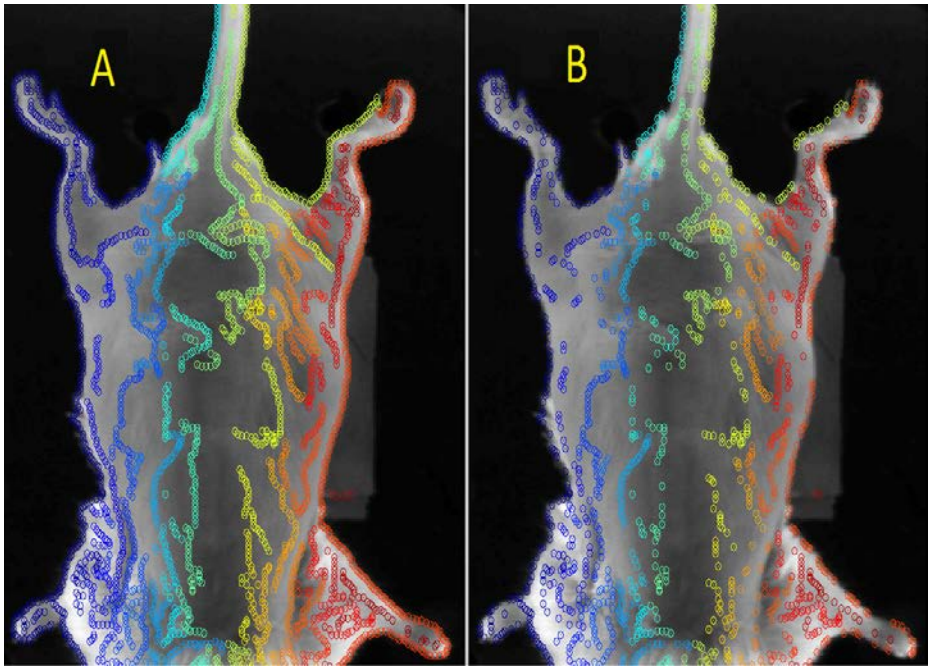

Figure 2.5. The original set of all points are shown (left). The stable set once all the unstable points have been removed (right).

The new set of stable offsets i^P and j^P are used to populate the complete 2D deformation vector field (DVF). To populate the DVF, the convex hull is calculated to find the boundary of the data set [78-80]. Then Delaunay triangulation is used to compute a bounding triangle for the interpolated area [81, 82]. Next, sparse bi-linear interpolation is applied to extract the value at every unknown voxel [29, 83, 84]. The complete DVF is then used to deform I_{moving}. The whole process is repeated iteratively using the Vercauteren method, until the stopping criterion S at iteration I is reached, where $S \geq \sum_{\#points} E_I^{P+1} / \sum_{\#points} E_I^P$ [85, 86].

2.2.4 Evaluations

The performance of Canny DIR is tested against several other registration methods, rigid registration, where only a global rigid 2D translational transformation is considered, Demons based method, distinct feature method, and the Canny DIR method. A modified open source version of the demons algorithm was used, with an intensity correction step, called intensity corrected Demons (IC Demons) [87]. The distinct feature extraction method was based on an open source code [68]. The Canny DIR method was developed in-house.

Common methods of establishing a ground truth include, using a known DVF applied to a reference image then applying Monte Carlo noise contamination, Gaussian noise contamination, and or an intensity transformation [22, 29, 36, 88-91]. Other popular methods include using an entirely digital phantom with a known DVF [92-94].

Monte Carlo noise contamination can be challenging in a 2D white light image, as there is no 3D surface information to base shading characteristics. Gaussian noise does not account for shading and lighting artifacts. Intensity transformations that simulate lighting and shading variations can be unrealistic. To overcome these challenges, two different ground truth models were created. A synthetic 3D mouse surface, and a 2D fluorescence accumulation model were used to evaluate the accuracy of the algorithm.

For the synthetic 3D mouse surface model, a microCT scan was taken with the Skyscan 1178 (Bruker, Kontich, Belgium), using an isotropic resolution of 200μm. A surface mesh was generated using marching cubes [95, 96]. A white light image, taken from the portable imager, was mapped on to the surface of the mouse. A line was drawn from each face on the surface, which passed through the white light image to a virtual

source. The pixel that the line passed through was used to shade the corresponding face. All the faces of the mouse surface are shaded using this method, until the mouse skin texture is fully mapped to the reconstructed mouse surface. The mouse surface was then deformed using a 15mm half sine wave in the LR direction, from the apex of the head to most posterior aspect of the feet. The mouse surface was then rotated from 0° to 40°. Figure 2.6 shows the synthetic mouse surface.

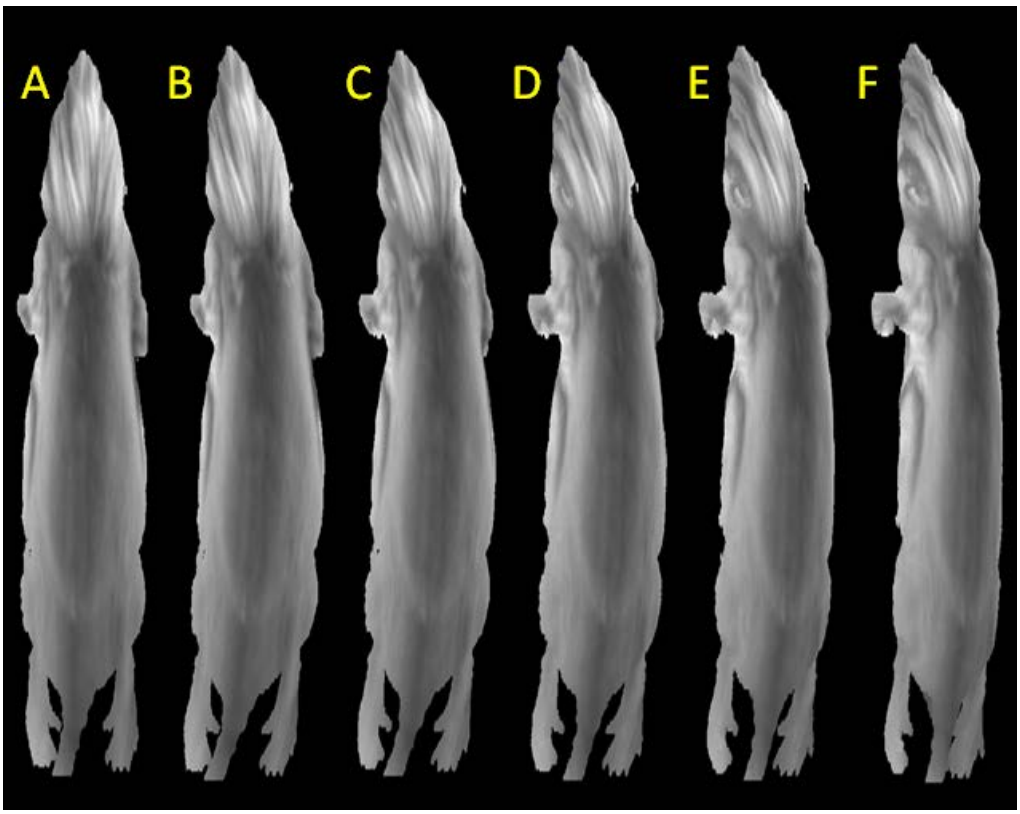

Figure 2.6. The synthetic mouse surface (A), with 15mm deformation at 0° rotation (B), 10° rotation (C), 20° rotation (D), 30° rotation (E), and 40° rotation (F).

The surface of the mouse was divided into multiple zones, to help understand the effects of rotation on different regions of the mouse surface. Figure 2.7 shows the various zones of the mouse surface.

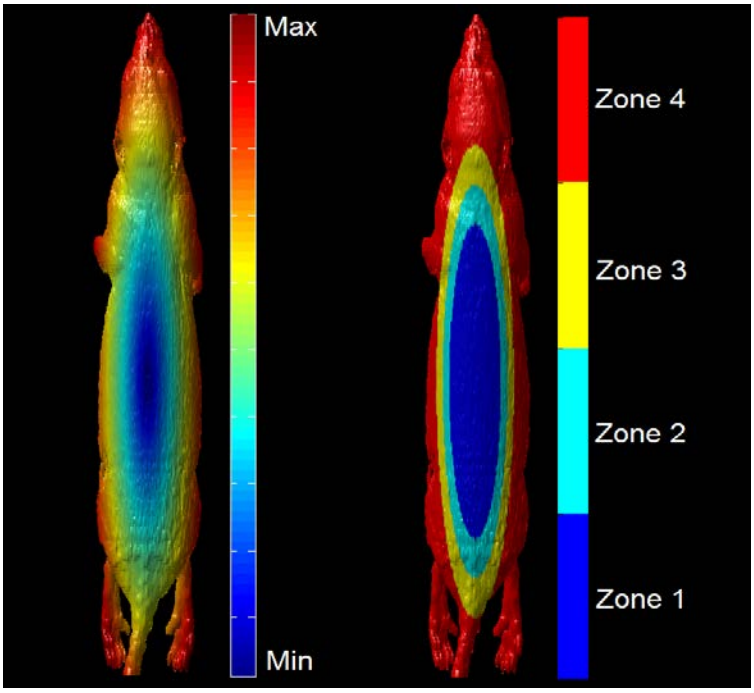

Figure 2.7. The mouse surface distance from centermost vertex on the posterior abdomen (left). The 4 zones of the mouse from centermost (zone 1) to outermost (zone 4).

White light based DIR will be used to deformably warp the white light image. The same set of DVFs will then be applied to the fluorescent image. The similarity of the original fluorescent image and the deformed fluorescent image are then evaluated using the gamma analysis technique [97]. If a direct spatial comparison between images is done, two corresponding pixels that are offset by a pixel width can lead to big

discrepancies using a direct spatial comparison [98-100]. For this reason it is favorable to use a technique that searches locally for a best match. Gamma analysis searches a specified area around each pixel until a best match is found. The smallest difference from each pixel is recorded for a given region of interest.

If *i*, and *j* represent the indexes of the image being analyzed, *k*, and *l* represent the search range specified, DTA represents the search range, and dose represents the percent error threshold, the gamma equation can be represented as, $G(i,j) = \arg\min\left\|Ga(k,l)\right\|$, where, $Ga(k,l) = \sqrt{\frac{r(i,j)^2}{DTA^2} + \frac{d(i,j)^2}{dose^2}}$, *r* represents the radial distance squared, and *d* represents the signal difference squared. The cutoff criterion is 95% of all pixels within a 3x3 pixel search range, are within 3% error [98].

To test the spatial congruence between the various registration algorithms, several intensity evaluation metrics were used, root mean square error of the Canny edge ($RMSE_{CE}$), normalized mutual information (NMI), and feature similarity index metric (FSIM). $RMSE_{CE}$ between the Canny edges C_1 and the Canny edges C_2 in corresponding images, are defined as, $\mathrm{RMSE}_{\mathrm{CE}} = \sqrt{\sum_i^N [C_2{}^i - C_1{}^i]^2 \Big/ \sum_i^N [C_2{}^i]^2}$ [70, 101]. NMI is a measurement of the mutual information between corresponding images [102-105]. FSIM evaluates gradient and phase information between corresponding images [106].

2.3 Results

2.3.1 Ground Truth Results

A checkerboard comparison between the static and deformed images for the rigid, SIFT, and Canny DIR methods is demonstrated in figure 2.8.

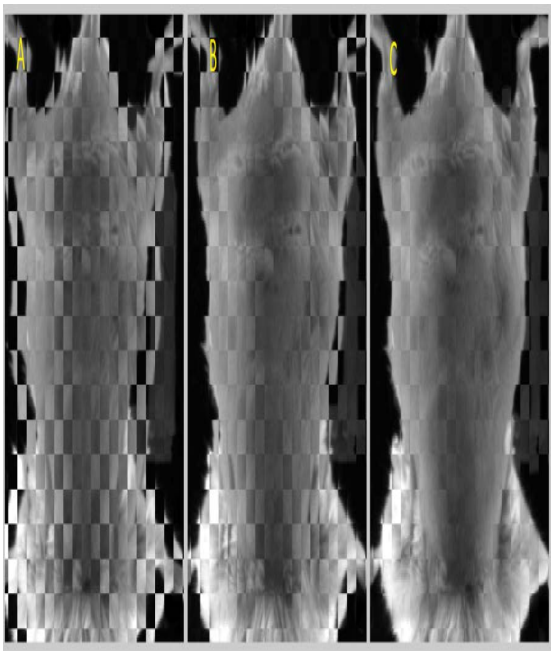

Figure 2.8. A checkerboard comparison between the static and the deformed images for rigid registration (A), SIFT (B), and Canny DIR (C).

Figure 2.9 shows an absolute difference comparison between the static and deformed images using rigid registration, SIFT, and Canny DIR methods, with its corresponding deformed fluorescent image sets.

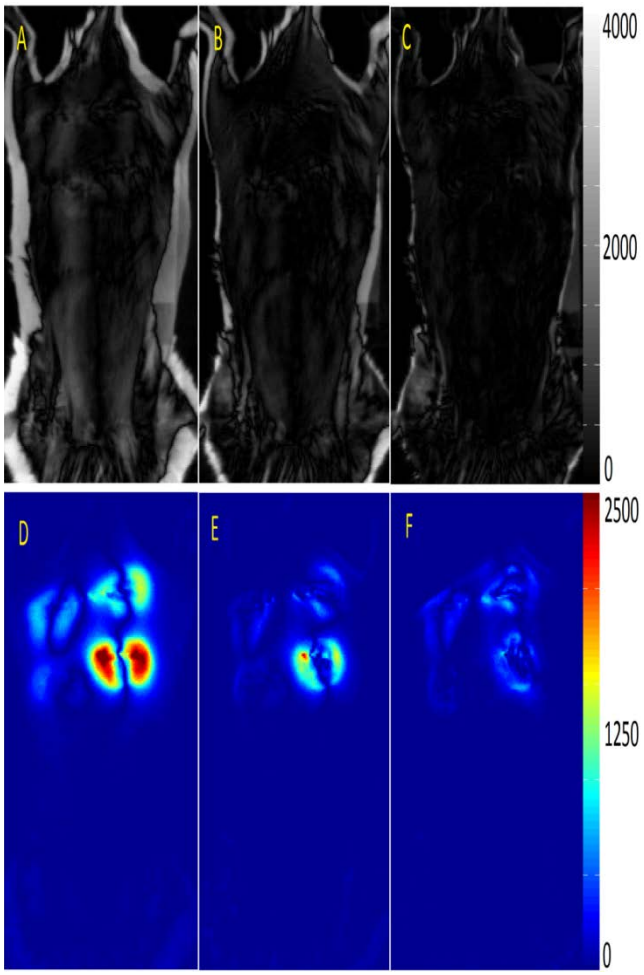

Figure 2.9 White light absolute value difference comparison between the static and deformed images for rigid registration (A), SIFT (B), and Canny DIR (C). Fluorescence absolute value difference comparison between the static and deformed images for rigid registration (D), SIFT (E), and Canny DIR (F).

To get a better understanding of the intensity congruence between image sets a gamma analysis was done between the various image sets. Figure 2.10 shows a gamma analysis between the static and deformed images using rigid registration, SIFT, and Canny DIR methods.

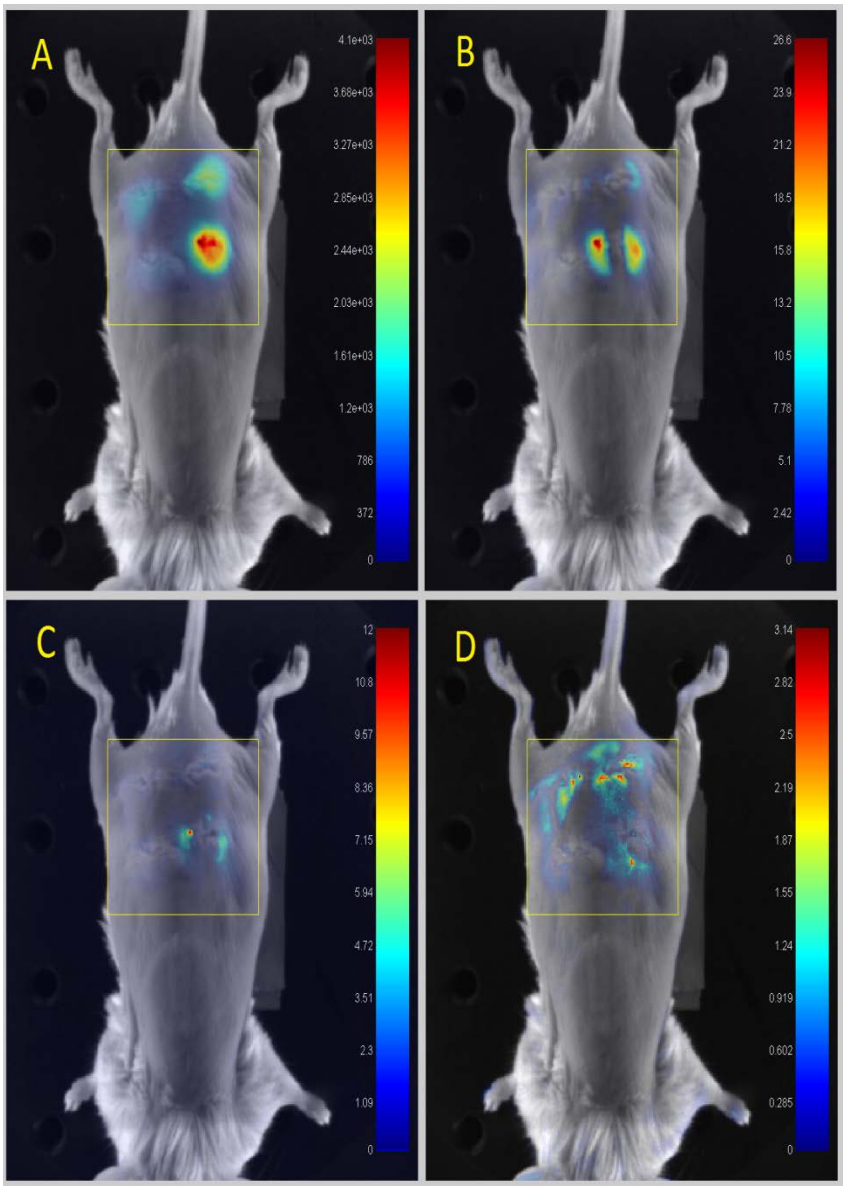

Figure 2.10. The white light image with the fluorescence superimposed on the static image (A). The static image with the superimposed fluorescence gamma comparison between the static and rigid registration (B), SIFT (C), and Canny DIR (D). The yellow box shows the area under consideration.

2.3.2 Evaluation Metrics Results

The synthetic ground truth scenarios were evaluated using the 90 percentile error margin for the IC Demons algorithm, SIFT and Canny DIR algorithms. Table 2.2 shows the DVF accuracy for all synthetic scenarios using various DIR methods.

Table 2.2. The DVF 90 percentile error for IC Demons, SIFT, and Canny DIR methods for all synthetic scenarios.

		0°	10°	20°	30°	40°
zone 1	IC Demons 90% error (μm)	240.3	310.2	398.5	530.6	618.7
	SIFT 90% error (μm)	291.4	304.4	376.0	435.2	503.4
	Canny DIR 90% error (μm)	258.2	276.4	289.4	310.1	395.5
zone 2	IC Demons 90% error (μm)	248.1	300.9	371.0	529.1	781.8
	SIFT 90% error (μm)	279.7	316.5	387.9	410.6	566.2
	Canny DIR 90% error (μm)	251.2	281.0	297.1	357.3	442.1
zone 3	IC Demons 90% error (μm)	234.8	283.0	408.8	581.0	738.6
	SIFT 90% error (μm)	269.6	297.8	358.6	481.9	703.1
	Canny DIR 90% error (μm)	259.3	268.1	284.7	392.8	569.0
zone 4	IC Demons 90% error (μm)	221.8	298.1	387.9	577.0	807.7
	SIFT 90% error (μm)	304.5	312.6	353.1	433.3	758.8
	Canny DIR 90% error (μm)	232.2	261.0	297.3	401.4	631.9

Table 2.3 shows the registration results from 7 mice evaluated with NMI, RMSE, and FSIM evaluation metrics.

Table 2.3. The evaluation matrix results from 7 mice with their corresponding mean values are shown for NMI, RMSE, and FSIM. The values for the various registration methods are shown, including rigid, intensity corrected Demons, SIFT, and canny edge registration.

		1	2	3	4	5	6	7	mean
NMI	Rigid	0.56	0.51	0.59	0.62	0.61	0.63	0.49	0.57
	IC Demons	0.61	0.55	0.67	0.66	0.65	0.70	0.67	0.64
	SIFT	0.78	0.74	0.70	0.87	0.71	0.80	0.72	0.76
	Canny	0.85	0.83	0.84	0.89	0.81	0.89	0.75	0.84
RMSE	Rigid	0.42	0.34	0.38	0.41	0.40	0.43	0.42	0.40
	IC Demons	0.39	0.35	0.45	0.43	0.43	0.46	0.44	0.42
	SIFT	0.30	0.30	0.29	0.36	0.29	0.32	0.30	0.31
	Canny	0.20	0.20	0.16	0.21	0.19	0.21	0.18	0.19
FSIM	Rigid	0.63	0.53	0.56	0.59	0.59	0.65	0.52	0.58
	IC Demons	0.60	0.54	0.69	0.71	0.66	0.68	0.62	0.64
	SIFT	0.89	0.83	0.82	0.83	0.82	0.89	0.78	0.84
	Canny	0.91	0.91	0.99	0.96	0.87	0.98	0.83	0.92

To evaluate the intensity congruence of the various registration algorithms the maximum gamma error was used as well as the overall gamma passing rate. A gamma passing rate of 3% error with a (150 x 150) μm^2 search range was used. For maximum gamma a (150 x 150) μm^2 search range was also used. Table 2.4 shows the gamma evaluation results.

Table 2.4. The gamma analysis results from 7 mice with their corresponding mean values are shown for the maximum gamma error and the gamma passing rate. The values for the various registration methods are shown, including rigid, intensity corrected Demons, SIFT, and canny edge registration.

		1	2	3	4	5	6	7	mean
Max Gamma	Rigid	29.47	23.87	26.82	28.67	28.32	29.86	29.84	28.12
	Parametric	31.78	24.82	31.48	30.51	21.80	32.21	31.45	29.15
	SIFT	12.38	11.95	8.40	14.38	11.44	12.94	7.90	11.34
	Canny	5.96	9.50	4.87	6.23	5.66	6.35	5.37	6.28
Failing %	Rigid	21.07	16.84	19.22	20.24	19.90	21.51	21.59	20.05
	Parametric	25.65	17.07	22.60	21.19	21.01	22.88	21.96	21.77
	SIFT	7.34	10.10	4.30	8.34	6.85	7.42	3.90	6.89
	Canny	2.89	4.90	2.45	3.23	2.84	3.21	2.68	3.17

2.4 Discussion and Conclusion

The ground truth accuracy for the synthetic scenarios for IC Demons, SIFT, and Canny DIR were all evaluated at the 90% error margin. For the 0° scenario, all the algorithms performed well for all zones and were within 305μm at the 90% error margin. For the 10° scenario all the algorithms performed fairly well overall and the Canny DIR slightly outperformed all other algorithms. For the 20° scenario, the IC demons and SIFT algorithms performed poorly for some zones, while the Canny DIR algorithm performed well for all zones and was within 300μm for all zones. At 30° rotation, most of the methods for all the zones did not perform well, except for zones 1 and 2 of the Canny DIR method. Zone 1 is within 310.1μm at the 90% error margin. For the 40° scenario, all algorithms for all zones perform poorly but the Canny Edge method performs far better than all other algorithms, especially for zone 1, which stays within 395.1μm at the 90% error margin. The synthetic ground truth test demonstrates that the Canny DIR method is accurate in the presence of rotations (≤20°). However, under larger rotations, between 20° and 30°, the surface tracking should be limited to zone 1. Rotations larger than 30° should be avoided.

For the evaluation matrices, the IC Demons performed near as well as rigid registration for the RMSE evaluation method and only slightly better than the rigid registration method for the NMI and FSIM. Although the intensity distribution is transformed towards the target image, the resulting DVF is not a good representation of the physical morphological deformation [107]. Since the objective function of the demons method is minimizing intensity difference distribution between the deformed and

static image, intensity evaluation metrics can give artificially good results [108]. The RMSE method, produces poor results in this case because it is a representation of how well the edges between the images are aligned [109].

The SIFT performance was generally much better than IC Demons. This method will perform particularly well when evaluated with NMI or FSIM because the distinct features are chosen on regions of the image that have rich intensity and gradient features. So when these regions are selected for intensity matching they will have a somewhat better performance. This method performs only slightly better than IC Demons method when evaluated using RMSE, because the edges between the deformed and static image do not match up well. This is in part because the distinct features are not dense along the image edges. If the distinct feature extraction method is less discriminatory, more features will be used but they will be less stable and will produce more deformation errors [64]. There will always be a tradeoff between the amount of distinct features being used and the quality of the overall quality of the features [68]. For this study the removal criteria was calibrated to achieve the best possible NMI performance.

There is an effect on the canny edge sensitivity ε and the SIFT removal tolerance ω. The effects of changing the canny edge and SIFT constants can be seen in figure 2.11

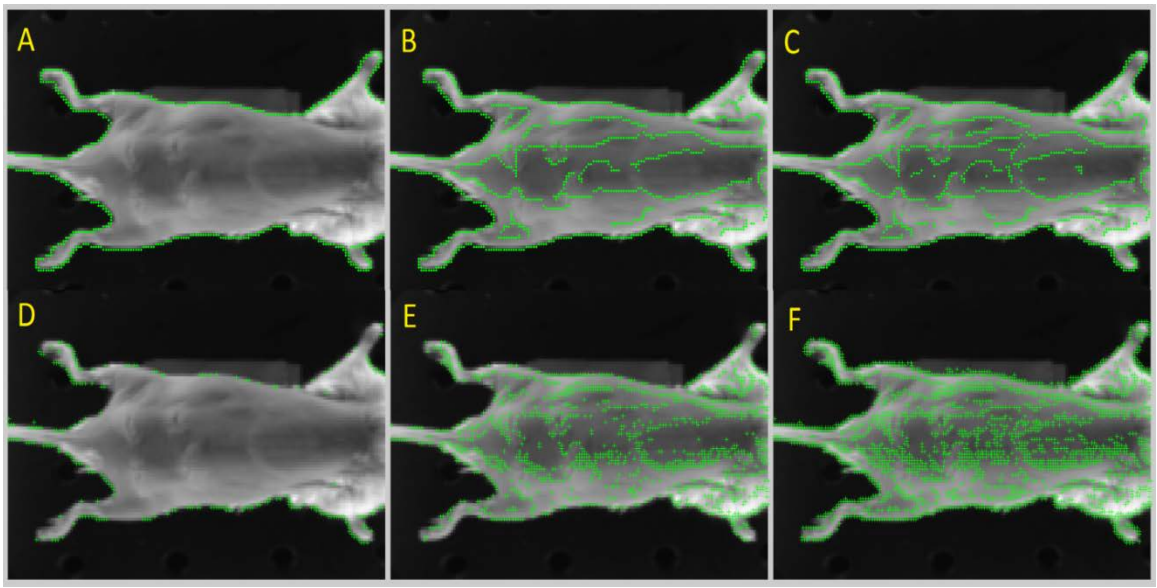

Figure 2.11. Canny edges with an ε_{lower} of 0.1 and an ε_{upper} of 0.9 (A), an ε_{lower} of 0.01 and an ε_{upper} of 0.1 (B), and an ε_{lower} of 0.001 and an ε_{upper} of 0.01 (C). SIFT points with an ω of 0.1 (D), an ω 0.01 (E), and an ω 0.001 (F).

Although the optimal values for the upper threshold ε_{upper} and lower threshold ε_{lower} will vary somewhat depending on the imaging environment, a normalized ε_{upper} value of 0.1 and an ε_{lower} value of 0.01, tend to produce the best tradeoff between edge density and edge quality. Similarly, using an ω of 0.01 offered a good tradeoff between distinct feature density and quality.

The canny DIR method performed better than all other methods for every evaluation metric used. It performed only slightly better than the SIFT method for the NMI evaluation metric. This is in part due to the distinct feature selection criteria bias towards NMI performance, which stems from the removal criteria calibration [105]. It had the largest performance increase over all other methods for the RMSE evaluation

metric. Since the canny DIR method uses stable edges, it is expected that an edge-based evaluation matrix would give good results.

For the gamma analysis evaluation methods, it can be seen that the IC Demons method performed the worst, which suggests that the DVFs are not accurate. This method sacrifices spatial congruence for intensity congruence. As a result, the quality of the DVFs can suffer, in the presence of lighting and shading variations.

The SIFT method performed far better than the rigid registration method for both the maximum gamma and the gamma passing rate tests. This method had a mean maximum gamma of roughly twice as small as the rigid registration method and about triple the gamma passing rate. This is a good indication that this method had realistic DVFs.

The canny DIR method outperformed the district feature method for both the maximum gamma and the gamma passing rate tests. This method had a mean maximum gamma of roughly twice as small as the SIFT method and about 2x better gamma passing rate. This is a strong indication that the canny DIR method has the most accurate DVFs.

It is important to note that, all the canny DIR mice passed the gamma analysis test and that only two mice passed the gamma analysis test for the SIFT method. Also, none of the mice passed the gamma test for the IC Demons or rigid registration methods.

Since, 2D white light images are based on 3D surface projections of mice, there are some limitations to using the Canny DIR method. Canny DIR, will not account for large mouse rotations, since the region of the skin surface being image can change between time points. Care must be taken during setup and positioning to help minimize

rotation. The mice should be oriented such that the fluorescent implants are not too far from the center of the mouse surface, with respect to the imager. Future work will be directed at comprehensively analyzing the setup, and implantation imaging limitation of this method.

In conclusion, this paper demonstrates the canny DIR spatial accuracy improvement over other existing methods using intensity and fluorescence based evaluation matrices. Canny DIR is resistant to illumination changes due to anatomical deformation and can accurately accumulate fluorescence signals.

2.5 Acknowledgements

This work was supported by grants from Progenitec Inc. and NIH AR064650-01 and EB014404-01.

CHAPTER 3

IN VIVO TEMPORAL TRACKING AND MULTIPLE FLUORESCENT SIGNAL EXTRACTION

3.1 Introduction

3.1.1 Cell Tracking

It is well known that early diagnosis of cancer has a direct correlation to patient survival rate [110]. As malignant cells propagate within a patient, they can spread to adjacent tissues or in the form of metastasis via the lymphatic or circulatory system [111]. It is widely accepted that the ineffectiveness of conventional cancer therapy is in part caused by active cancer metastasis [112]. Furthermore, inflammatory responses have been associated with cancer metastasis. In a recent study, mice implanted with EPO releasing scaffolds on average had a 30% longer lifespan compared to groups with no EPO [113]. Other types of traps have shown potential in reducing tumor burden, such as Vascular endothelial growth factor combined with paclitaxel, and tartrate-resistant acid phosphatase [114-117]. As the results of this observation, implantable, sustained release devices that release chemokines have been developed to study the influence of chemokine on metastatic cancer migration [118]. Unfortunately, identification and tracking of the chemokine release throughout the course of the experiments can place a heavy burden on the clinical or experimental resources. Furthermore, intra- and inter-user implant delineation can introduce experimental errors and potentially reduce the reliability of the tracking results. To overcome this challenge a computer assisted

temporal tracking algorithm, that relies on white light based DIR, will be developed and implemented. The computer assisted implantation temporal tracking algorithm will incorporate the Canny DIR algorithm and use the same imaging design and geometry as previously mentioned in chapter 2.

3.1.2 Multiple Sites

During small animal optical imaging implantation space on the surface of the mouse is limited. For direct comparison, it can be advantageous to image multiple implantation peaks in one snapshot [119]. It is often desirable to take a functional image immediately after implantation for calibration and tracking purposes. During this time, the peaks of each implantation site will tend to be at their maximum intensities. This can make peak detection and signal intensity quantification difficult, as the various peaks may blead into each other. A weaker signal can be completely missed if it is overpowered by a neighboring strong signal, or two strong signals can cross contaminate each other [120]. Therefore, local maxima must be extracted in the presence of background contamination.

To analyze a signal and extract meaningful information from it, two main approaches are often used. One approach is to decompose it into separate course resolution components. Individual wavelets are used to parametrically model the observed signal. This method is referred to as wavelet analysis [121]. Another popular approach is to decompose a course resolution signal into latent variables, and then use the fine resolution signal to statistically derive them [122]. Recreating the latent course

resolution variables from fine resolution observations is a much beefier statistical inference, and is referred to as wavelet synthesis.

Image processing using wavelet synthesis can be thought of as machine learning [123]. This method is very advantageous when considering many latent variables. Algorithms such as artificial neural networks, semi-supervised learning, and deep learning have wide application in image recognition applications, such as edge extraction, facial recognition, facial expression, and radar unjamming [124-126]. Machine learning based signal extraction based approaches have been used to detect and extract signals [127, 128]. Machine learning based signal extraction approaches require a very large training data set and are often very computationally expensive. Machine learning-based signal extraction is not a viable option for this problem as the experimenters do not always have sufficient training data. Machine learning algorithms may require large sets of known single signals to sufficiently condition the extraction algorithm [129, 130].

Multiple-site wavelet analysis based models have been developed for 1 dimensional problems [131, 132]. Wavelet analysis based models using parametric decomposition do not require large training data sets, and are computationally inexpensive. A 2D wavelet analysis approach is used, since this study does not depend on large training sets and is designed to be speedy so that it does not interfere with the *in vivo* workflow.

3.1.3 Peak Tracking

Although DIR based on structural images is an essential part of functional signal tracking, there are still scenarios in which DIR alone will not suffice to temporally track a functional signal. In some instances, once a fluorescent marker is implanted, the signal can begin to weaken, diffuse, change form, or drift away from the initial implantation site. When this occurs, longitudinal signal quantification can be challenging. It can be cumbersome to manually sort through large longitudinal sets of images. Also intra-user manual signal contouring can be prone to user error and or user expectation bias [133, 134].

Automated peak detection algorithms have shown potential in reducing inter- and intra-user peak contouring variability [135-137]. However, these algorithms all rely on an initial training set of data for calibration. Additionally, when the morphology of the signals changes in an unpredictable way, pre-conditioned peak finding algorithms tend to break down. To overcome this challenge it is desirable to have a peak finding algorithm that is user-conditioned, guided by structural images, reside in the original local vicinity, and only considers peaks that are morphologically similar to the original peak.

This study will focus on the development and evaluation of a novel longitudinal fluorescent signal tracking algorithm. In order to extract multiple sites per image, a wavelet analysis based model will be used. To demonstrate the utility of these tracking algorithms, this technique will be implemented on several common fluorescent tracking applications. Since the peak finding algorithm must be user-conditioned an end-user software application was built called PortableView.

3.2 Methods and Materials

3.2.1 Multiple Site Background Removal

To extract the background from multiple sites, local maxima must first be identified. To do this, a variant of the growing method will be used to find and remove the most dominant implantation signals. Then the growing routine, previously described, can be reapplied to find and remove the next most dominant implantation signal. Once all the locations of the implantations have been identified connection lines are extracted, which connect all implantation sites together. The recorded values along the lines will be used to solve to the background of each implantation site simultaneously, as the problem will be cast into an optimization routine. The computed emission profiles from the optimization routine will be used to generate the implantation site boundaries and estimate the implantation site tails. The tails will be used to obtain a more accurate boundary of each implantation site.

Figure 3.1 shows the peak extraction and separation process. The surface contours of the peaks are shown in false color, with the height associated with the signal strength.

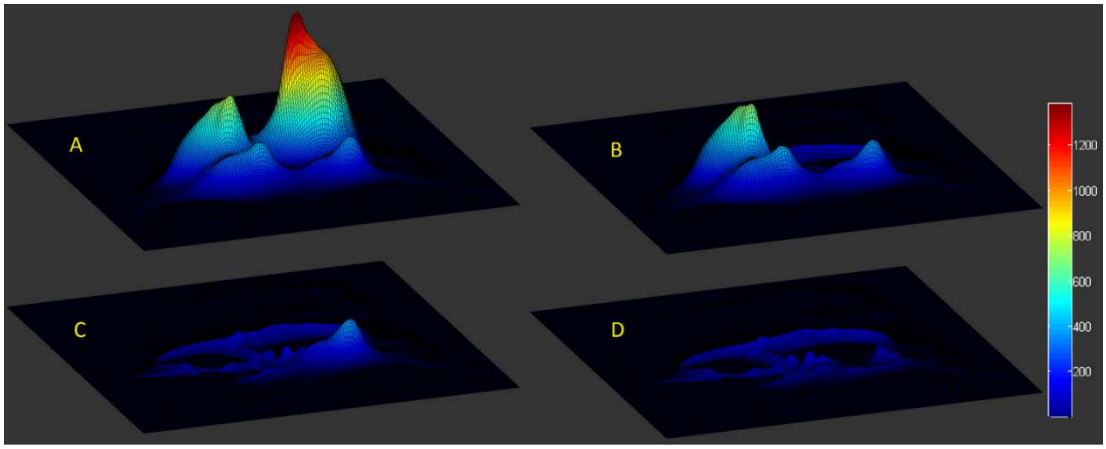

Figure 3.1. The original signals are shown for all four peaks (A). The most dominant peak has been removed with its corresponding tails (B). The three most dominant peaks have been removed with all of their corresponding tails (C). All of the peaks have been removed with all of the associated tails. (D).

Once the boundaries of the implantation sites are initially estimated the background of the fluorescent image is calculated by taking the mean of all regions on the mouse that are not within an expansion around each implantation site. Once all the tails of the multiple implantation sites are estimated, each peak is isolated by subtracting all the neighboring peak tails. By subtracting all the tails, all the peaks can be analyzed without the contamination from their neighbors. The statistical information is generated from the isolated peaks, such as the standard deviation, mean, maximum, and minimum values within each peak. Figure 3.2 demonstrates the delineation of the boundary of each isolated peak. The surface contours of the peaks are shown in false color, with the height and transparency associated with the strength of each signal.

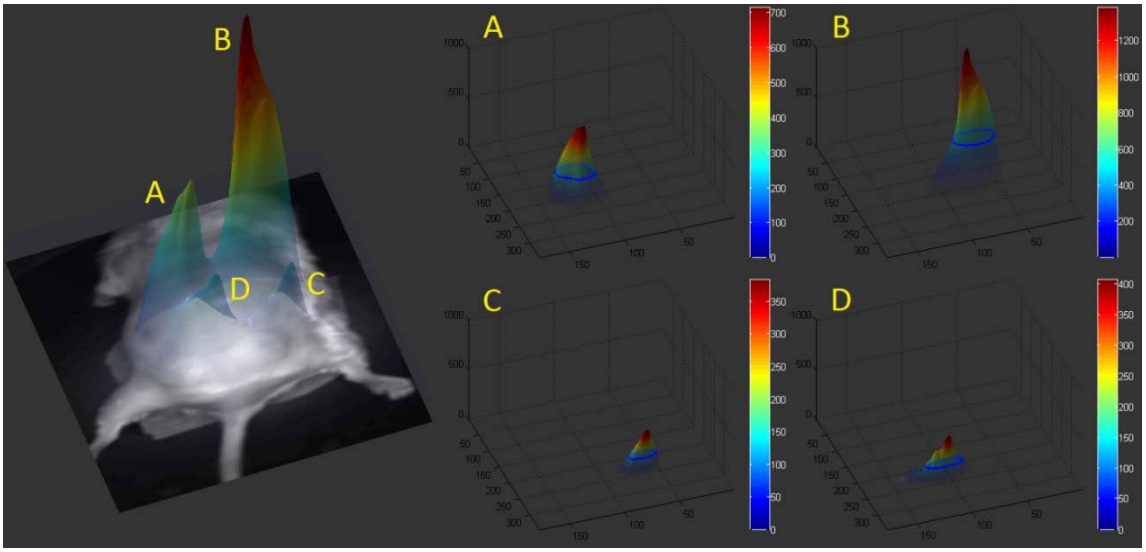

Figure 3.2. All four peaks superimposed on the white light image of the mouse (Left). For A-D the 1/3 maximum isoline is represented with a blue line. The second most dominant isolated peak (A). The most dominant isolated peak (B). The third most dominant isolated peak (C). The least dominant isolated peak (D).

3.2.2 Peak Tracking

First, the canny DIR algorithm will deform all white light images at all later time points $W_{moving}^{1:n}$ to the initial white light image W_{static}^{0}. This will produce a set of $DVF^{1:n}$, which will be used to deform the set of fluorescent images at all later time points $F_{moving}^{1:n}$ into a deformed fluorescent image set $F_{deformed}^{1:n}$. Each set of fluorescent images will be in the same spatial reference frame as the initial fluorescent image F_{static}^{0}. The peak assessment and tracking algorithms for each time point will be based on the corresponding $F_{deformed}^{n}$ image. Multi-peak signal extraction will then be implemented. Finally, the entire process will be wrapped inside an end user application PortableView.

A user will specify the number (m) of peak regions on the F_{static}^{0} fluorescent image, with an associated relative intensity threshold (τ^m). The τ^m will be used to outline a closed region encompassing any pixel values above τ^m for each peak region. Each region will then be processed in binary form. Each binary form will then be flood filled to close any opening within the each peak boundary. Each binary image will then be analyzed for connected bodies. All disconnected bodies above a below a certain size will be discarded. This will help reduce the effects of dispersion, and the background signal. The final processed peaks within each binary boundary will then be used to extract the separate morphology and intensity characteristics. The initial set of m peaks inside the processed boundaries $P_{static}^{m,0}$ will then be used to find corresponding peaks at later time points $P_{moving}^{m,n}$.

The $P_{moving}^{m,n}$ is registered to a corresponding region on the $F_{deformed}^{1:n}$ using gradient, intensity, and morphology information. To compare morphologies, bounding ellipsoid eccentricities and texture information are used. The texture and eccentricity similarities are scored and grouped into a penalty, which is referred to as the morphology penalty (ρ).

$P_{moving}^{m,n}$ will then be shifted by (x,y) and rotated by (θ) incrementally in a steepest decent manner, until Q is minimized for each peak, where

$$Q(x,y,\theta)^{m,n} = \left\| (\nabla P_{static}^{m,0} - \nabla P_{moving}^{m,n})^2 (P_{static}^{m,0} - P_{moving}^{m,n})^2 + \rho \right\|$$

$$x,y,\theta = \arg\min Q(x,y,\theta)^{m,n}$$

With the condition that $r \geq \sqrt{x^2 + y^2}$ is satisfied.

Once a registration offset is determined for each $P_{moving}^{m,n}$, a signal extraction routine is implemented to delineate the new signal peak. If the minimized *Q* score is too high, or $r \geq \sqrt{x^2 + y^2}$ is not satisfied, the peak is determined to not exist, and is discarded.

The signal extraction routine uses the offsets *x* and *y* to start an initial peak growing routine. A peak growing routine is started based on the registration offsets. The connecting voxels grown around a central voxel at (*x*,*y*) will be used to determine if the signal originates from diseased tissues, as described by other groups [136]. A new $P_{growing}^{0}$ is defined at the center of *x* and *y*. Starting at the maximum image value *Vxy*, an expansion is created in four neighboring voxels *Vxy-1*, *Vxy+1*, *Vx+1y*, and *Vx-1y*. If any of those neighboring voxels are above the threshold τ^m then they will be included in the growing area $P_{growing}^{i}$. $P_{growing}^{i}$ is expanded incrementally to include any pixels inside the threshold τ^m, until $P_{growing}^{i} = P_{growing}^{i+1}$. Once this condition is reached, $P_{growing}^{i}$ is saved as $P_{deformed}^{m,n}$ and the process is completed for all peaks at all time points.

In Summary, to deform the set of contours, the DVF resulting from the DIR algorithm are applied directly to a binary scalarized form of the user specified peaks. The Deformed scalars are then thresholded to a binary format where 0 represents all pixels outside the peak and 1 represents inside the peak. The peak tracking algorithm is then applied to each peak individually. Finally all peaks are polygonised for visualization. Figure 3.3 represents the workflow of the peak tracking method.

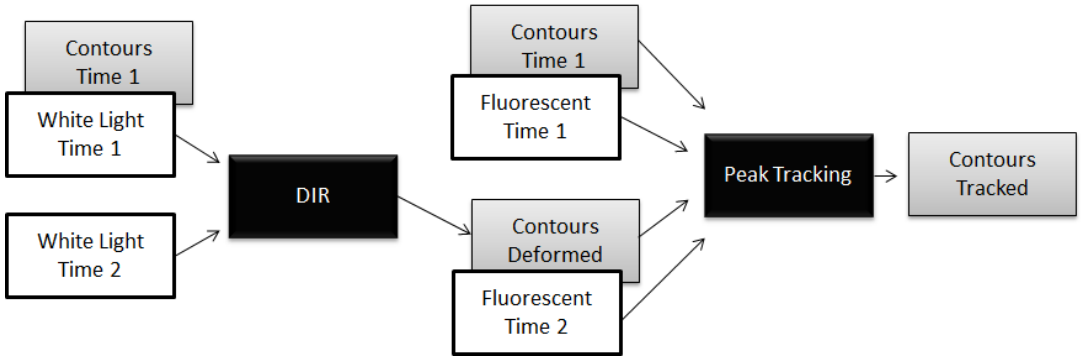

Figure 3.3. The workflow for the peak tracking method using white light-based DIR. Contours 1 represents the user specified peaks of the first time point. Contours deformed represent the deformed contours that result from the DIR algorithm. Contours tracked represent the tracked contours that result from the peak tracking algorithm.

Figure 3.4 shows two examples of the Canny DIR combined with the signal extraction method using two in vivo mice.

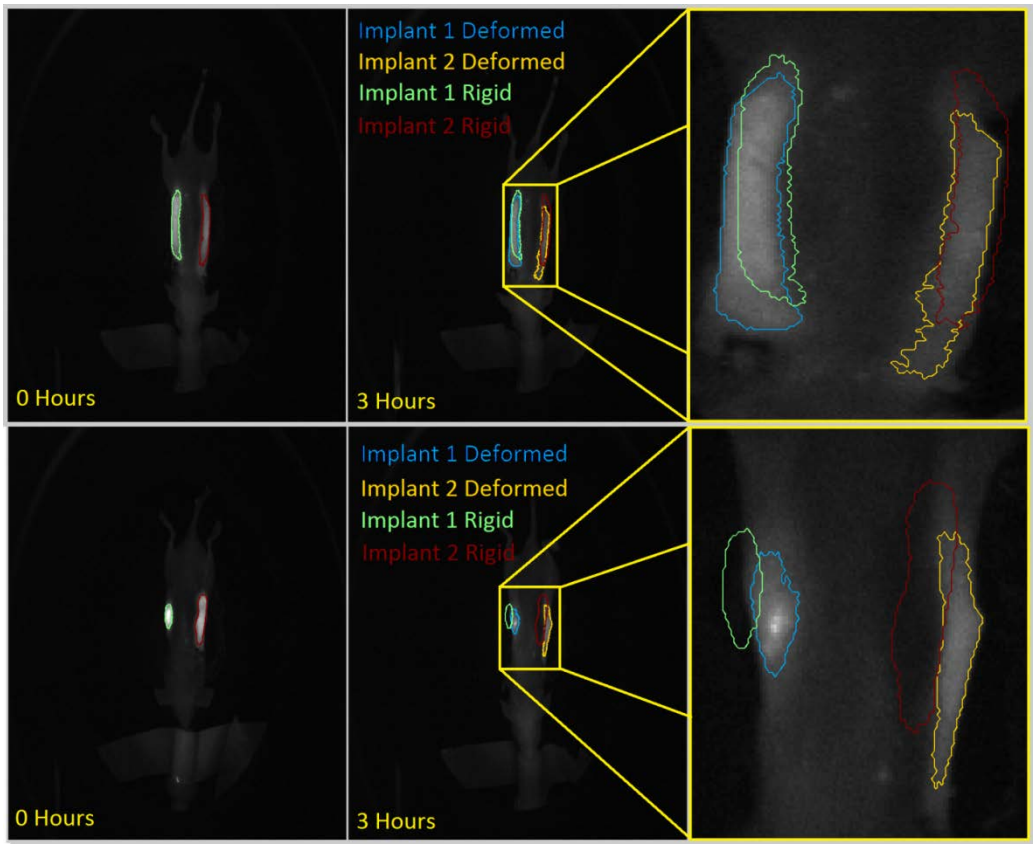

Figure 3.4. Top Left: Mouse implanted with tube containing cotton (light green) and no cotton (red) at 0 Hours. Top Middle: Mouse after 3 hours showing the deformed implantation containing cotton (light blue) and the deformed implantation without cotton, and the rigid registered cotton tube (light green) with the rigid registered non cotton tube (red). Top Right: Zoomed Mouse after 3 hours with corresponding contours. Bottom Left: Mouse injected with liquid (light green) and implanted with a tube (red) at 0 Hours. Bottom Middle: Mouse after 3 hours showing the deformed liquid injection (light blue) and the deformed implantation, and the rigid registered liquid injection (light green) with the rigid registered tube implantation (red). Bottom Right: Zoomed Mouse after 3 hours with corresponding contours.

To demonstrate the automated contour tracking algorithm, two different imaging test scenarios were conducted. Mouse 1 has two implantations, one using a polyurethane tube and the other without a tube. The polyurethane tube is implanted inside the mouse prior to EPO injection. It is compared with saline mixed with EPO. EPO is tagged with

CY5 for fluorescence tracing. The relative intensities of the two injection sites will be compared for multiple time points to assess the release time of the implant. Mouse 2 has two tube implantation, one of the tubes contains cotton, and the other tube does not contain cotton. EPO tagged with CY5 was injected into each tube, then the intensities were taken at multiple time points to assess how much cotton helps the implanted tube retain EPO.

Since the shape and intensity distribution change between time points for each contour, the intensity distribution of the individual contours will be used as opposed to directly comparing intensity information in the context of their relative spatial distribution. To account for the changing spatial distribution of the individual peaks, confined NMI is used instead [29]. The confined NMI of the deformed contours on the later fluorescent images is compared with the original contours on the first fluorescent images taken for each study.

3.3 Results

3.3.1 Multiple Site Background Removal

The peaks are estimated at the isovalue of 60% from their individual maximums once the background has been subtracted. The isolated peak statistics are then compared with the initial unprocessed raw peak values for comparison. The background is also removed from the initial peak values, and the isovalues are also reported at 60% from their individual maximums. Figure 3.5 shows the boundaries of each isolated peak with

the associated mean intensity values between the raw values and the peak extrapolation values.

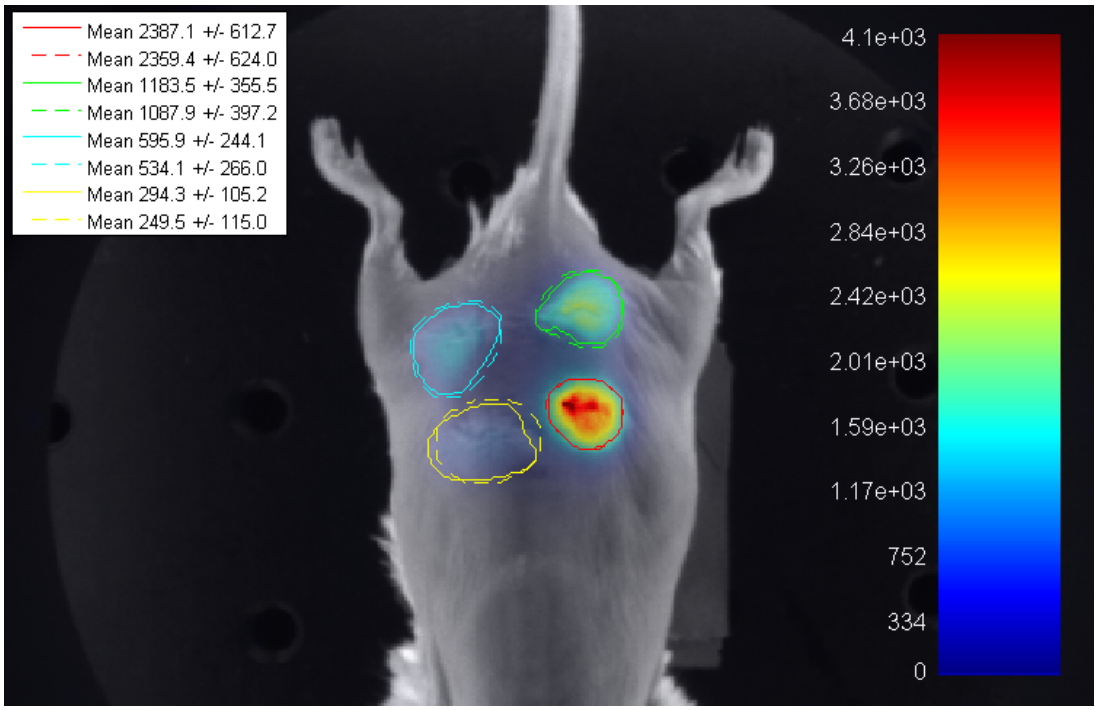

Figure 3.5. The boundaries of each isolated peak is shown superimposed on the white light image. The red peak is the most dominant, the green peak is the second most dominant, the light blue peak is the third most dominant, and the yellow peak represents the least dominant peak. The mean values of all isolated peaks are shown in the legend on the top left corner. For each peak the solid line represents the extrapolation corrected peaks and the dashed line represents the raw peaks.

To evaluate the accuracy of the resulting extracted signals, known concentrations of fluorescent tracer CY5 will be implanted using an *in vivo* mouse model. CY5 is a near infrared fluorescent dye with an emission wavelength of 630-700nm [76]. All imaging data was collected using the previously described Progenitec portable imaging system. This device was built based on funding provided by Progenitec. Several fluorescent tracers were implanted into the mice, and imaged immediately.

The extracted fluorescent signals will be compared with known concentrations of CY5. 4 different concentration ratios will be used on each mouse. An initial concentration of $0.15\frac{\text{mg}}{ml} \pm 0.01\frac{\text{mg}}{ml}$ was used for the most concentrated site. The lower concentrations were created by diluting the initial concentration by 2, 4, and 8 times the initial concentration with an error of $0.01ml$. The error ($error_1^C$) for each concentration value ($Value_1^C$) can be calculated using the previous concentration value ($Value_0^C$) and error ($error_0^C$), as well as the volume dilution ($Value_1^V$) and error ($error_1^V$), as seen in the following equation, $error_1^C = Value_1^C \sqrt{\left(\frac{error_0^C}{Value_0^C}\right)^2 + \left(\frac{error_1^V}{Value_1^V}\right)^2}$. The 2x dilution concentration is $0.075\frac{\text{mg}}{ml} \pm 0.005\frac{\text{mg}}{ml}$, the 4x dilution concentration is $0.0375\frac{\text{mg}}{ml} \pm 0.025\frac{\text{mg}}{ml}$, the 8x dilution concentration is $0.01875\frac{\text{mg}}{ml} \pm 0.00125\frac{\text{mg}}{ml}$. 30ul injections per site were used, with an led power current of 40 mA, using a 6 second exposure time at 2 x 2 pixel binning. 6 different mice were used in this study. Relative concentration ratios will be used as a metric to evaluate the overall accuracy the extracted concentration values.

The accuracy of the background corrected values are compared with the initial uncorrected values. The mean relative concentrations of each peak are used instead of the absolute concentration values. This helps negate the influence of the day to day differences between user needle insertion depth during injection. Also, mice can have varying skin thickness, and tissue inconsistencies which can affect the absolute

fluorescent values. Table 3.1 shows the various mean concentration values for all the mice, for the corrected and uncorrected algorithms.

Table 3.1. The absolute mean concertation values are shown for all 6 mice for both algorithms. The initial corrected % values represent the average % of each mouse's concentration level compared with the 1x concentration value for the corrected algorithm. The initial uncorrected % values represent the average % of each mouse's concentration level compared with the 1x concentration value for the uncorrected algorithm.

Algorithm	Concentration	1	2	3	4	5	6	% Initial Corrected	% Initial Uncorrected
Corrected	1x	2370.8	2177.0	2247.3	2538.1	2718.7	2220.8	100.00	
	0.5x	1065.2	1070.0	777.7	1390.8	1506.8	1460.4	52.78	
	0.25x	581.4	500.3	551.7	355.8	796.3	740.6	23.78	
	0.125x	276.9	234.6	192.0	256.1	404.0	394.0	11.08	
Uncorrected	1x	2288.0	2150.8	2174.3	2444.1	2730.4	2143.3	100.00	97.55
	0.5x	874.5	820.0	1002.8	947.6	1207.7	921.4	41.41	40.40
	0.25x	638.2	601.9	546.0	584.1	655.3	448.1	23.97	23.36
	0.125x	160.6	240.4	179.0	202.5	153.3	180.9	8.13	7.92

3.3.2 Peak Tracking

Table 3.2 shows NMI confined to the contours on the later fluorescent time points. The confined NMI is highest for the tracked algorithm compared to the deformed or rigid registration, which indicates that the relative intensity distribution between the tracked contours on the later fluorescent time points match best with the relative intensity distribution of the original contours on the first set of fluorescent images.

Table 3.2. NMI is shown for individual contours. NMI of the contours for M1 with the tube and without the tube for all time points (top), NMI of the contours for M2 with the tube and with the tube and cotton, for all three registration algorithms, rigid, deformed, and tracked.

	M1 Tube			M1 No Tube		
Time (Hours)	Rigid	Deformed	Tracked	Rigid	Deformed	Tracked
3	0.38	0.59	0.63	0.31	0.41	0.67
6	0.29	0.53	0.60	0.23	0.29	0.51
20	0.12	0.41	0.54	0.16	0.23	0.43
28	0.17	0.37	0.49	0.11	0.19	0.19
48	0.15	0.28	0.32	0.16	0.18	0.18
	M2 Tube			M1 Tube + Cotton		
Time (Hours)	Rigid	Deformed	Tracked	Rigid	Deformed	Tracked
6	0.31	0.45	0.62	0.37	0.51	0.68
20	0.19	0.43	0.52	0.27	0.50	0.61
28	0.14	0.42	0.44	0.11	0.43	0.49
48	0.18	0.31	0.39	0.16	0.35	0.40

The tracking results for two different experiments can be seen in table 3.3. The comparison between the tube and no tube scenarios can be seen under mouse 1 (M1). The comparison between the tube with cotton and the tube without cotton scenarios can be seen under mouse 2 (M2).

Table 3.3. The percent release of the M1 scenario can been seen for 0, 3, 6, 20, 28, and 48 hours for the tube and no tube scenarios with the associated t-test p-value. The percent release of the M2 scenario can been seen for 0, 6, 20, 28, and 48 hours for the tube with cotton and tube without cotton scenarios with the associated t-test p-value.

	time (Hours)	Tube	No Tube		time (Hours)	Tube	Tube + Cotton
M1	0	0	0	M2	0	0	0
	3	45.1	69.3		6	48.2	23.1
	6	65.7	92.3		20	81.4	68.1
	20	74.1	98.9		28	92.7	76.7
	28	82.2	98.1		48	98.1	85.3
	48	96.9	97.1				
		p-value	0.010005			p-value	0.004892

Figure 3.6 shows a graphical representation of the relative percent release for scenario M1.

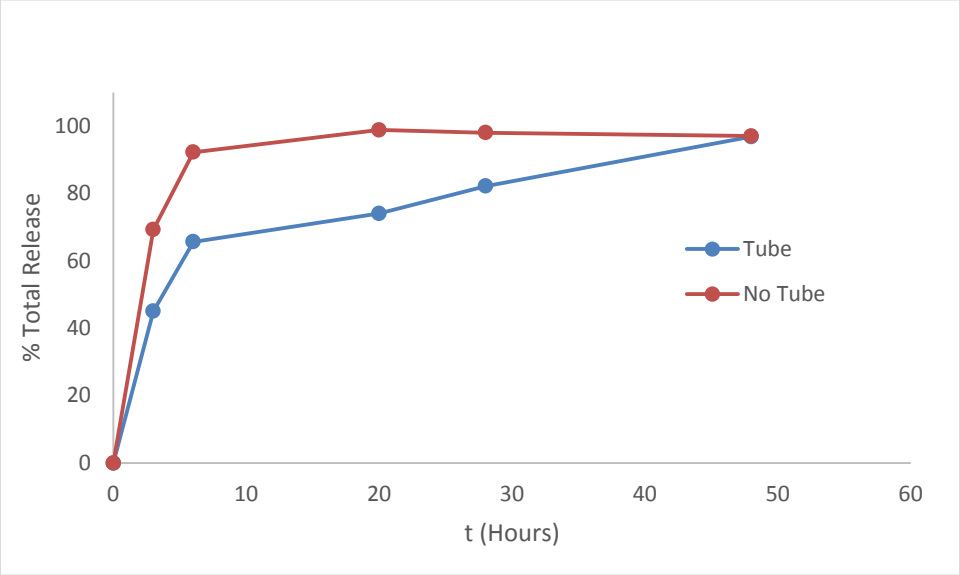

Figure 3.6. The percent release of the M1 scenario can been seen for 0, 3, 6, 20, 28, and 48 hours for the tube and no tube scenario.

Figure 3.7 shows a graphical representation of the relative percent release for scenario M2.

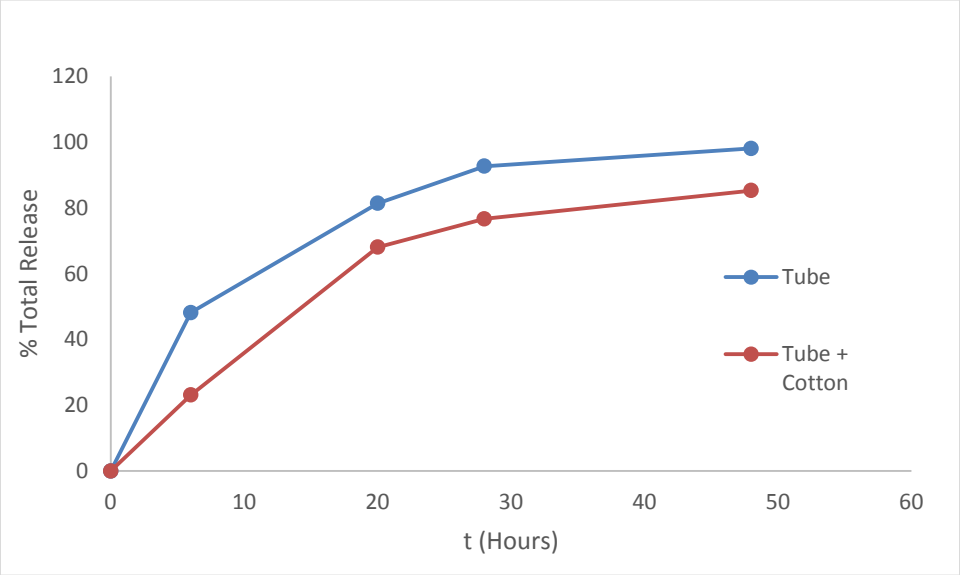

Figure 3.7. The percent release of the M2 scenario can been seen for 0, 6, 20, 28, and 48 hours for the tube with cotton and tube without cotton scenario.

3.4 Discussion and Conclusion

3.4.1 Multiple Site Background Removal

The background extraction method is not very sensitive to noise [122]. However, this method will only work if the width to the half maximum point is not within the boundary of the neighboring implantation site's width to half maximum distance. If this condition fails then the user must manually select the implantation sites. Figure 3.8 show a side by side comparison between the corrected and uncorrected concentration estimation methods.

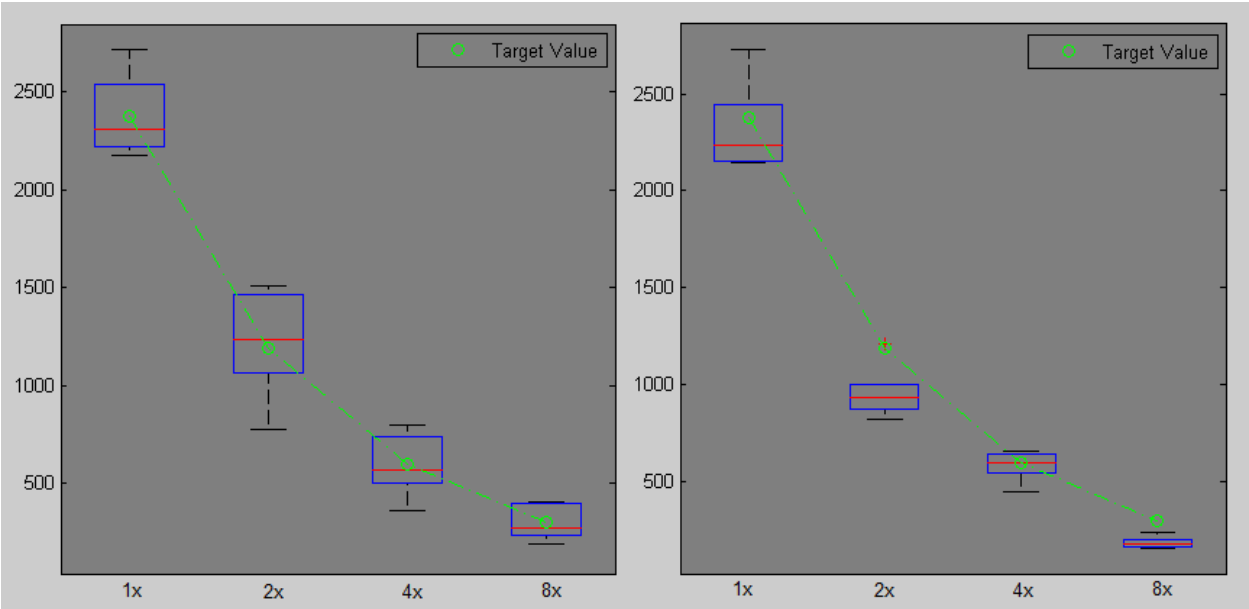

Figure 3.8. A box and whiskers plot of the corrected (left) and the uncorrected algorithm (right), with their associated targeted values in green. The vertical axis indicates the fluorescent intensity and the horizontal axis indicates the dilution ratio.

The corrected algorithms generally yielded much more accurate results compared with the uncorrected algorithm. The corrected algorithm mean difference was 2.78% for the 0.5x dilution for the target dilution value, with a relative accuracy of 5.56%. The corrected algorithm mean difference was 1.22% for the 0.25x dilution for the target dilution value, with a relative accuracy of 4.88%. The corrected algorithm mean difference was 1.42% for the 0.125x dilution for the target dilution value, with a relative accuracy of 11.36%. The uncorrected algorithm mean difference was 8.59% for the 0.5x dilution for the target dilution value, with a relative accuracy of 17.18%. The uncorrected algorithm mean difference was 1.03% for the 0.25x dilution for the target

dilution value, with a relative accuracy of 4.12%. The corrected algorithm mean difference was 4.37% for the 0.125x dilution for the target dilution value, with a relative accuracy of 34.96%.

The biggest difference between the corrected and uncorrected algorithms was seen on the 0.125x dilution site. The corrected algorithm was roughly 3 times more accurate than the uncorrected algorithm. This is in part due to the proximity of the 0.125x dilution to the 1x dilution. Since the small signal of the 0.125x site was overpowered by the 1x site the corrected algorithm had a very pronounced effect under these conditions.

The smallest difference between the corrected and uncorrected algorithms was seen on the 0.25x dilution site. The corrected algorithm was only slightly better than the uncorrected algorithm, which was in part due to the 0.25x site distance from the 1x site. Since there was not a much stronger signal nearby to contaminate the peak, the corrected algorithm did not make as big of an impact.

In general it can be seen that the proximity of neighboring peaks is an important factor when considering the usefulness of the correction algorithm. Certainly, the user must ultimately decide if their experimental conditions warrant the use of the corrected algorithm. Based on the results of this study, it will be advantageous to use the peak correction algorithm if neighboring peaks are with in close proximity and/or a small peak is near a large peak. Further studies will be aimed at a comprehensive peak intensity to neighboring peak distance examination. Since all the concentrations had the same

injected volume, it would be useful study the effect on volume size and concentration prediction accuracy since more dilute solutions may diffuse more easily.

In conclusion, this algorithm will help enable more accurate peak delineation and neighboring peak tail extrapolation and removal which will help investigators obtain more meaningful and accurate results from *in vivo* optical imaging studies.

3.4.2 Peak Tracking

The confined NMI of the contours were used to quantitatively access the accuracy of the tracked contours [29]. The tracking algorithm contour mapping quality improvement over direct deformation, and rigid registration was verified using confined NMI [103, 104]. NMI was used since other similarity metrics such as FSIM, RMSE, or cross correlation, include spatial information and will give a bias towards the rigidly registered contours since they have the same shape as the original contours, since the EPO has a tendency to diffuse and migrate within the mouse [106, 138, 139].

For the M1 scenario with no tube, the NMI for the deformed and tracked contours were the same for the 28-hour and 48-hour time points. This was due to the similarity cutoff criteria being reached for both of these cases. When the morphological similarity between the contours is below a cut off criteria then the tracked contour will revert back to the deformed contour. It is important to note that any confined NMI below 0.20 should be strongly suspected of being noise. Under this circumstance, the contours were manually double checked. It was confirmed, that the 28-hour and 48-hour time points had no visually detectable signal for the no tube scenario.

It is important to note that the M1 scenario tracking total release results indicate that the tube has a statistically significant increase in release time compared with the no tube implant scenario, with a p-value of 0.010005. Additionally, the M2 scenario tracking total release results indicate that the tube with cotton has a statistically significant increase in release time compared with the tube without cotton implant, with a p-value of 0.004892.

There are limitations to the fluorescence tracking algorithm. If the fluorescence signal migrates or diffuses too much the tracking algorithm will begin to fail. This is in part due to a restriction on the search range of the algorithm. If the algorithm searches too far, it may be more susceptible to picking up noise. Also, if the peak signal is not at least twice as strong as noise, it will assume there is no signal present, and revert back to using Canny DIR.

The peak tracking algorithm in general demonstrated more accurate implant tracking than the deformed or rigid registration algorithms. The implementation of the peak tracking algorithm reduces the experimental workload and helps reduce inter- and intra-user induced error and bias. This algorithm has the potential to increase the usefulness of the portable imaging software and make temporal tracking more accurate in the presence of implantation signal migration and diffusion.

3.5 Acknowledgements

This work was supported by grants from Progenitec Inc. and NIH AR064650-01 and EB014404-01.

CHAPTER 4

AUTOMATED RETINAL DEFORMATION AND DRUG DISPERSION TRACKING

4.1. Introduction

Posterior eye segment diseases such as age-related macular degeneration (AMD), diabetic retinopathy, glaucoma, and retinitis pigmentosa account for most cases of irreversible blindness world wide [140, 141]. Intraocular metastasis frequently arise in the choroid from women suffering from breast carcinoma and men diagnosed with lung carcinoma [142].

Treatment of the posterior segment is impeded by the difficulty of delivering effective doses of drugs to the posterior vitreous, retina, and choroid [143, 144]. Drugs administered topically may cross the conjunctiva and diffuse through the sclera, however this method usually does not result in therapeutic drug accumulation in the posterior vitreous [145, 146]. Systemic drug administration can deliver therapeutic drug levels to the posterior vitreous, however the large dose required often lead to adverse side effects [147]. The most direct method for posterior segment drug delivery is via intravitreal injection. Intravitreal injection is often associated with side effects such as hemorrhage, cataracts, endophthalmitis, and retinal detachment, so sustained release implants are often used to help reduce these adverse effects and increase the drug contact time [148, 149].

Currently, pharmacokinetic methods are used in most studies to assess drug release in vivo. Specifically, at the end of the study, retinal tissue and vitreous humor are

isolated. The drug in the tissue is then extracted and the amounts of drugs in tissue/fluid are then quantified using HPLC and/or Mass Spectrometry method [150, 151].

Recent developments in optical coherence tomography (OCT) and ultrasonic imaging of the posterior segment have shown potential in 3D eye structure rendering [152-154]. However, functional fluorescence imaging presents a challenge for OCT and ultrasound modalities. Positron emission tomography (PET) coupled with computed tomography (CT) or magnetic resonance imaging (MRI) are well suited for functional fluorescence image but suffer from insufficient resolution (~400X400 μm) to determine the concentrations and distribution of the drugs and nanoparticles in different regions of ocular tissues [155-157].

Ocular fluorescence imaging has shown potential in imaging nanoparticle accumulation in the vitreous [158-160]. Serial sectioning has emerged as a high resolution functional and structural imaging modality. Many slice correction techniques have been developed to help deal with segmentation distortion, however, think delicate structures such as the eye still present a challenge [161, 162].

Since manual retina delineation is cumbersome, advances in automated retina delineation algorithms using OCT has been a popular area of research in recent years [163-166]. However, automatic retina delineation using serial sectioning has not been well studied.

Thus, in order to track drug dispersion in the posterior eye segment as a function of time with high resolution a slice distortion correction algorithm needs to be developed in parallel with an automatic retinal delineation algorithm.

This study aims to develop a novel 3D ocular drug distribution model using serial sectioning fluorescent images. To achieve this, the authors have developed an automatic retina delineation algorithm, and an automatic slice distortion correction algorithm using autofluorescence images. Using a rabbit injection/implantation model, these algorithms are then implemented to track the dispersion as a function of time of a fluorescent-labeled model drug within the posterior retina using various drug delivery methods.

4.2 Methods and Materials

4.2.1 Animal Model / Implantation Procedure

All animals were male Dutch Belted Rabbits in good health, weighing approximately 2 lbs, from Murtle's Rabbitry (Thompsons Station, Tennessee). Five animals per group were evaluated. For each ocular site and time point, animals were treated with single injection or treatment.

For the eye drop experiment, only locally anesthesia with oxybuprocain (0.4%) eye drops was required. Each rabbit was sedated with an intramuscular injection of a mixture of ketamine (35 mg/kg) and xylazine hydrochloride (5 mg/kg). The fluorescein (Aldrich, Milwaukee, WI, USA, provided by Alcon Laboratory) was used as a model drug which was delivered to the ocular tissues via injection or slow release devices. For injection, 50 µl of fluorescence dye was applied topically or injected into subconjunctival, intravitreal and sub-tenon spaces. In addition, fluorescence dye-

containing phospholipids implants were implanted into aqueous humor, subconjunctival, intravitreal, and sub-tenon spaces.

For subconjunctival implantation, the rabbits were administered or implanted subconjunctivally in the supratemporal quadrant of the eyes with fluorescein solution or fluorescein-embedded phospholipid implants (drug delivery devices), respectively [167].

In the case of intravitreal implantation, pupils were dilated with topical 10% phenylephrine and 0.5% tropicamide before surgery. Under local anesthesia with oxybuprocain 0.4%, a lid speculum was placed and a transconjunctival incision of the sclera was made in the temporo-superior quadrant of the eye at 3 mm from the limbus under a surgical microscope. A 23 gauge needle were then inserted in the vitreous cavity with a glass slide over the cornea to allow visual control of the needle, after which the fluorescein solution or drug delivery devices was inserted into the vitreous space and then fixed to the vitreous wall [168]. Poly-N-isopropylamide (PNIPAM) nanoparticle labeled with fluorescein isothiocyanate (FITC), were injected intravitreally with a concentration of (0.5µg/25µl).

Some of the animals underwent sub-tenon via fluorescein injection or fluorescein releasing device implantation [169].

4.2.2 Tissue Collection and Analysis

At the end of the study, rabbits were sacrificed and the eyes were then enucleated. Each eye ball was sectioned (~10 µm/section) and scanned using the Genepix 4000B

(Axon Instruments, Inc., Union City, CA). Table 4.1 shows the complete administration protocol.

Table 4.1. The various injection/implantation sites are listed on the left, while the imaging time is indicated on the top of the table.

	2 hours	4 hours	1 day	2 days	4 days	7 days
Cornea/Anterior Sub-tenon	Topical	Topical	Topical /Implants	implants	Implants	Implants
Intravitreal	Injection	Injection	Injection / Implants	Injection / Implants	Implants	Implants
Subconjunctival	Injection	Injection	Injection / Implants	Injection / Implants	Implants	Implants
Sub-Tenon	Injection	Injection	Injection / Implants	Injection / Implants	Implants	Implants

4.2.3 Image Processing Overview

During the eye segmentation stage, the eye slices get distorted and deformed by the blade. Since eye shapes and sizes vary between individuals pre-defining the morphology of an eye can generate unrealistic structural shapes. To overcome this limitation, an in-house software platform was developed called EyeMesh. EyeMesh was developed using C++ and Nvidia's compute unified design architecture (CUDA). EyeMesh allows the user to choose between semi-automatic and fully-automatic distortion correction modes. The semi-automatic mode allows the user to manually deform and manipulate a sparse subset of eye slices, which are then used to interpolate intermediate slices. The fully-automatic mode uses a flexible eye template based on

preexisting eye measurements, to guide a distortion correction algorithm. A workflow of the slice correction process can be seen in figure 4.1.

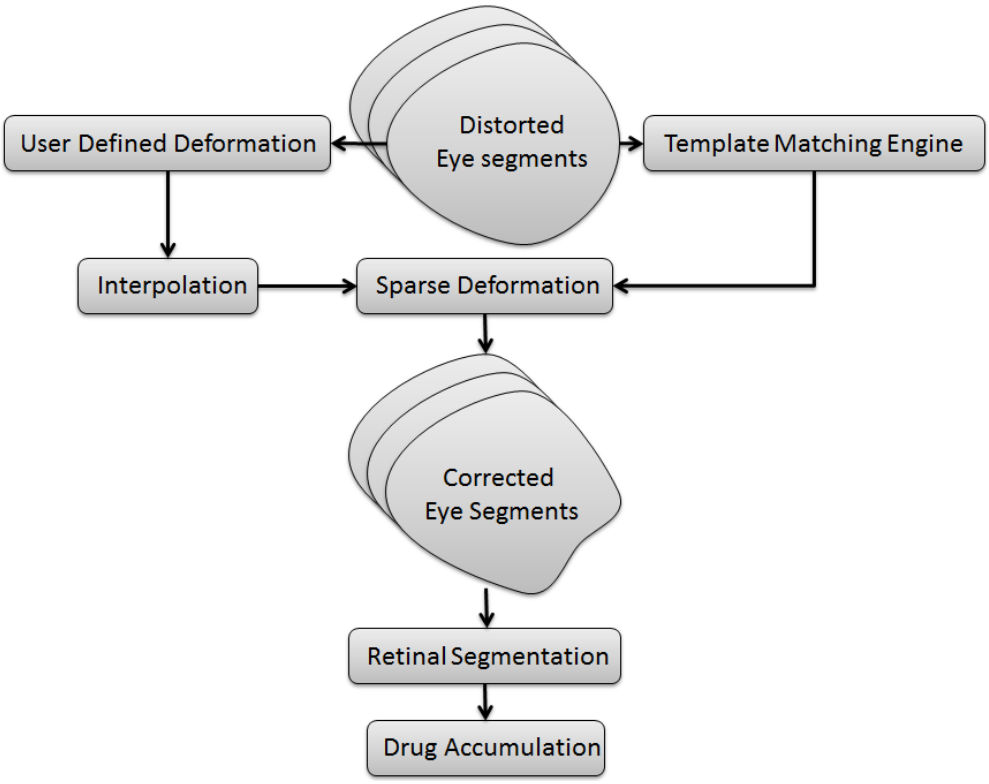

Figure 4.1. Workflow of the algorithm

4.2.4 Semi-Automatic Slice Registration

EyeMesh utilizes a click and drag deformable image registration (DIR) function. This allows users to manually click on an eye slice and pull the structure to the desired location. After each mouse click, mouse movement generates a deformation vector field (DVF) in the direction of the mouse movement. The image is updated every 0.1 seconds

until the mouse button is released. All DVFs are stored and accumulated using the Veracuteren formula [86].

Once the manually deformed images are generated a rough outline of the eye boundary is created using matching squares [96]. The boundary outline is then down-sampled and up-sampled using cubic interpolation [170]. This process helps smooth out any roughness from the manual manipulation. Figure 4.2 demonstrates the workflow of the click and drag DIR function and illustrates the cubic interpolation process.

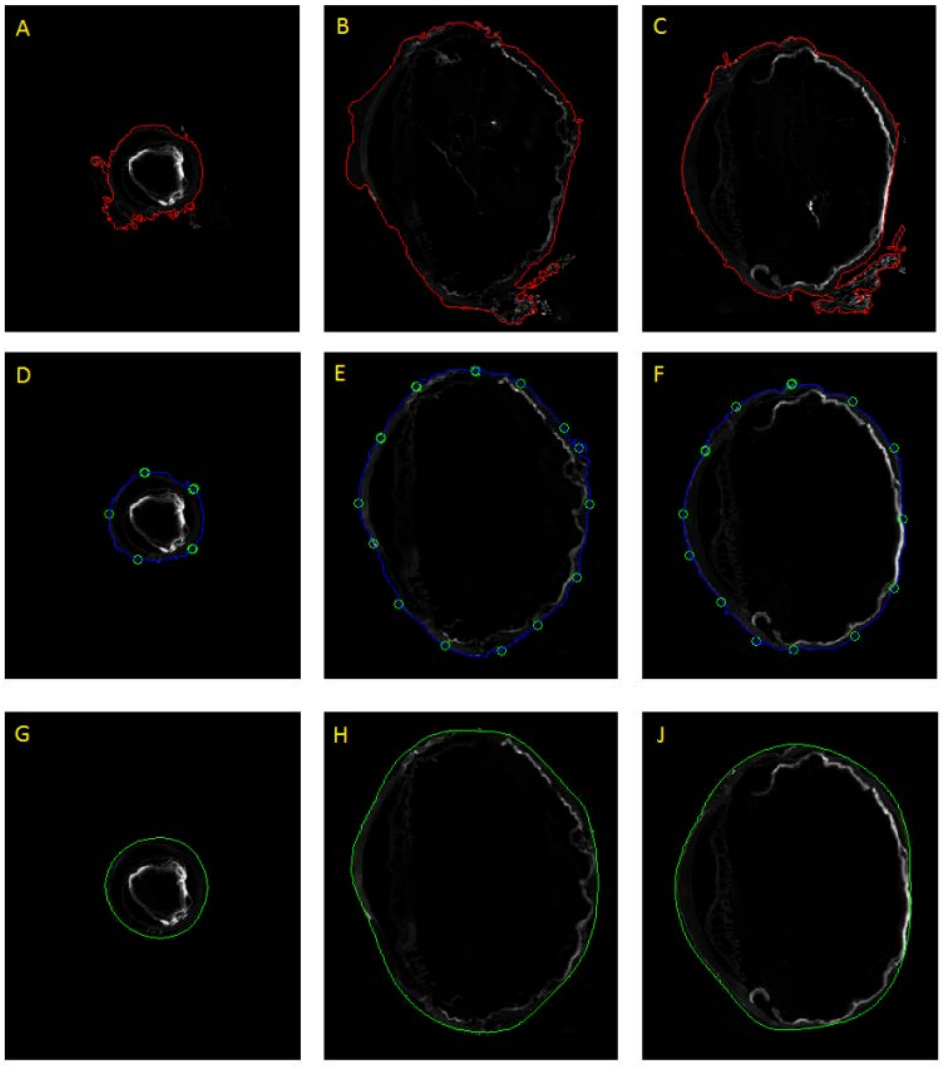

Figure 4.2. Images A-C represent the original unprocessed slices. The red line represents the largest connected closed image component. Images D-F represent the processed slices using EyeMesh. The blue line represents the largest connected closed image component and the green circle represent a sparse subset of points used for the nodes in the cubic interpolation. Images G-J represent the cubic interpolation of images D-F. The green line represents the cubic line interpolation result.

Once a sparse subset of slices are manually generated a cubic variant of mean squared interpolation is implemented to generate the outlines of all intermediate slices [171, 172]. Figure 4.3 shows the interpolated slices of the intermediate eye segments.

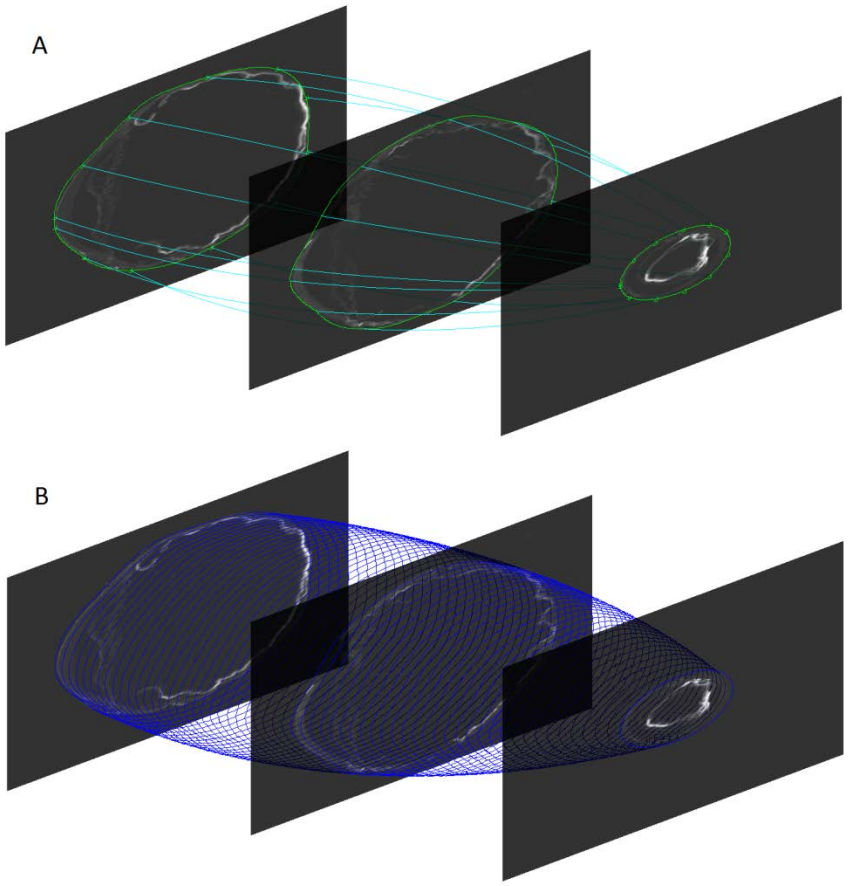

Figure 4.3. Image set A represents consecutive slices 1, 75, and 150 with the inter-slice cubic interpolation indicated by the teal lines. Image set B represents the contour as a blue line of each interpolated slice.

4.2.5 Automatic Slice Registration

Contingent on the individual user requirements, a fully automatic template matching algorithm was developed in parallel. EyeMesh allows the user to fit the eye slices to a flexible template. The automatic registration scheme is initialized as an optimization problem.

To increase computational efficiency and help the objective function converge, a hierarchal scheme is implemented. First, a flexible ellipse E_f with radii r_1, and r_2 is fitted to the outer border of the eye segment B_{eye} rotated by a rotational matrix M_θ of angle Θ. The outer edge of the cornea is initially modeled with C_r. Θ, r_1, and r_2 are shifted until Q is minimized for iteration (n) at slice (s).

$$Q(\theta, r_1, r_2)_s^n = \min \left\| \left(B_{eye} \bullet M_\theta - E_f(r_1, r_2) - C_r \right)^2 \right\|_s^n$$

$$(\theta, r_1, r_2)_s^n = \arg\min Q(\theta, r_1, r_2)_s^n$$

Once an ellipse (E_r) is determined and a corresponding rotated eye segment (B_r) is determined, the flexible outer boundary of the cornea C_f is modeled with a 3rd order polynomial and superimposed on the anterior corner of E_r. The corresponding coefficients P_4, P_3, P_2, and P_1 of the corneal polynomial are shifted until Γ is minimized.

$$\Gamma(P_1, P_2, P_3, P_4)_s^n = \min \left\| B_r - (E_r + C_f(P_1, P_2, P_3, P_4)) \right\|_s^n$$

$$(P_1, P_2, P_3, P_4)_s^n = \arg\min \Gamma(P_1, P_2, P_3, P_4)_s^n$$

C_r is obtained by applying coefficients P_4, P_3, P_2, and P_1. C_r and E_r are iteratively combined to form a flexible template T_f and a weighted difference with B_r is computed. Pixels that reside inside the T_f and outside B_r are assigned penalty P_1 and pixels that reside outside T_f and inside B_r are assigned a penalty P_2. Mismatch between T_f and B_r penalizes the objective function Ψ, where

$$\Psi_{slice}^n = \sum_{\#voxels} (P_1 + P_2)_{slice}^{n+1} \Big/ \sum_{\#voxels} (P_1 + P_2)_{slice}^n .$$

The initial starting conditions for the eye template's corresponding radii and corneal curvature are taken from previous average measurements of the rabbit eye [173].

Since the assumption of convexity in the solution space is often times invalid, a global optimization followed by a local optimization is implemented to minimize Γ and Q. A graphic processor based (GPU) open source optimization engine was implemented using simulated annealing and the Nelder-Mead method [174]. Figure 4.4 shows a graphical representation of the automatic registration process.

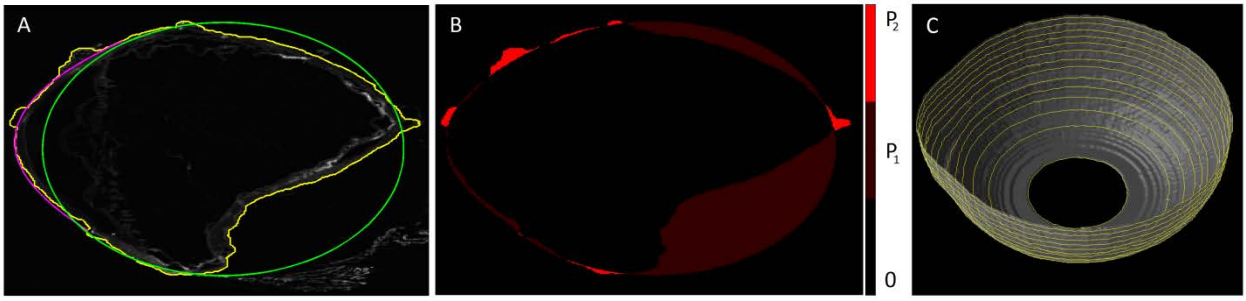

Figure 4.4. Image A shows B_r in yellow, C_r in pink and E_r in green. Image B shows a penalty map with user defined penalty p_2 represented in bright red and user defined penalty P_1 represented as dark red. Image C shows every tenth slice of T_f in yellow superimposed on the corresponding T_f surface mesh.

4.2.6 Sparse Matrix Deformation

Once a boundary for each slice has been generated, the weighted least squared distances WLSD for each point on the original contour outline C_{moving}, and each point on the template contour C_{static} is calculated as follows,

$$\sum_{i}\sum_{j,} WLSD_{i,j} = \sqrt{\left(C^{i}_{moving} - C^{j}_{static}\right)^{2}},$$

Where *i* represents the index of C_{moving} and j represents the index of C_{static}. The minimum of the j^{th} index of i represents the corresponding DVF between point C^{j}_{static} and C^{i}_{moving}. The offsets are utilized to populate the complete 2 dimensional DVF using sparse interpolation. The raw slice $Slice_{raw}$ is then deformed using sparse interpolant to form the deformed slice $Slice_{deformed}$ [29, 30]. Figure 4.5 shows the sparse DVF between C_{ststic} and C_{moving} and the complete DVF between $Slice_{deformed}$ and $Slice_{raw}$.

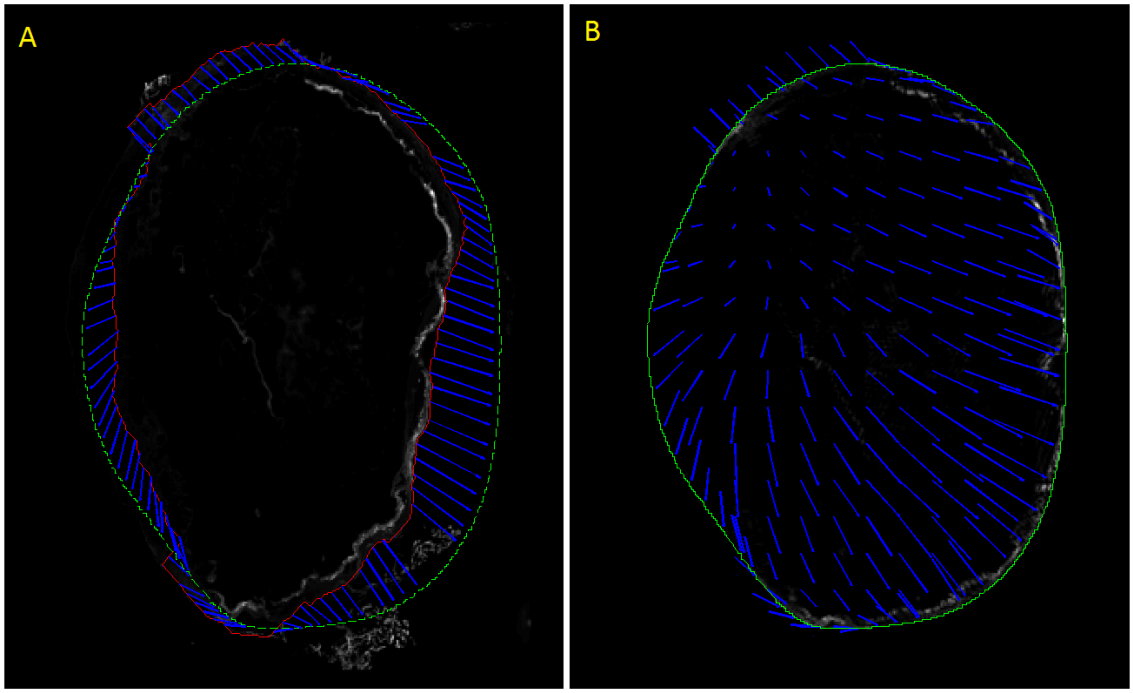

Figure 4.5. Image A shows the outline of $Slice_{raw}$ represented as a red line and the dashed green line represents the interpolated slice. The blue arrows represent the sparse deformation vector field. Image B shows $Slice_{deformed}$ with the green line representing the interpolated slice and the blue arrows showing the interpolated deformation vector field.

4.2.7 Retinal accumulation

Once all the slices are deformed the two edge detection techniques are combined to find the sclera and retina on the $Slice_{deformed}$. Intensity edges are found using thresholding and gradient edges are generated using canny edge detection [69, 73]. Since canny edges can be sensitive to noise a continuity constraint is applied to limit the edge outputs to smooth continuous edges, and morphological thinning is implemented to help improve the accuracy of the canny edge algorithm [72, 74]. Similarly, closed loop threshold edges are mapped to a binary image, flood filled, contracted, small speck filtered, then dilated [175, 176]. A ray tracing method is implemented using Siddon's algorithm from the center of mass to each vertex point along the outermost combined edge [177]. The anterior region, retina, and sclera are spatially mapped based on the corresponding path lengths of each ray trace. Figure 4.6 shows the graphical representation of the auto-segmentation process.

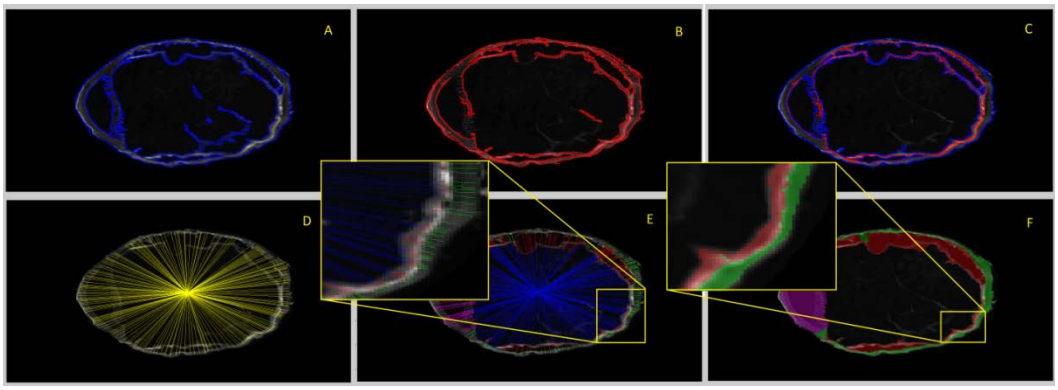

Figure 4.6. Image A represents a preprocessed threshold. Image B shows the enhanced canny edges. Image C shows the combined processed threshold and enhanced canny edges. Image D shows a subset of ray tracing paths. Image E shows the various path lengths, where green represents the scleral length, red represents the retinal length, purple represents the anterior region length, and blue represents the vitreous humour. Image F shows the various areas, where green represents the sclera, red represents the retina, and purple represents the anterior region.

Once all the regions are mapped, a shell of the eye is formed from the outlines of all the $Slice_{deformed}$ sections. The shell surface mesh is calculated using marching cubes [178, 179]. The center of mass of the $Slice_{deformed}$ is calculated and used as a reference to accumulate voxel values on the eye surface. Figure 7 shows a 3D intensity distribution, ray tracing paths, and the vertex accumulation of the voxel intensities within the eye contained inside the surface mesh.

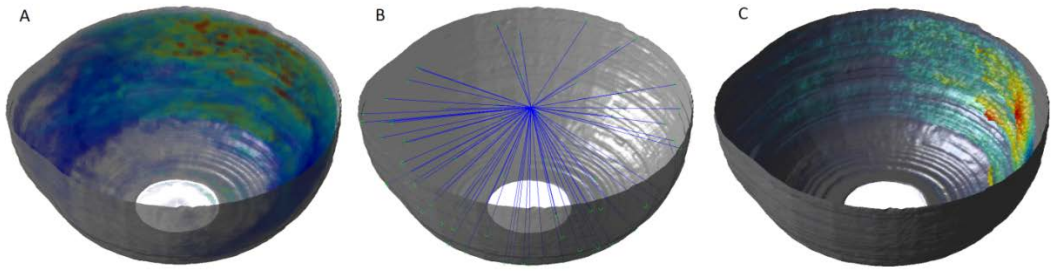

Figure 4.7. Image A represents the eye shell with a 3D distribution of dye. Image B shows a sparse subset of line paths used to accumulate voxel intensities on each surface vertex. Image C shows the topographic map of the voxel intensity accumulation on the eye surface mesh.

The various steps of the process are implemented as follows:

Algorithm 1:

1. **If:** Semi-Automatic Registration
    A. Sparse Manual Slice Manipulation
    B. Inter Slice Cubic interpolation
1. **If:** Automatic Registration
    Loop: 1 through number of slices
        Loop: 1:interation number
        Minimize Q
        Minimize Γ
        end
    end
2. Deformation
    Loop: 1 through number of slices
        Loop: 1 through number points on the slice boundary
        Compute WLSD
        end
    Compute the sparse interpolant
    Populate the 2D DVF
    Deform the slice
    end
3. Construct the eye surface mesh
4. Auto-segmentation
5. Accumulate dye
    Loop: 1 though number of surface vertices
    Raytracing
    end

4.3 Results

4.3.1 Slice Distortion Correction

In order to access the accuracy of the semi-automatic and automatic registration all eye slices were manually registered. The resulting automatic and semi-automatic registrations were evaluated using normalized least squared differences. Figure 4.8 shows a comparison between the normalized least squared differences (NLSD) of the semi-automatic and automatic registration techniques for different number of manually registered slices [180].

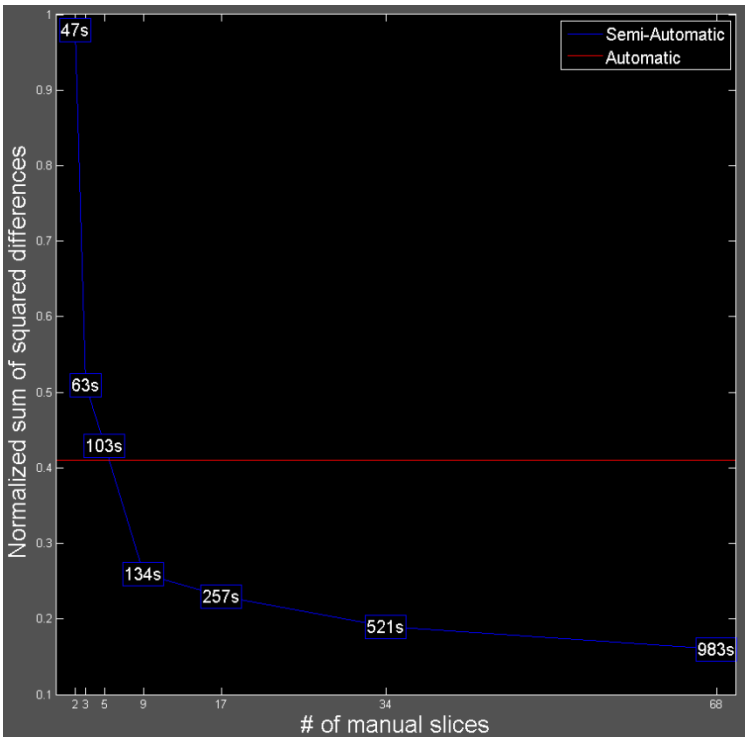

Figure 4.8. The blue line represents the semi-automatic registration results, with the manual registration time in seconds (s) shown in white. The red line represents the fully automatic result. The results generated from the mean NLSD, and time values of all IV data.

4.3.2 Tissue Segmentation

To evaluate the accuracy of the retinal segmentation algorithm, five retinas were manually contoured. The SSD between all manually contoured sets were calculated [181]. Then the SSD between the retinal segmentation algorithm and each manually contoured retina was calculated. Table 4.2 shows the values for each of the comparisons.

Table 4.2. The Average SSD's between sample combinations are shown for the automatic and manually contoured (top) and between manually contoured trials (bottom).

Combination	1		2		3		4		5	
Automatic	1.494		1.018		2.63		1.282		2.76	
Combination	1,2	1,3	1,4	1,5	2,3	2,4	2,5	3,4	3,5	4,5
Hand Contoured	1.192	1.706	2.188	2.172	2.336	2.298	1.868	1.28	2.504	1.484

A pilot study using the completely randomized (CR) design was conducted to determine the minimum sample size necessary to test if the SSD's obtained from the retinal segmentation algorithm and the manually contoured retina are the same with in the 95% confidence interval [182, 183]. If x = target value – automatic value, y = target value – hand contoured value, $Sx^2 = \frac{\sum_i^n (xi-\bar{x})^2}{n-1}$, $Sy^2 = \frac{\sum_i^m (yi-\bar{y})^2}{m-1}$, $Sig^2 = \frac{\left((n-1)Sx^2+(m-1)Sy^2\right)}{n*m-2}$, then the sample size $= \frac{2(Z_\propto{}^2 - Z_1 - \beta_0)^2}{\delta_0}$ (Sig^2), were n = 5, m = 10, $\propto = 0.05$, $Z_\propto{}^2$ = 1.96, Z_1 = -1.64, β_0 = 0, and δ_0 = 1. The CR design gives a minimum sample size of 2.45 or 3 eyes in order to determine if the means from the retinal segmentation algorithm and the manually contoured retina are indistinguishable.

We test the null hypothesis H0: ux = uy with an alpha of 0.5. The degrees of freedom are calculated as follows, $V = \frac{\left(\frac{std_x^2}{n}+\frac{std_y^2}{m}\right)^2}{\frac{\left(\frac{std_x^2}{n}\right)^2}{n-1}+\frac{\left(\frac{std_y^2}{m}\right)^2}{m-1}} = 5.69 \approx 6$, where std_x = 0.7179, and std_y = 0.4436 [184]. Next t_0^* is calculated, $t_0^* = \frac{u_x-u_y}{\sqrt{\frac{std_x^2}{n}+\frac{std_y^2}{m}}}$ = -0.189, where u_x = 1.837, u_y = 1.903 [184]. We cannot reject the null hypotheses since $\pm t_{0.025,6}$ = ±2.447 [184]. Therefore, using the CR design the difference between the manually contoured and retinal segmentation algorithm SSDs means are not significantly different.

4.3.3 Deformation Sampling Error

To access the sampling effect of the sparse deformation, the retinal drug accumulation was calculated before and after deformation with 5 eyes for the intravitrial implant. The Absolute difference in drug accumulation has an average of 3.23% between the deformed image and the original image. Figure 4.9 shows a graphical representation of the retinal drug accumulation before and after deformation.

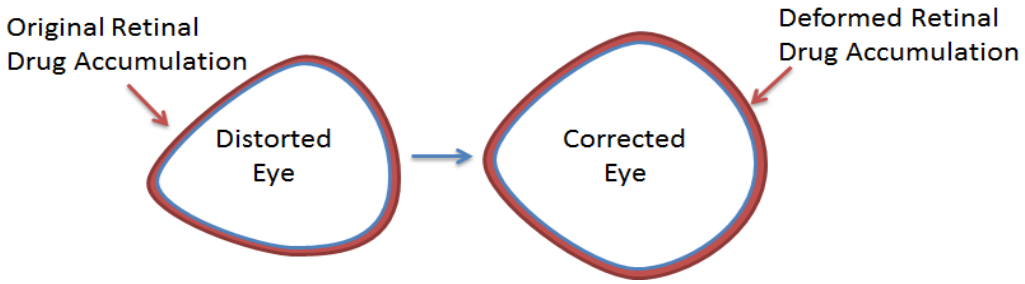

Figure 4.9. A schematic of the original retinal drug accumulation calculated before (left) and after (right) deformation.

4.3.4 Drug Accumulation

To evaluate the relative drug distribution at different time points using different delivery techniques the retina was subdivided into 8 regions. The 8 eye regions were divided based on their relative distance from the optic nerve, which was defined manually. The optic nerve region represents the closest 20^{th} percentile distance. The posterior right and left region are within the 20^{th} and 40^{th} percentile distance. The middle right and left region are within the 40^{th} and 60^{th} percentile distance. The anterior right and left region are within the 60^{th} and 80^{th} percentile distance. The anterior region is within the 80^{th} and 100^{th} percentile distance. Figure 4.6 graphically demonstrates how the eye is subdivided.

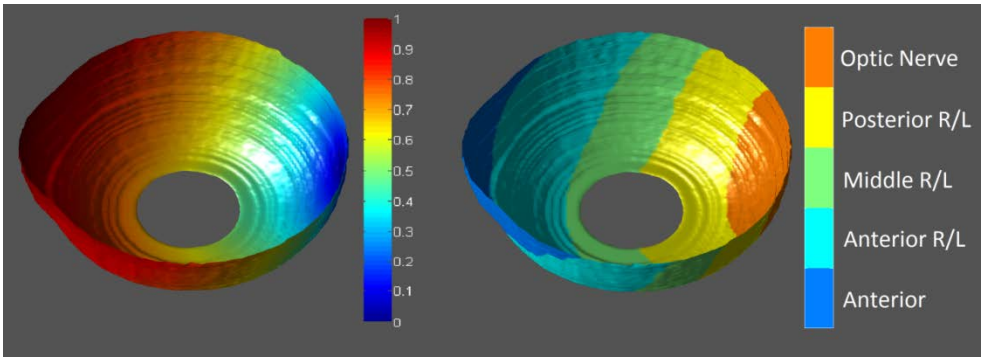

Figure 4.6. The left side of the image shows a normalized distance map of each point on the surface to the center of the optic nerve point. The right side of the image shows how the eye regions are subdivided according to their relative distances to the optic nerve center.

Table 4.3 shows a comparison between the AS, IV, SC, and ST for 1 day, 2 days, 4 days, 7 days after the implantation.

Table 4.3. The mean normalized implantation values for the, intravitreal (IV), Sub-Tenon Spaces (ST), Sub-Conjunctival (SC), Aqueous Humor (AH). The various implantation methods are shown for the anterior, anterior right, anterior left, middle right, middle left, posterior right, posterior left, and the optic nerve.

		Anterior	Anterior Right	Anterior Left	Middle Right	Middle Left	Posterior Right	Posterior Left	Optic Nerve
1 Day	IV	0.11 +/- 0.03	0.20 +/- 0.08	0.23 +/- 0.08	0.45 +/- 0.13	0.35 +/- 0.18	0.47 +/- 0.17	0.56 +/- 0.16	0.66 +/- 0.29
	ST	0.43 +/- 0.12	0.48 +/- 0.13	0.48 +/- 0.14	0.43 +/- 0.14	0.35 +/- 0.13	0.43 +/- 0.10	0.48 +/- 0.13	0.52 +/- 0.14
	SC	0.26 +/- 0.05	0.39 +/- 0.09	0.31 +/- 0.14	0.51 +/- 0.15	0.38 +/- 0.15	0.40 +/- 0.13	0.31 +/- 0.12	0.27 +/- 0.06
	AH	0.80 +/- 0.31	0.38 +/- 0.15	0.42 +/- 0.17	0.16 +/- 0.06	0.12 +/- 0.06	0.09 +/- 0.02	0.11 +/- 0.05	0.18 +/- 0.04
2 Days	IV	0.13 +/- 0.04	0.37 +/- 0.12	0.43 +/- 0.16	0.76 +/- 0.25	0.55 +/- 0.24	0.66 +/- 0.19	0.72 +/- 0.23	0.64 +/- 0.24
	ST	0.39 +/- 0.11	0.51 +/- 0.11	0.46 +/- 0.20	0.73 +/- 0.25	0.47 +/- 0.19	0.50 +/- 0.16	0.67 +/- 0.18	0.45 +/- 0.16
	SC	0.44 +/- 0.17	0.49 +/- 0.14	0.52 +/- 0.17	0.50 +/- 0.15	0.44 +/- 0.16	0.48 +/- 0.12	0.39 +/- 0.09	0.25 +/- 0.04
	AH	1.00 +/- 0.19	0.56 +/- 0.13	0.59 +/- 0.18	0.25 +/- 0.13	0.22 +/- 0.06	0.21 +/- 0.08	0.20 +/- 0.07	0.15 +/- 0.04
4 Days	IV	0.22 +/- 0.07	0.58 +/- 0.17	0.42 +/- 0.21	0.65 +/- 0.21	0.90 +/- 0.23	0.80 +/- 0.20	0.57 +/- 0.25	0.68 +/- 0.21
	ST	0.46 +/- 0.10	0.61 +/- 0.25	0.68 +/- 0.19	0.97 +/- 0.26	0.84 +/- 0.30	0.75 +/- 0.18	0.58 +/- 0.17	0.47 +/- 0.13
	SC	0.62 +/- 0.23	0.73 +/- 0.24	0.88 +/- 0.26	0.97 +/- 0.25	0.98 +/- 0.19	1.00 +/- 0.26	0.79 +/- 0.25	0.23 +/- 0.06
	AH	0.88 +/- 0.24	0.63 +/- 0.23	0.65 +/- 0.11	0.45 +/- 0.08	0.44 +/- 0.11	0.37 +/- 0.06	0.32 +/- 0.13	0.14 +/- 0.05
7 Days	IV	0.23 +/- 0.08	0.52 +/- 0.20	0.48 +/- 0.20	1.00 +/- 0.28	0.94 +/- 0.19	0.76 +/- 0.28	0.78 +/- 0.22	0.69 +/- 0.15
	ST	0.45 +/- 0.14	0.66 +/- 0.20	0.66 +/- 0.23	0.88 +/- 0.24	1.00 +/- 0.34	0.59 +/- 0.23	0.60 +/- 0.17	0.52 +/- 0.10
	SC	0.71 +/- 0.33	0.57 +/- 0.26	0.72 +/- 0.17	0.98 +/- 0.29	0.86 +/- 0.25	0.59 +/- 0.16	0.45 +/- 0.14	0.26 +/- 0.09
	AH	0.55 +/- 0.25	0.51 +/- 0.13	0.58 +/- 0.17	0.40 +/- 0.18	0.38 +/- 0.16	0.26 +/- 0.11	0.29 +/- 0.11	0.12 +/- 0.04

Figure 4.10 shows a 3d comparison distribution between day 1, day 4, and day 7 after IV injection.

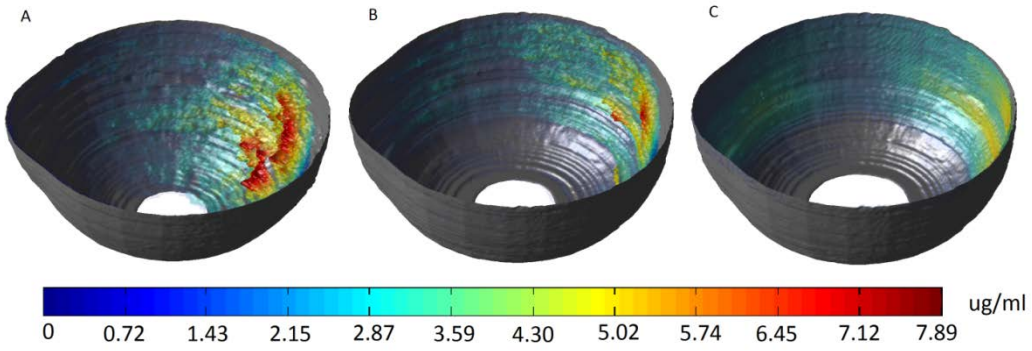

Figure 4.10. Image A represents day 1, image B represents day 4 after injection, and image C represents day 7 after injections.

Figure 4.11 shows a 3d distribution of the IV implantation methods using a smoothing kernal.

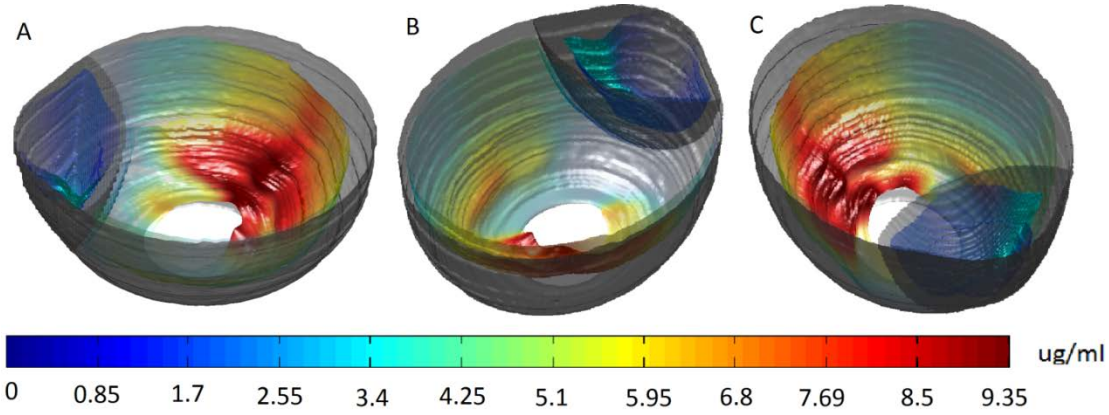

Figure 4.11. Images A-C represent day 2 of implantation retinal intensity distribution using IV delivery method at 0° (A), 120°, and 240°. The retinal drug distribution is shown in transparent false color with the eye boundary shown in transparent grey.

4.4 Discussion and Conclusion

The large NLSD between 3 and 2 manually registered slices is a result of the different interpolation techniques. 2 manual slices forces a linear interpolation [185]. 3 or more manual slices allows for cubic interpolation which will produces lower NLSD values [186].

The automatic registration performs slightly better than the semi-automatic registration with 5 manually slices. An additional 13% decrease can be achieved by using 9 manually registered slices, after that point there is diminished improvement for the amount of additional user input time.

To access the relative distributions from each implantation site as a function of time, the mean intensity and standard deviation of the various retinal regions were normalized from 0 to 1. Figure 4.12 shows the relative mean intensity and relative standard deviation of the various regions of the retina of the different implantation methods.

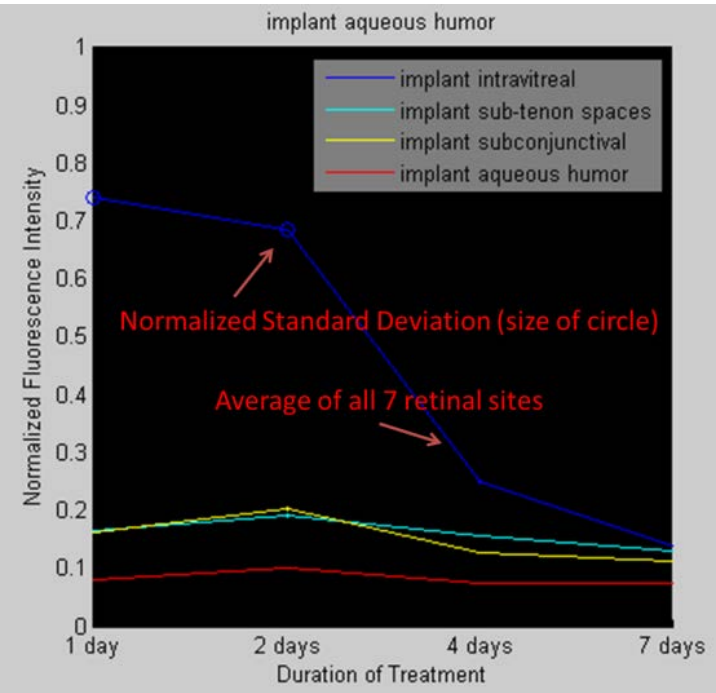

Figure 4.12. The mean relative regional distributions from each implantation site as a function of time as shown with the standard deviation represented as a size of the circle at each time point.

The IV method shows the highest overall retinal accumulation during the first 4 days in figure 4.12. This behavior is consistent with our expectation since the drug is being release towards the posterior interior wall of the vitreous.

Table 4.3 is used to determine if the IV implantation method is distinguishable from the other implantation methods. A decision on whether or not the IV method is distinguishable from the other methods based on the mean and variances of the corresponding sample distributions. If we aim to test the null hypothesis that u_1-u_2 = 0, then $t_0 = \frac{\overline{x_1} - \overline{x_2}}{s_p\sqrt{\frac{2}{n}}}$, where $\overline{x_1}$ is the mean of the IV method, $\overline{x_2}$ is the mean of the method being

tested, n is the sample size of 5, and $S_p = \sqrt{\frac{(n-1)S_1^2 + (n-1)S_2^2}{2n-2}}$, where S_1 is the variance of the IV method, and S_2 is the variance of the method being tested. A look up table was used to determine the confidence interval of the associate method and retinal region [184]. Table 4.4 shows a complete statistical analysis of the confidence intervals of the various implantation methods compared with the IV method for all retinal regions.

Table 4.4. The confidence intervals of the various implantation methods compared with the IV method for all retinal regions. The negative sign in front of the confidence interval indicates the mean IV value was less than the compared implantation method mean value.

		Anterior (%)	Anterior Right (%)	Anterior Left (%)	Middle Right (%)	Middle Left (%)	Posterior Right (%)	Posterior Left (%)	Optic Nerve (%)
Day 1	ST	-99.95	-99.95	-99.95	90.00	>60.00	99.00	99.95	99.50
	SC	-99.95	-99.95	-99.95	-99.90	-90.00	99.90	99.95	99.95
	AH	-99.95	-99.95	-99.95	99.95	99.95	99.95	99.95	99.95
Day 2	ST	-99.95	-99.95	-90.00	75.00	97.50	99.95	90.00	99.95
	SC	-99.95	-99.95	-99.95	99.95	99.75	99.95	99.95	99.95
	AH	-99.95	-99.95	-99.95	99.95	99.95	99.95	99.95	99.95
Day 4	ST	-99.95	-75.00	-99.95	-99.95	75.00	95.00	-60.00	99.95
	SC	-99.95	-99.95	-99.95	-99.95	-97.50	-99.95	-99.95	99.95
	AH	-99.95	-90.00	-99.95	99.95	99.95	99.95	99.95	99.95
Day 7	ST	-99.95	-99.95	-99.95	97.50	-75.00	99.75	99.95	99.95
	SC	-99.95	-90.00	-99.95	60.00	97.50	99.90	99.95	99.95
	AH	-99.95	60.00	-99.90	99.95	99.95	99.95	99.95	99.95

From table 4.4 it can be seen that the relative optic nerve concentration for the IV method is greater than all other implantation methods with a confidence interval of 99.95%. It can also be seen, that the relative anterior concentration for the IV method is

lesser than all other implantation methods with a confidence interval of 99.95%, and that the relative posterior right and posterior left concentrations for the IV method is greater than all other implantation methods with a confidence interval of 99.95% for days 1 and 2.

To access the relative regional distributions, the mean intensity and standard deviation of the various retinal regions were normalized from 0 to 1. Figure 4.13 shows the relative mean intensity and relative standard deviation of the various regions of the retina for each implantation method.

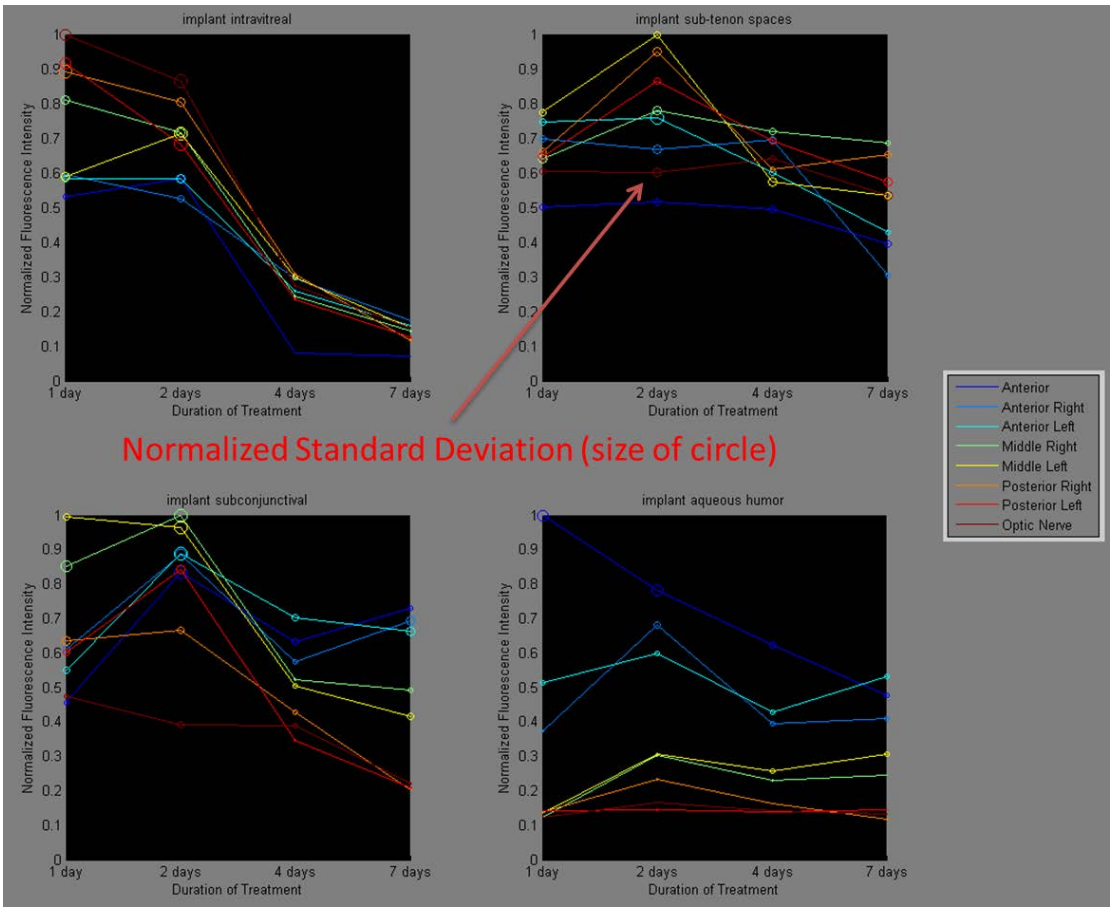

Figure 4.13. The data shows the average of all the retinal regions of the mean normalized implantation values for the, intravitreal, Sub-Tenon Spaces, Sub-Conjunctival, Aqueous Humor. value for each method for all the various implantation methods are shown for the anterior, anterior right, anterior left, middle right, middle left, posterior right, posterior left, and the optic nerve.

As demonstrated from figure 4.13, the relative intensities near the optic nerve, and the posterior right and left retina are the highest for the first two days for the IV implantation method. This behavior is expected since the model drug is released near the optic nerve.

Future work will incorporate relative retinal uptake compared with the total drug accumulation within all the eye structures, such as the vitreous, and the sclera.

In this paper, we detailed the feasibility of serial sectioning drug imaging to the posterior vitreous. Novel methods have been developed to correct for slice distortion during segmentation. An auto-segmentation framework has been developed to automatically register the retinal sclera interface. The entire process has been packaged into EyeMesh using a powerful CUDA/C++ computational engine [187, 188].

Utilizing the EyeMesh framework a user can produce high quality functional and structural images that can help track drug tissue accumulation and distribution in the posterior eye segment with little or no manual manipulation.

4.5 Acknowledgements

This work was supported by a grant from Progenitec Inc.

CHAPTER 5

AUTOMATED LANDMARK-GUIDED DEFORMABLE IMAGE REGISTRATION

5. 1. Introduction

The goal of radiotherapy is to deliver a tumorcidal dose to the target while simultaneously sparing neighboring normal tissue and critical structures. Conventionally, a treatment plan is generated on simulation CT images, then subsequently delivered over a treatment course lasting for many weeks with minimal adaptive replanning [189, 190]. However, anatomical changes that occur during this time may degrade the accuracy of radiation therapy.

On-board Cone-beam CT (CBCT) scans are often used for patient positioning prior to radiation therapy treatment. Several studies have been conducted using CBCT images for dose calculation [191-195]. However, low image quality of the CBCT images makes direct dose calculation less accurate based on CBCT than based on conventional CT because of inaccurate Hounsfield Unit (HU) assignment. If the CBCT can be accurately deformably registered to the original planning CT, the dose can be calculated on the deformed CT, producing much more reliable dosimetric results [196-198].

The differences in imaging techniques between CT and CBCT scans lead to nonlinear intensity inconsistencies between corresponding anatomical regions, mainly due to higher scattering in the CBCT images [199, 200]. Although many different scatter correction techniques have been studied, CBCT scatter contamination is still an open problem [201-204]. Since gray-scale based deformable image registration (DIR) relies on

image intensity similarities between corresponding anatomical structures, an intensity correction step must be implemented to allow for accurate DIR between the CBCT and planning CT images. Many different intensity correction approaches have been demonstrated to help increase the accuracy of inter-modality DIR, such as, polynomial intensity transform [205, 206], histogram matching intensity redistribution [207], and iterative intensity matching in conjunction with a tissue specific intensity transformation [208]. The transformation of the global intensity histogram is also used to guide the objective function to convergence [209, 210]. Two groups have presented algorithms including local spatially corresponding information to help the DIR algorithm converge in a more spatially accurate manner [101, 211]. However, heavy CBCT noise contamination can still present a challenge, even with a local intensity correction step.

Kim et al incorporated manually delineated organ contours and distinct points into the objective function of the B-spline algorithm, and imposed a rigidity penalty for bony regions [212, 213]. Additionally, an adaptation of the Demons algorithm has been implemented using a contour rigidity constraint to guide the objective function toward convergence [214]. A previous study has been conducted showing the utility of mapped control volumes in aiding the BSpine deformable calculation [215]. Using manually delineated points or contours can be strenuous on clinical resources if large data sets need to be analyzed.

This paper reports an automated landmark generation algorithm incorporated into the work flow of a local intensity corrected CT-CBCT DIR algorithm. The proposed

landmark-guided DIR (LDIR) algorithm uses gradient similarity as a metric to establish landmarks to help guide the Demons objective function towards convergence.

5.2 Methods and Materials

5.2.1. Landmark Generation

An overview of the workflow is illustrated in Figure 1. Simulation CT images were used with a pixel size ranging from 1 to 1.1719 mm and a slice thickness of 3 mm. The CBCTs were acquired in the first treatment week (Fraction #1 to #5) in full fan mode using a Truebeam onboard CBCT (Varian Medical System, Palo Alto, CA). The CBCT images had a pixel size of 0.9 mm and a slice thickness of 2 mm. The LDIR algorithm adopted a parallelized Demons algorithm implemented on graphics processing units (GPU) as the original framework [216].

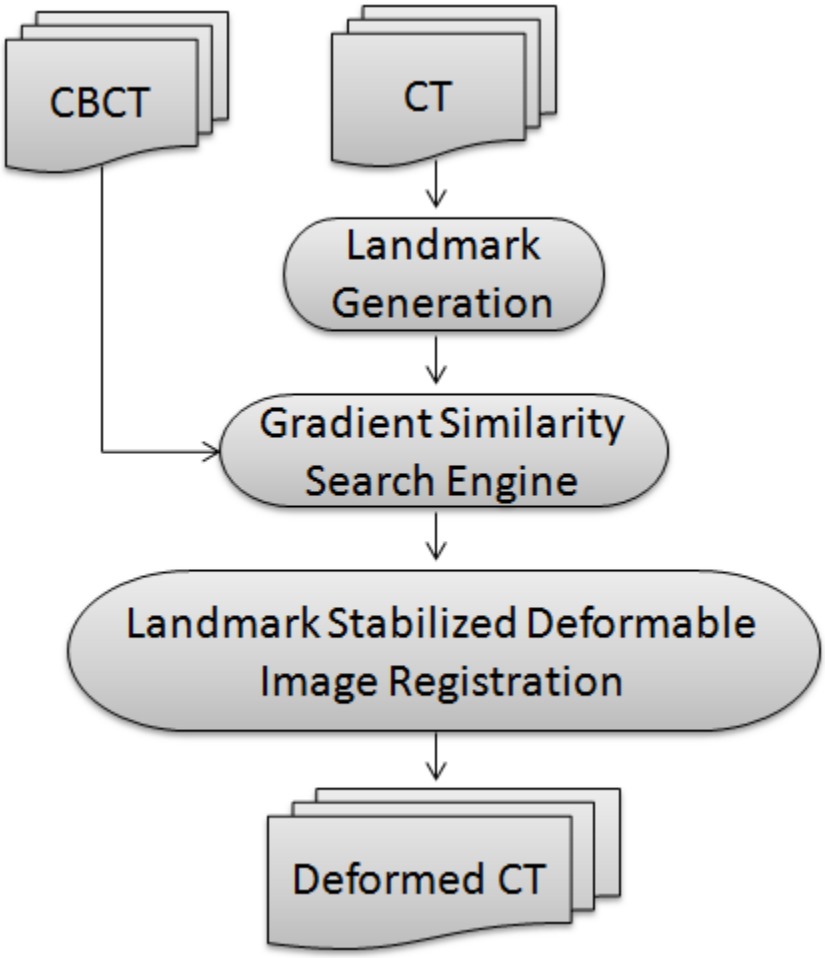

Figure 5.1. Workflow of the LDIR algorithm.

The landmark generation scheme first segments the CT into body surface, boney structures, and internal airways as shown in Figure 5.2(C). The landmarks are generated on the boundaries of each segment, as these regions all have strong gradient information as shown in Figure 2(D).

A local small volume (LSV) with an initial size of 6 mm x 6 mm x 3 mm is centered on each landmark of the static image (LSV_{static}) as shown in Figure 5.2(E). The LSV is registered to a corresponding volume on the moving image (LSV_{moving}) using a

gradient similarity search engine. Each LSV_{moving} is shifted by (i, j, k) until Q is minimized for each landmark n, where

$$Q(i,j,k)^n = \left\| (\nabla LSV_{static} - \nabla LSV_{moving}^{i,j,k})^2 (LSV_{static} - LSV_{moving}^{i,j,k})^2 \right\|$$

$$i,j,k = \arg\min Q(i,j,k)^n \quad (1)$$

Once a registration offset is determined for a landmark the LSV size is increased to a coarser multi-scale level. If two consecutive multi-scale levels (ρ) produce the same offset for a given landmark, the landmark is determined to be stable. LSV multi-scale level sizes are, $(AP, LR, SI)_\rho = [2(2+\rho),\ 2(2+\rho),\ 3(1+\ floor(\rho/2))]$ mm. A landmark is considered stable if Q_ρ^η and $Q_{\rho+1}^\eta$ are equal as shown in figure 5.2(F).

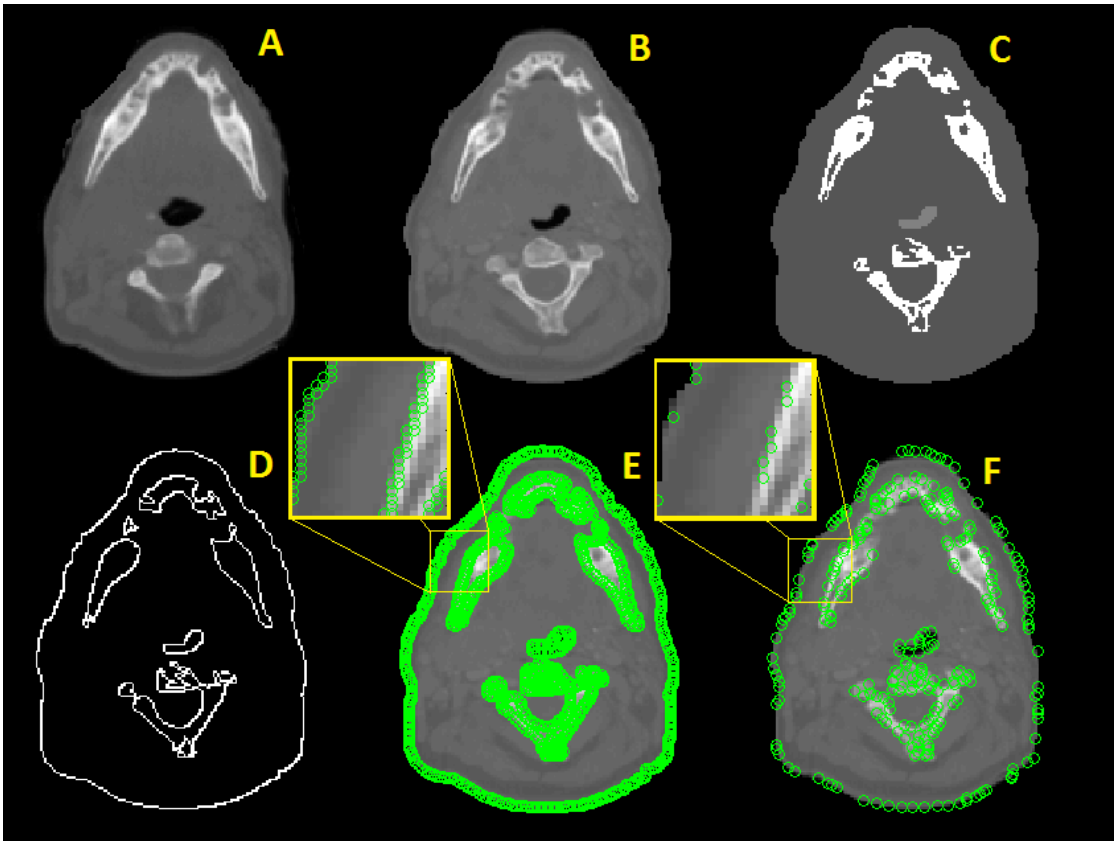

Figure 5.2. (A) Moving image (CBCT). (B) Static Image (CT). (C) Segmentation. (D) High gradient boundaries. (E) Initial set of landmarks with corresponding zoomed region. (F) Subset of stable landmarks with corresponding zoomed region.

5.2.2. Landmark-guided Demons Algorithm

Each landmark offset generated from the gradient similarity search engine represents a known deformation point. In order to obtain a complete deformation map of the entire 3D image, the sparse subset of deformation points are tri-linearly sparse data interpolated to fill in the missing deformation data around the landmarks [217-221]. Once a complete deformation map is populated, an initial sparse data interpolated deformation step is implemented on the CT images. The gradient similarity search engine is applied iteratively until $C^{i} - C^{i+4}$ is smaller than δ, which is a pre-defined

threshold. C^i is the summation of every voxel (v) for the objective function Q as defined in Eq. (1), for the i-th iteration, $C^i = \sum_v Q^v$.

A local intensity transformation is applied after each iteration. An intensity multiplication constant u is determined for each voxel n, such that the difference of the two regions are minimized.

$$D(u)^n = \left\| (LSV_{moving} \circ u) - LSV_{static}{}^2 \right\|$$

$$u = \arg\min D(u) \tag{2}$$

The deformed landmarks are used as control points in the Demons algorithm. The Demons incremental moving vector (r) at every voxel is then calculated by an adaptation of the double force method [222, 223],

$$r^{n+1} = \frac{(I_m^n - I_s)\nabla I_s}{(I_m^n - I_s)^2 + \left|\nabla I_s\right|^2} + \frac{(I_m^n - I_s)\nabla I_m^n}{(I_m^n - I_s)^2 + \left|\nabla I_m^n\right|^2} + \varepsilon(\Delta L^n)^2 \tag{3}$$

where n represents the iterative number, r^n is the iteratively updated moving vector, I_s represents the CBCT or static image, I_m represents the initially deformed intensity corrected CT or moving image, and I_m^n is the iteratively updated moving image, ΔL^n represents the iteratively updated landmark displacement magnitude between the moving image static image and ε represents an elasticity constant. The value of ε in proportional to the degree of resistance to the Demons moving vector. Displacement of the landmarks penalizes the objective function l, where $l^n = \sum_{\#voxels} | r^{n+1} | \Big/ \sum_{\#voxels} | r^n |$.

Initializing an intensity correction step helps stabilizes the $(I_m^n - I_s)$ term in the incremental moving vector r^{n+1} for CBCT-CT DIR. The whole process is repeated for two multi-scale levels. The resolution steps for this process are 4 mm x 4 mm x 6 mm, then 2 mm x 2 mm x 3 mm in the AP, LR, and SI directions respectively.

The various steps of the LDIR algorithm are implemented as follows:

Algorithm 5.1:

A. initiate multiscale loop (coarsest to Finest)

1. I_s segmentation

B. Initiate Landmark based sparse interpolation loop

C. Initiate landmark multiscale stability loop

2. LSV gradient similarity search from equation (1)

end loop

3. Compute sparse interpolant [220, 221]

$$DVF_{complete} = Scatter\ \ Grid\ \ Interpolation\ \left\| DVF_{sparse} \right\|$$

4. Warp I_m using composite DVFs [86]

$$DVF_{composite}^{i+1} = DVF_{morphed}^{i+1} + DVF_{composite}^{i}$$

5. Initiate intensity correction from equation (2)

6. Assess stopping criterion $C^i - C^{i+4} < \delta$

end loop

7. Landmark Guided Demons equation (3)

end loop

In Algorithms 5.1, the I_s segmentation represents the tissue segmentation of the static image, The DVF_{sparse} is defined as the sparse deformation vector field generated by the gradient similarity search. The $DVF_{composite}$ represents the composite DVFs updated during each iteration of the initial sparse interpolation loop. The $DVF_{morphed}$ is the latest iterative DVF.

5.2.3. Evaluations

The DVF accuracy of LDIR is accessed using a synthetic case. The synthetic data set was generated by applying a known smooth DVF to planning CT image set of a head and neck cancer patient. The deformed image was then contaminated with CBCT noise. CBCT noise was simulated by adding poison noise to the detector, and adding Gaussian noise to the background, then performing a logarithmic transform [224, 225]. The intensity distribution of the static image was then transformed using a piecewise multiplicative approach, based on previously reported electron density transformation values [191, 193-195]. The CT was deformed from the nose to the clavicle using a half sine wave DVF in the anterior-posterior (AP) direction with a maximum displacement of 22 mm. A deformation in the AP direction was chosen to simulate neck roll, and the superior-interior (SI) direction was not used due to large slice thickness, i.e. lower spatial resolution.

To evaluate the accuracy on the patient cases three different similarity metrics where used, root mean square error of the 3D Canny edge ($RMSE_{CE}$), normalized mutual information (NMI), and feature similarity index metric (FSIM). $RMSE_{CE}$ between the Canny edges C_1 and the Canny edges C_2 in corresponding images, is defined as $\mathrm{RMSE}_{\mathrm{CE}} = \sqrt{\sum_{i}^{N}[C_2{}^{i} - C_1{}^{i}]^2 \Big/ \sum_{i}^{N}[C_2{}^{i}]^2}$. Canny edges represent high gradient boundaries within an image. In CT images these edges correspond to tissue boundaries [70, 101]. NMI is a measurement of the mutual information $\mathrm{MI}^{\bar{T}}_{I_1,I_2}$ and the corresponding intensity transform $\bar{T}$ between the histograms H_1 and H_2 in the joint histogram $\mathrm{H}^{\bar{T}}_{I_1,I_2}$, where

$MI^{\vec{T}}_{I_1,I_2} = \int\int H^{\vec{T}}_{I_1,I_2} \log H^{\vec{T}}_{I_1,I_2} \Big/ H^{\vec{T}}_{I_1} H_{I_2}\, dI_1 dI_2$ [101, 211]. FSIM is an open source image similarity metric that emulates the human visual system by evaluating phase and gradient information between the two images [101, 138]. FSIM and NMI were normalized from 0 to 1, where 1 represents maximum information congruence.

5.2.4. Auto Contour Propagation

The structure set is generated from the structure DICOM file exported from Eclipse Treatment Planning System (TPS) (Varian Medical Systems, Palo Alto, CA). Each structure is assigned a value of 1 in or on the contour and given a value of zero elsewhere. The DVF is then used to deform each solid structure. All values above 0.5 are reassigned to 1, and a value of zero is given to voxels less than or equal to 0.5. Each slice of all deformed contours are converted into point sets, written into DICOM structure set format, and imported into Eclipse TPS for physician qualitative evaluation. The relative intensity distributions between the various registration algorithms are compared for individual binary volumetric critical structures. The confined NMI of the deformed contours on the CBCT are compared with the original contours on the planning CT.

5.2.5 Computational Efficiency

The authors avoid using monolithic kernels whenever possible, instead flexible kernels are utilized in the form of grid-stride loops. This helps maximize memory coalescence during processes such as tissue segmentation. Since the segments from the various tissue boundaries have a different number of points flexible kernels are used to

avoid wasting GPU threads. In addition, fast math and single precision computations are used to speed up computations on the GPU with minimal accuracy degradation [226].

The authors take advantage of NVIDIA's open source libraries to help accelerate the workflow, such as cuSPARSE, used to populate the 3D deformation space [227].

5.3. Results

5.3.1. LDIR Performance on the Synthetic Case

Demons, intensity corrected Demons (IT Demons), and LDIR were tested using the synthetic case using five different scenarios, no noise and no intensity transform (Scenario 1), noises of ± 25 HU with an intensity transform (Scenario 2), noises of ± 200 HU with an intensity transform (Scenario 3), noises of ± 800 HU with an intensity transform (Scenario 4), noises of ± 2400 HU with an intensity transform (Scenario 5). Figure 5.3 shows all five scenarios and the ground truth.

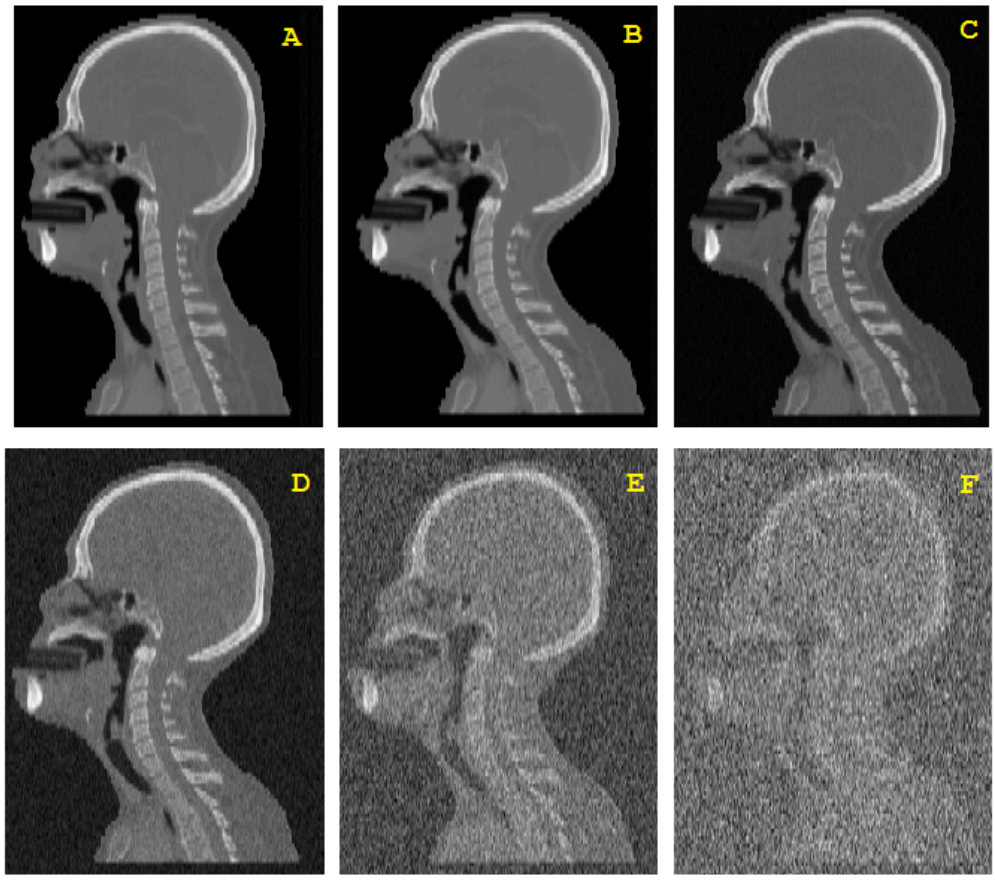

Figure 5.3. (A) Ground truth CT, (B) Scenario 1, no noise and no intensity transform. (C) Scenario 2, noises of ± 25 HU with an intensity transformation. (D) Scenario 3, noises of ± 800 HU with an intensity transform. (E) Scenario 4, noises of ± 800 HU with an intensity transform. (F) Scenario 5, noises of ± 2400 HU with an intensity transform.

Figure 5.4 shows the ground truth DVF comparison using Demons and LDIR for scenario 1 and 3. LDIR provides better results.

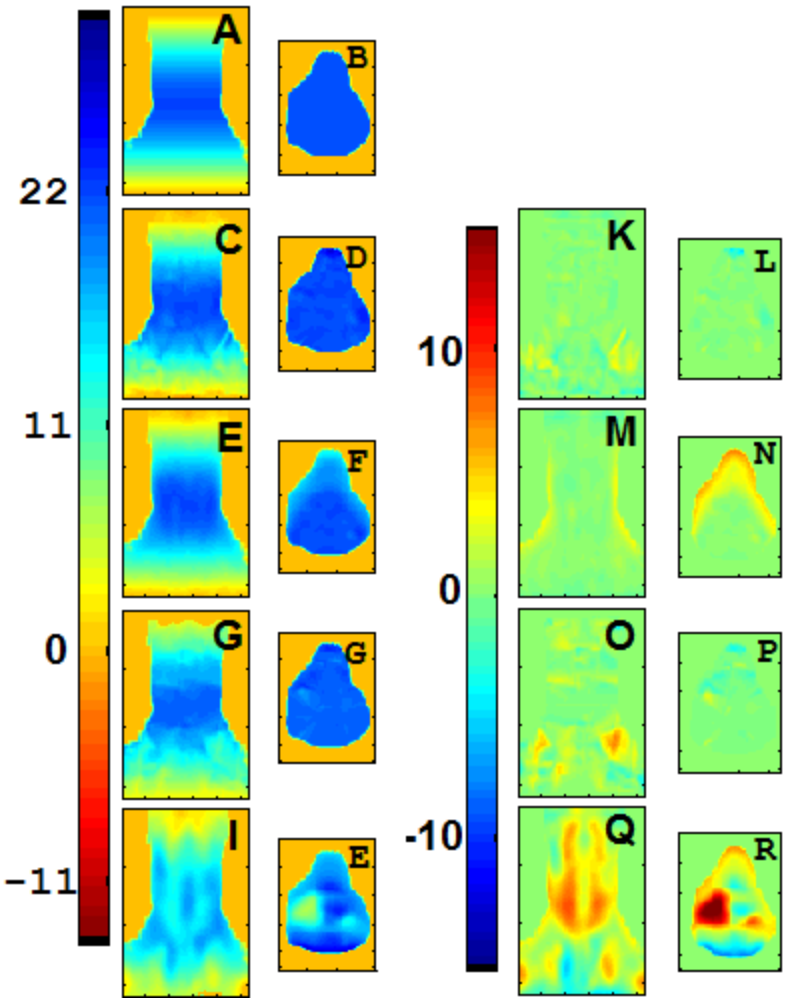

Figure 5.4. (A) and (B) ground truth DVF (mm), for a mid-sagittal and mid axial slice respectively. (C) and (D) LDIR for scenario 1. (E) and (F) Demons for scenario 1. (G) and (H) LDIR for scenario 4. (I) and (J) Demons for scenario 4. (K) and (L) LDIR error (mm) for scenario 1. (M) and (N) Demons error for scenario 1. (O) and (P) LDIR error for scenario 4. (Q) and (R) Demons error for scenario 4.

All ground truth scenarios were evaluated using the 90 percentile error margin for the Demons algorithm, IT Demons, and LDIR. Table 5.1 shows the DVF accuracy for all five scenarios using various DIR algorithms.

Table 5.1. The DVF 90 percentile error for LDIR, IT Demons, and Demons for all five scenarios.

	Scenario 1	Scenario 2	Scenario 3	Scenario 4	Scenario 5
LDIR 90% error (mm)	1.44	1.68	1.92	2.67	3.87
IT Demons 90% error (mm)	1.94	2.41	3.07	4.76	6.26
Demons 90% error (mm)	1.32	4.23	5.89	7.64	7.86

5.3.2. LDIR Performance on Five Patients

The performance of LDIR is shown using intensity difference information on five head and neck cancer patients. Figure 5.5 shows the intensity difference between the various DIR algorithms.

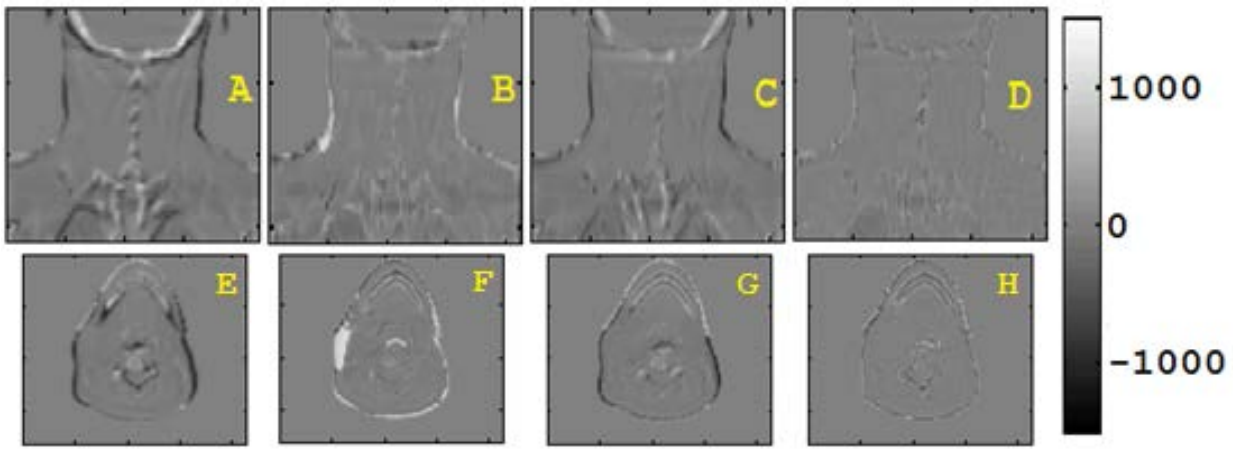

Figure 5.5. Mid sagittal slice (top row) and mid axial slice (bottom row) of the CBCT subtracted from the, CT (A, E), Demons deformed CT (B, F), intensity corrected Demons deformed CT (C, G), LDIR deformed CT (D, H).

The Demons deformed CT and CBCT shows a big intensity discrepancy. IT Demons shows improvement over rigid registration and Demons registration. LDIR shows the highest intensity congruence out of all the algorithms.

Figure 5.6 shows a checkerboard comparison of the various stages of the LDIR algorithm.

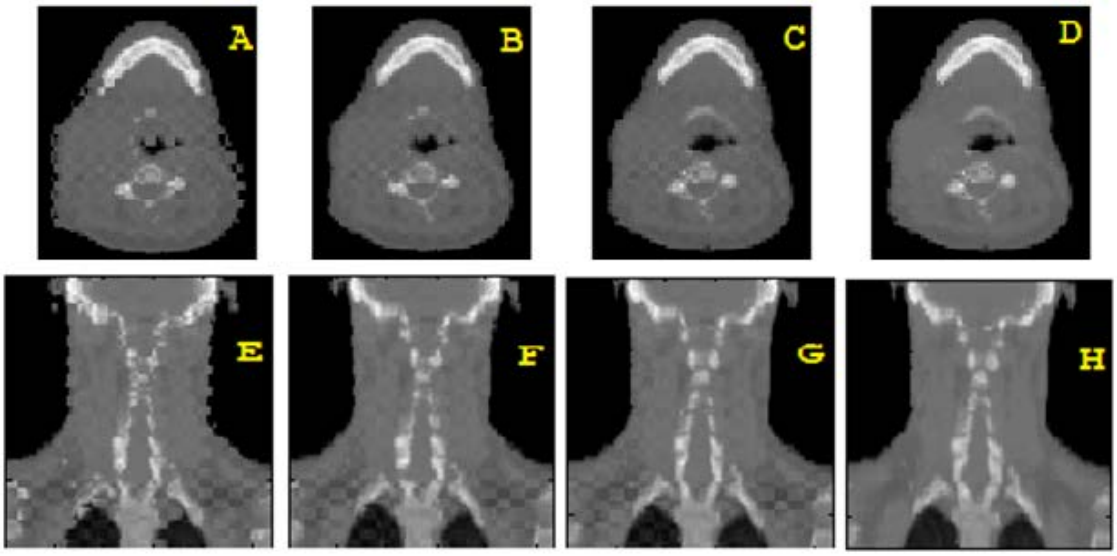

Figure 5.6. Checkerboard mid axial (top row) and mid sagittal (bottom row) slice of the CBCT and, rigid registration (A, E), IT Demons (B, F), LDIR (C, G), and intensity corrected CBCT with LDIR (D, H).

As seen through visual inspection of the checkerboard comparison the LDIR algorithm is more spatially accurate than IT Demons and rigid registration. Table 5.2 lists the similarity metric results for the various DIR algorithms.

Table 5.2. NMI, $RMSE_{CE}$ and FSIM results between the rigid registration, Demons, IT Demons, initial LDIR, and LDIR compared with the CBCT for all five patients and their corresponding mean values.

		p1	p2	p3	p4	p5	p6	mean
NMI	Rigid Registration	0.55	0.52	0.56	0.61	0.59	0.58	0.57
	Demons	0.57	0.61	0.59	0.62	0.60	0.60	0.60
	IT Demons	0.67	0.67	0.69	0.71	0.68	0.65	0.68
	Initial LDIR	0.65	0.63	0.64	0.65	0.63	0.68	0.65
	LDIR	0.70	0.68	0.71	0.72	0.69	0.70	0.70
$RMSE_{CE}$	Rigid Registration	0.28	0.29	0.24	0.19	0.21	0.22	0.24
	Demons	0.25	0.31	0.27	0.19	0.25	0.23	0.25
	IT Demons	0.22	0.26	0.19	0.15	0.18	0.17	0.20
	Initial LDIR	0.19	0.26	0.18	0.13	0.19	0.17	0.19
	LDIR	0.18	0.22	0.15	0.11	0.13	0.12	0.15
FSIM	Rigid Registration	0.88	0.89	0.93	0.93	0.85	0.86	0.89
	Demons	0.86	0.88	0.94	0.93	0.88	0.87	0.89
	IT Demons	0.90	0.91	0.96	0.95	0.90	0.93	0.93
	Initial LDIR	0.92	0.91	0.98	0.97	0.89	0.96	0.94
	LDIR	0.93	0.92	0.99	0.98	0.91	0.98	0.95

Amongst all similarity metric evaluation techniques LDIR consistently out performs all other algorithms. IT Demons and initial LDIR registration without demons produce similar results for $RMSE_{CE}$ and FSIM, but IT Demons performed better for NMI.

Figure 5.7 shows the step sizes, ρ, of the LSVs $(AP, LR, SI)_{\rho}$ for the first 1000 points of each iteration in the landmark generation scheme.

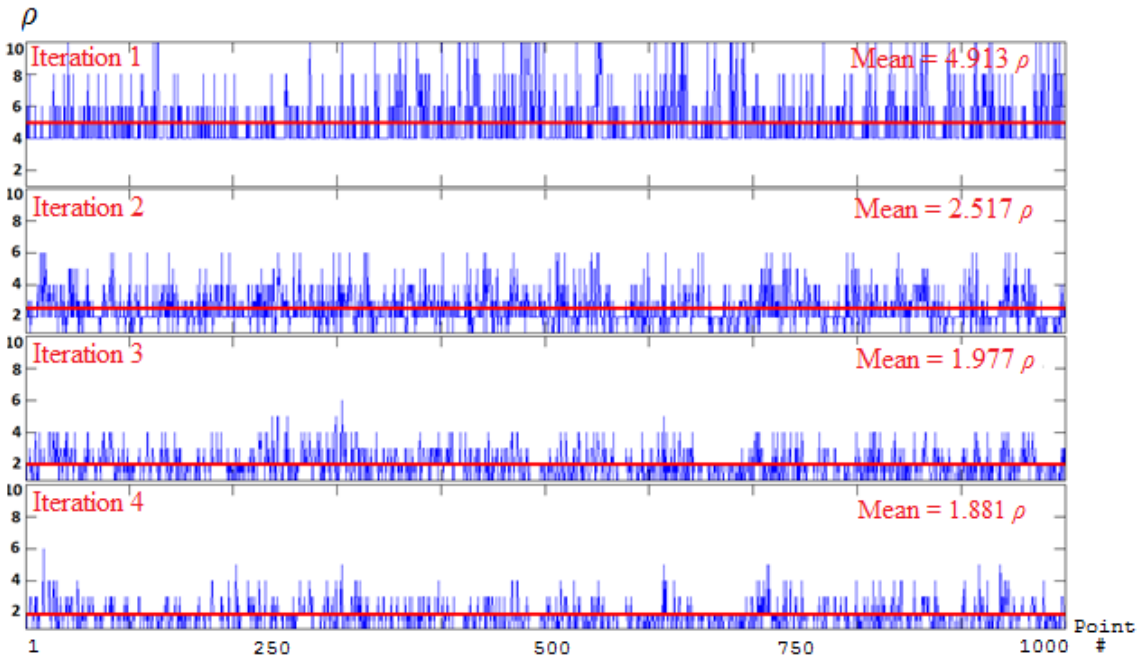

Figure 5.7. Iterative LSV multi-scale level ρ, at each landmark for the initial LDIR deformation. The 1st iteration has a mean of 4.913ρ, the 2nd iteration has a mean of 2.517ρ, the 3rd iteration had a mean of 1.977ρ, and the 4th iteration had a mean of 1.881ρ.

The LSV sizes get smaller until the stopping criterion is satisfied. The resolution of the control points depends on the stability of the LSV region. Allowing the resolution to vary depending on the stability of the LSV region helps determine the optimal resolution size for a given landmark.

The value of the elasticity constant ε affects the behavior of the LDIR algorithm by resisting the Demons moving vector force. Figure 5.8 shows LDIR using different values of ε.

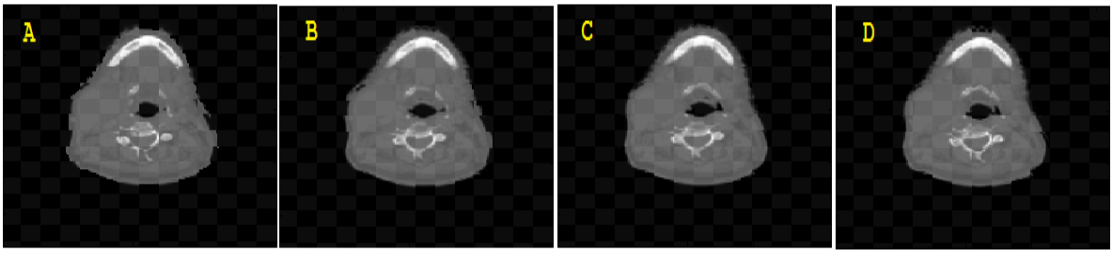

Figure 5.8. Checkerboard image of mid axial slice of the CBCT and LDIR with different ε values, 0 (A), 10 (B), 50 (C), 1000 (D).

An ε value of zero yields similar results as intensity corrected Demons, and a very large ε value produces results similar to the initial LDIR deformation.

Figure 5.9 demonstrates the contour mapping accuracy of the LDIR algorithm. Several contours have been mapped to the CBCT and the original CT for comparison. LDIR maps contours to the CBCT that match up well with their corresponding anatomy when compared against the rigidly registered contours.

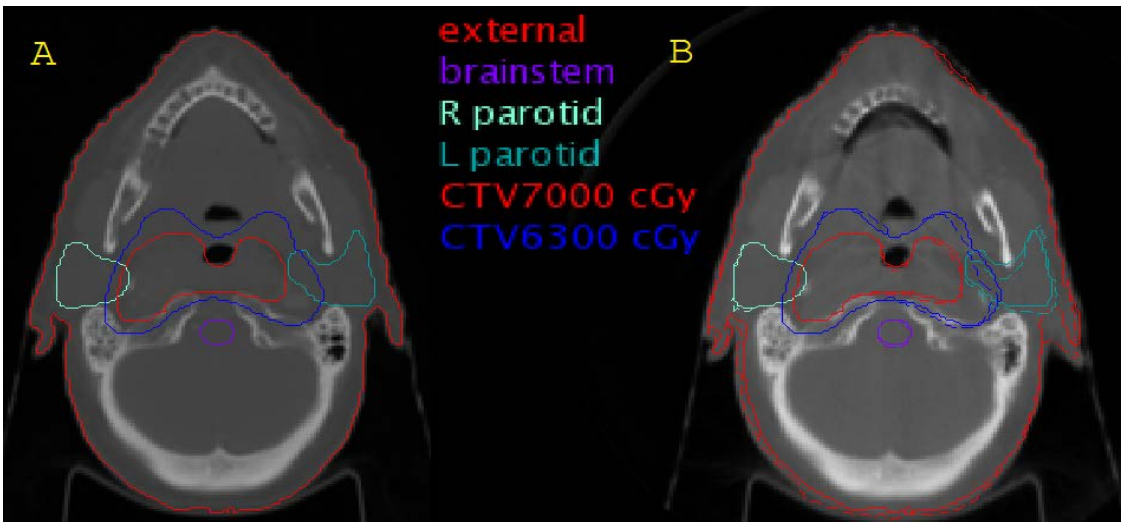

Figure 5.9. (A) Represents the mid axial slice of the simulation CT with superimposed original contours represented by solid lines. (B) Mid-axial slice of the CBCT with superimposed deformed contours represented by dashed lines and original contours represented by solid lines.

Table 5.3 shows NMI confined to critical structures on the CBCT. The confined NMI is highest for the LDIR algorithm compared to the IT Demons and rigid registration, which indicates that the relative intensity distribution between the LDIR deformed contours on the CBCT matches best with the relative intensity distribution of the original contours on the original image.

Table 5.3. NMI is shown for individual structures. NMI of the ROI for the Brainstem, Parotids (mean of left and right sides), Optic Nerves (mean of left and right sides), optic chiasm, and the temporal lobes (mean of left and right sides) are shown for rigid registration, IT Demons, and LDIR.

	P1			P2			P3		
	Rigid Registration	IT Demons	LDIR	Rigid Registration	IT Demons	LDIR	Rigid Registration	IT Demons	LDIR
Brainstem	0.41	0.55	0.59	0.38	0.43	0.53	0.56	0.59	0.61
Parotids	0.33	0.46	0.48	0.25	0.37	0.41	0.28	0.29	0.31
Optic Nerves	0.21	0.51	0.59	0.18	0.32	0.36	0.43	0.48	0.54
Optic Chiasm	0.19	0.18	0.22	0.22	0.25	0.34	0.29	0.29	0.31
Temporal Lobes	0.66	0.66	0.68	0.58	0.59	0.62	0.61	0.62	0.64
	P4			P5			P6		
	Rigid Registration	IT Demons	LDIR	Rigid Registration	IT Demons	LDIR	Rigid Registration	IT Demons	LDIR
Brainstem	0.27	0.41	0.42	0.42	0.47	0.49	0.39	0.42	0.51
Parotids	0.40	0.51	0.57	0.39	0.46	0.48	0.26	0.38	0.40
Optic Nerves	0.38	0.42	0.51	0.26	0.37	0.38	0.17	0.31	0.37
Optic Chiasm	0.26	0.28	0.29	0.18	0.25	0.27	0.25	0.26	0.28
Temporal Lobes	0.56	0.57	0.57	0.67	0.66	0.68	0.61	0.63	0.64

5.4. Discussion and Conclusion

The ground truth accuracy of Demons, IT Demons and LDIR were all evaluated at the 90 percentile error margin. For the no-noise no-intensity-transformation scenario (scenario 1) all algorithms were highly accurate and were within 2 mm error. Demons performed slightly better than LDIR for the ideal case. When an intensity transform was introduced LDIR and IT Demons remained accurate, 1.68 mm and 2.41 mm respectively, while Demons produced errors exceeding 4.2 mm. As noise was increased the accuracy of IT demons was rapidly degraded while the LDIR accuracy remained high up to scenario 4 (2.67mm). None of the algorithms performed well on Scenario 5 but LDIR still performed better than IT Demons and Demons by at least 2.39 mm.

Non-parametric based DIR algorithms such as Demons will generally perform well under intensity information based metrics such as mutual information and cross correlation. The initial LDIR performs well under tissue boundary similarity metrics such as FSIM and Canny Edge. The combination of initial LDIR with IT Demons gives the best results for all similarity metric algorithms.

The image quality of the CBCT varies regionally, so determining the optimal resolution size should also depend on how well the corresponding regions match. Intensity matching matrices such as cross correlation can be accurate in the presence of noise if there is a large enough sample size. Cross correlation works very well for whole data sets, but begins to break down when a subset of an image is used. Similarly, regional gradient similarity can be accurate in the presence of noise, but begins the break

down when the region of interest gets too small. By allowing the LSV sizes to vary depending on the stability of the region a resolution level can be chosen that is big enough to ensure accuracy but small enough to maintain high resolution. For all patients the mean resolution of the LSV was below 8 mm x 8 mm x 6 mm by the 3rd iteration and had a maximum resolution of 16 mm x 16 mm x 12 mm by the 5th iteration. The initial LDIR step converged between iteration 2 and 5 for all five patients.

The improvement of LDIR over conventional intensity corrected Demons will not be as great in regions that reside far away from the nearest control points. The algorithm will behave more like intensity corrected Demons with good initial starting conditions for regions of the body that do not have strong gradient information.

The LDIR contour mapping quality was verified on every slice by an attending physician for the right and left parotids, body, spinal cord, brainstem, and all CTVs for all patients. The confined NMI of the critical structures was used to quantitatively access the accuracy of the deformed contours. NMI was used since other similarity metrics such as FSIM, RMSE, or cross correlation include spatial information and will give a bias towards the rigidly registered contours since they have the same shape as the original structure set.

LDIR maintains computational efficiency by using only a sparse subset of control points, and by utilizing GPUs. Amongst the five patient cohort, the longest computation time for LDIR was less than 215s for an image set of 256 by 256 by 132. A NVIDIA G-force 580 GTX card was used with a 2.53 GHz Intel Xeon processor with 12 GB of memory. Since LDIR is computationally efficient, it can be clinically incorporated with

minimal additional strain on clinical resources, and is a viable complement to the ultra-fast imaging and adaptive replanning GPU computing paradigm shift [100, 228-240].

Both the synthetic case and patient data demonstrate that LDIR achieves high deformable image registration accuracy between multimodality images in the presence of noise contamination, while simultaneously preserving high computational efficiency. LDIR presents a possible solution to overcome the unique imaging difficulties of CBCT to CT DIR. Additionally, a dosimetric longitudinal study is underway, which will shed light on the dosimetric implications of patient anatomical deformation throughout the course of radiotherapy. Furthermore, there is a potential to use LDIR for adaptive replanning on low dose CBCTs since LDIR performs well under heavy noise conditions.

5.5 Acknowledgements

This work was supported in part by **Cancer Prevention Research Institute of Texas** (CPRIT) grants RP110329 and RP110562-P2.

CHAPTER 6

CONCLUSION

6.1 General Summary

This dissertation summarizes my work on computer vision algorithm development for biomedical applications. Although this work has been applied to a wide scope of scenarios, all with their own unique blend of challenges, one central theme remained consistent. In all chapters computer vision was used to make decisions that were then used to interpret, rank, deform, or segment biomedical images for the purpose of facilitating physicians in a clinical setting, or investigators during research and development.

Although many of the approaches used in this work have been in existence for a long time, their applications to these various biomedical problems are. For instance, sparse math has been main stream in computer science application since the 70s [241, 242]. Similarly, automated biomedical image registration has been mainstream since the 90s [243, 244]. However, this work describes the first successful development of a deformable image registration algorithm that relies entirely on sparse matrix manipulation and thus overcomes many of the conventional challenges dealing with CBCT to CT registration [29, 30]. Additionally, feature extraction methods have been widely implemented since the 90s and the canny edge algorithm was introduced in the 80s [63, 69, 245]. However, this work was the first to develop a technique that combines canny edge detection, feature extraction, and sparse matrix DIR to overcome the

challenges of white light based DIR problems. This novel algorithm extends the application of portable *in vivo* imaging and allows for quantitative, non-invasive, non-ionizing, automated temporal tracking using a small animal model. Following a similar trend, the combination of canny edge extraction, sparse matrix DIR, and amoeba optimization routines was the first of its class to present a successful algorithm to track posterior retinal drug accumulation using serial sectioning fluorescent images.

6.2 Specific Summary

The superiority of landmark-guided DIR over other DIR was demonstrated in Kearney et al., and the accuracy was shown to be preserved in the presence of noise contamination and tissue specific intensity transformations [29, 30]. This work will help clinicians retrospectively accumulate dose to assess the treatment quality and help them make decision about future treatment fractions. Additionally, since landmark-guided DIR was implemented on GPUs and is computationally efficient, it could be implemented without minimal strain on clinical resources.

The feasibility of using a serial sectioning drug imaging protocol for the posterior vitreous was demonstrated for the automated retinal deformation and drug dispersion tracking algorithm. This novel algorithm corrects for segmentation distortion and automatically segments the retina. This entire process is currently available in an end-user software package called EyeMesh, allowing investigators to accurately track and quantitatively assess posterior retinal targeting drugs tagged with fluorescent tracers.

A Canny edge white light based DIR algorithm was developed and evaluated. This study has shown that Canny DIR is more spatially accurate than other existing methods. This was demonstrated using intensity and fluorescence based evaluation matrices. Canny DIR is resistant to illumination changes, and can accurately track anatomical deformation using an *in vivo* small animal model.

A multiple site background removal and temporal tracking algorithm was developed, evaluated, and implemented using an *in vivo* mouse model. The multiple site background removal strategy was shown to consistently produce more accurate concentration predictions than other models. This algorithm will help enable more accurate peak delineation of implantation sites using a multiple site small animal *in vivo* model. The peak tracking algorithm was shown to be more accurate than the deformed or rigid registration algorithms. The peak tracking algorithm could help reduce intra- and inter-user induced errors and variability, and help reduce experimental workload. Additionally, these algorithms help further the experimental application of the small animal portable imager and enable accurate multiple implantation temporal tracking.

6.3 Future Directions

Although the results from all these studies are exciting, further investigation, development and validation are required to push these imaging techniques to next level, such as the clinic implementation or further research advancement. Future efforts should be devoted to several areas, as are summarized below.

First, for landmark-guided DIR, much work has to be done before such an algorithm can be implanted into the clinic, such as FDA approval. FDA approval would require a comprehensive examination of the limitation of this algorithm as well as extensive clinical validation. For now, this algorithm is limited to research and retrospective treatment evaluation. Future studies should be aimed at the evaluating this algorithm for more body sites, as the patient cohort was limited to head and neck patients undergoing VMAT. Future studies should also incorporate an internal airway compensation strategy to better address the changing configuration of the epiglottis, esophagus and oral cavity. Additionally, a routine that is free of the conventional Demons algorithm should be developed. This could potentially enhance the performance of the algorithm in the most inferior low contrast regions, where noise contamination is the highest.

Second, for the automated retinal segmentation and serial sectioning algorithms, further assessment of the limitations of the algorithm should be conducted. This would help investigators know when the distortion correction algorithm is most reliable. Also evaluations of the accuracy, as it relates to slice thickness, should be carried out, so that the axial resolution can be maximized without degrading the correction accuracy. Additionally, a more comprehensive study should be conducted on the effects of retinal detachment on the accuracy of the retinal segmentation. A study that compares retinal segmentation accuracy for slices with and without retinal detachment will help investigators understand the limitations of this algorithm and avoid potential pitfalls.

Third, for the Canny edge white light based DIR algorithm, a more comprehensive assessment of the algorithm limitations should be conducted. The algorithm should be tested under more extreme lighting and deformation differences. This will give the investigators a better guideline of suitable conditions, so they can rely on this algorithm with more confidence and be aware of any possible pitfalls to avoid.

Fourth, future directions for the multiple site background removal and temporal tracking algorithm should be directed at a more comprehensive evaluation of effect of signal intensity on accuracy. For the multiple site background removal strategy, the limitations in regards to the implantation site proximity and relative strength should be examined. This would help investigators determine the optimal distance for implantation site separation and relative concentrations for an *in vivo* mouse model. For the temporal tracking algorithm, since this algorithm was only tested using an EPO release model, more in vivo applications should be carried out to test the experimental application limitation of this algorithm.

REFERENCES

1. Sonka, M., V. Hlavac, and R. Boyle, *Image processing, analysis, and machine vision*. 2014: Cengage Learning.
2. Enderle, J.D. and J.D. Bronzino, *Introduction to biomedical engineering*. 2012: Academic press.
3. Bach, P.B., et al., *Benefits and harms of CT screening for lung cancer: a systematic review.* Jama, 2012. **307**(22): p. 2418-2429.
4. McWilliams, A., et al., *Probability of cancer in pulmonary nodules detected on first screening CT.* New England Journal of Medicine, 2013. **369**(10): p. 910-919.
5. Pinto, A., et al. *Learning from errors in radiology: a comprehensive review*. in *Seminars in Ultrasound, CT and MRI*. 2012. Elsevier.
6. Tanimoto, S., *Structured computer vision: machine perception through hierarchical computation structures*. 2014: Elsevier.
7. Shapiro, L.G. *Image analysis for biomedical and healthcare applications*. in *Proceedings of the 1st ACM international workshop on Multimedia indexing and information retrieval for healthcare*. 2013. ACM.
8. Klette, R., *Concise computer vision*. 2014: Springer.
9. Bradski, G.R., *Computer vision face tracking for use in a perceptual user interface.* 1998.
10. Shapiro, L., *Computer vision and image processing*. 1992: Academic Press.
11. Szeliski, R., *Computer vision: algorithms and applications*. 2010: Springer Science & Business Media.
12. Forsyth, D.A. and J. Ponce, *A modern approach.* Computer Vision: A Modern Approach, 2003: p. 88-101.
13. Fletcher, R., *Practical methods of optimization*. 2013: John Wiley & Sons.
14. Ingber, L., et al., *Adaptive simulated annealing*, in *Stochastic global optimization and its applications with fuzzy adaptive simulated annealing*. 2012, Springer. p. 33-62.
15. Goldstein, T., E. Esser, and R. Baraniuk. *Adaptive Primal Dual Optimization for Image Processing and Learning*. in *Proc. 6th NIPS Workshop Optim. Mach. Learn*. 2013.
16. Tichauer, K.M., et al., *Computed tomography-guided time-domain diffuse fluorescence tomography in small animals for localization of cancer biomarkers.* Journal of visualized experiments: JoVE, 2012(65).
17. Dowsland, K.A. and J.M. Thompson, *Simulated annealing*, in *Handbook of Natural Computing*. 2012, Springer. p. 1623-1655.
18. Singhal, N., et al., *Implementation and optimization of image processing algorithms on embedded GPU.* IEICE TRANSACTIONS on Information and Systems, 2012. **95**(5): p. 1475-1484.
19. Davis, S.C., et al., *Dynamic dual-tracer MRI-guided fluorescence tomography to quantify receptor density in vivo.* Proceedings of the National Academy of Sciences, 2013. **110**(22): p. 9025-9030.

20. Lu, Y., et al., *In vivo imaging of orthotopic prostate cancer with far-red gene reporter fluorescence tomography and in vivo and ex vivo validation.* Journal of biomedical optics, 2013. **18**(10): p. 101305-101305.
21. Droske, M. and M. Rumpf, *A variational approach to nonrigid morphological image registration.* SIAM Journal on Applied Mathematics, 2004. **64**(2): p. 668-687.
22. Shen, J.-K., B.J. Matuszewski, and L.-K. Shark. *Deformable image registration*. in *Image Processing, 2005. ICIP 2005. IEEE International Conference on*. 2005. IEEE.
23. Gu, Y., et al., *Automated delineation of lung tumors from CT images using a single click ensemble segmentation approach.* Pattern recognition, 2013. **46**(3): p. 692-702.
24. Agarwal, R., A. Shankhadhar, and R.K. Sagar. *Detection of Lung Cancer Using Content Based Medical Image Retrieval*. in *Advanced Computing & Communication Technologies (ACCT), 2015 Fifth International Conference on*. 2015. IEEE.
25. Azeredo, T., I. Matias, and W. Oliveira. *Development of a Virtual Input Device Using Stereoscopic Computer Vision to Control a Vehicle in a Racing Game*. in *ICCGI 2012, The Seventh International Multi-Conference on Computing in the Global Information Technology*. 2012.
26. Diner, D.B. and D.H. Fender, *Human engineering in stereoscopic viewing devices*. 2013: Springer Publishing Company, Incorporated.
27. Fan, W., et al. *3D lighting-based image forgery detection using shape-from-shading*. in *Signal Processing Conference (EUSIPCO), 2012 Proceedings of the 20th European*. 2012. IEEE.
28. Patil, V.H., *Data Structures using C++*. 2012: Oxford University Press, Inc.
29. Kearney, V., et al., *Automated landmark-guided deformable image registration.* Physics in medicine and biology, 2015. **60**(1): p. 101.
30. Kearney, V., et al., *WE-D-9A-02: Automated Landmark-Guided CT to Cone-Beam CT Deformable Image Registration.* Medical Physics, 2014. **41**(6): p. 500-500.
31. Huang, C.W., et al. *Hollow Gold Nanoparticals as Biocompatible Radiosensitizer: An In Vitro Proof of Concept Study*. in *Journal of Nano Research*. 2015. Trans Tech Publ.
32. Kearney, V., et al., *TH-C-137-06: An Inter-Fractional Morphing Aperture Based Reoptimization Tool for Adaptive Radiotherapy.* Medical Physics, 2013. **40**(6): p. 533-533.
33. Kearney, V., et al., *SU-E-T-463: A Dosimetric Evaluation of CBCT Guided Intra-Fractional Adaptive Radiotherapy for VMAT.* Medical Physics, 2013. **40**(6): p. 312-312.
34. Kearney, V., et al., *SU-C-BRA-02: Evaluation of 2D DIR from CBCT to 4DCT Projections as a Tool for IGART.* Medical Physics, 2012. **39**(6): p. 3602-3603.
35. Kearney, V., et al., *SU-E-J-185: 4DCT Geometrical Eigenmode Model for Inter-Fraction Evaluation of Tumor Regression and Breathing Pattern Changes.* Medical Physics, 2012. **39**(6): p. 3695-3695.
36. Kearney, V.P., *Novel applications of 2D and 3D deformable registration in image-guided radiation therapy.* 2012.
37. Rozario, T., et al., *An accurate algorithm to match imperfectly matched images for lung tumor detection without markers.* Journal of Applied Clinical Medical Physics, 2015. **16**(3).
38. Hilderbrand, S.A. and R. Weissleder, *Near-infrared fluorescence: application to in vivo molecular imaging.* Current opinion in chemical biology, 2010. **14**(1): p. 71-79.

39. Rao, J., A. Dragulescu-Andrasi, and H. Yao, *Fluorescence imaging in vivo: recent advances.* Current opinion in biotechnology, 2007. **18**(1): p. 17-25.
40. Balas, C., *Review of biomedical optical imaging—a powerful, non-invasive, non-ionizing technology for improving in vivo diagnosis.* Measurement science and technology, 2009. **20**(10): p. 104020.
41. Holdsworth, D.W. and M.M. Thornton, *Micro-CT in small animal and specimen imaging.* Trends in Biotechnology, 2002. **20**(8): p. S34-S39.
42. Carlson, S.K., et al., *Small animal absorbed radiation dose from serial micro-computed tomography imaging.* Molecular Imaging and Biology, 2007. **9**(2): p. 78-82.
43. Jawhara, S. and S. Mordon, *In vivo imaging of bioluminescent Escherichia coli in a cutaneous wound infection model for evaluation of an antibiotic therapy.* Antimicrobial agents and chemotherapy, 2004. **48**(9): p. 3436-3441.
44. Anderson, R.E. and N.L. Warner, *Ionizing radiation and the immune response.* Advances in immunology, 1976. **24**: p. 215-335.
45. Kroeker, K.I., et al., *Patients with IBD are exposed to high levels of ionizing radiation through CT scan diagnostic imaging: a five-year study.* Journal of clinical gastroenterology, 2011. **45**(1): p. 34-39.
46. Kobayashi, H., et al., *Micro-MRI methods to detect renal cysts in mice.* Kidney international, 2004. **65**(4): p. 1511-1516.
47. Qin, X., et al. *3D in vivo imaging of rat hearts by high frequency ultrasound and its application in myofiber orientation wrapping*. in *SPIE Medical Imaging*. 2015. International Society for Optics and Photonics.
48. Maier-Hein, L., et al., *Optical techniques for 3d surface reconstruction in computer-assisted laparoscopic surgery.* Medical image analysis, 2013. **17**(8): p. 974-996.
49. Johnson, M., et al., *Micro-PET/CT monitoring of herpes thymidine kinase suicide gene therapy in a prostate cancer xenograft: the advantage of a cell-specific transcriptional targeting approach.* Molecular imaging, 2005. **4**(4): p. 463.
50. Kung, H.F., et al., *In vivo SPECT imaging of CNS D2.* J. Nucl. Med., 1990. **31**: p. 573-579.
51. Rodriguez, S., et al. *In-vivo breast imaging using an ultra-portable hand-held near-infrared optical scanner (NIROS)*. in *Biomedical Optics*. 2014. Optical Society of America.
52. Werner, S.G., et al., *Inflammation assessment in patients with arthritis using a novel in vivo fluorescence optical imaging technology.* Annals of the rheumatic diseases, 2012. **71**(4): p. 504-510.
53. Okusanya, O.T., et al., *Small portable interchangeable imager of fluorescence for fluorescence guided surgery and research.* Technology in cancer research & treatment, 2014: p. tcrt. 2012.500400.
54. Ye, J., et al. *A portable fluorescence microscopic imaging system for cholecystectomy*. in *SPIE BiOS*. 2016. International Society for Optics and Photonics.
55. Zhu, H., et al., *Optical imaging techniques for point-of-care diagnostics.* Lab on a Chip, 2013. **13**(1): p. 51-67.
56. Joshi, A.A., et al., *DigiWarp: a method for deformable mouse atlas warping to surface topographic data.* Physics in medicine and biology, 2010. **55**(20): p. 6197.
57. Wang, H., D.B. Stout, and A.F. Chatziioannou, *Mouse atlas registration with non-tomographic imaging modalities—a pilot study based on simulation.* Molecular Imaging and Biology, 2012. **14**(4): p. 408-419.

58. Wang, H., et al., *MARS: a mouse atlas registration system based on a planar x-ray projector and an optical camera.* Physics in medicine and biology, 2012. **57**(19): p. 6063.
59. Avriel, M., *Nonlinear programming: analysis and methods*. 2003: Courier Corporation.
60. Bonnans, J.-F., et al., *Numerical optimization: theoretical and practical aspects*. 2013: Springer Science & Business Media.
61. Horst, R. and H. Tuy, *Global optimization: Deterministic approaches*. 2013: Springer Science & Business Media.
62. Folkerts, M.M., *Digitally Reconstructed Radiographs.* Graphics Processing Unit-Based High Performance Computing in Radiation Therapy, 2015: p. 15.
63. Yuille, A.L., P.W. Hallinan, and D.S. Cohen, *Feature extraction from faces using deformable templates.* International journal of computer vision, 1992. **8**(2): p. 99-111.
64. Lowe, D.G., *Distinctive image features from scale-invariant keypoints.* International journal of computer vision, 2004. **60**(2): p. 91-110.
65. Xiong, X. and F. Torre. *Supervised descent method and its applications to face alignment*. in *Proceedings of the IEEE conference on computer vision and pattern recognition*. 2013.
66. de la Torre, F., et al. *Intraface*. in *Automatic Face and Gesture Recognition (FG), 2015 11th IEEE International Conference and Workshops on*. 2015. IEEE.
67. Chu, W.-S., F. Torre, and J. Cohn. *Selective transfer machine for personalized facial action unit detection*. in *Proceedings of the IEEE Conference on Computer Vision and Pattern Recognition*. 2013.
68. Naveen, C., *SIFT (Scale invariant Feature Transform) Algorithm*, 2013, October.
69. Canny, J., *A computational approach to edge detection.* Pattern Analysis and Machine Intelligence, IEEE Transactions on, 1986(6): p. 679-698.
70. Qian, R.J. and T.S. Huang, *Optimal edge detection in two-dimensional images.* IEEE Trans Image Process, 1996. **5**(7): p. 1215-20.
71. Worthington, P.L. *Enhanced Canny edge detection using curvature consistency*. in *Pattern Recognition, 2002. Proceedings. 16th International Conference on*. 2002. IEEE.
72. Wang, Z. and S.-x. HE, *An Adaptive Edge-detection Method Based on Canny Algorithm [J].* Journal of Image and Graphics, 2004. **8**: p. 010.
73. Luo, Y. and R. Duraiswami. *Canny edge detection on NVIDIA CUDA*. in *Computer Vision and Pattern Recognition Workshops, 2008. CVPRW'08. IEEE Computer Society Conference on*. 2008. IEEE.
74. Wang, B. and S. Fan. *An improved CANNY edge detection algorithm*. in *Computer Science and Engineering, 2009. WCSE'09. Second International Workshop on*. 2009. IEEE.
75. Chen, L. and C. Lo, *Edge-based registration for airborne imagery and lidar data.* ISPRS Remote Sensing and Spatial Information Sciences, 2012: p. 265-268.
76. Veiseh, M., et al., *Tumor paint: a chlorotoxin: Cy5. 5 bioconjugate for intraoperative visualization of cancer foci.* Cancer research, 2007. **67**(14): p. 6882-6888.
77. Samet, H. and M. Tamminen, *Efficient component labeling of images of arbitrary dimension represented by linear bintrees.* Pattern Analysis and Machine Intelligence, IEEE Transactions on, 1988. **10**(4): p. 579-586.
78. Jarvis, R.A., *On the identification of the convex hull of a finite set of points in the plane.* Information Processing Letters, 1973. **2**(1): p. 18-21.
79. Stein, A., E. Geva, and J. El-Sana, *CudaHull: Fast parallel 3D convex hull on the GPU.* Computers & Graphics, 2012. **36**(4): p. 265-271.

80. Srikanth, D., et al. *Parallelizing two dimensional convex hull on NVIDIA GPU and Cell BE*. in *International conference on high performance computing (HiPC)*. 2009.
81. Rong, G., T.-S. Tan, and T.-T. Cao. *Computing two-dimensional Delaunay triangulation using graphics hardware*. in *Proceedings of the 2008 symposium on Interactive 3D graphics and games*. 2008. ACM.
82. Qi, M., T.-T. Cao, and T.-S. Tan, *Computing 2D constrained Delaunay triangulation using the GPU.* Visualization and Computer Graphics, IEEE Transactions on, 2013. **19**(5): p. 736-748.
83. Kaltofen, E. and L. Yagati, *Improved sparse multivariate polynomial interpolation algorithms*, in *Symbolic and Algebraic Computation*. 1989, Springer. p. 467-474.
84. Cuyt, A. and W.-s. Lee, *A new algorithm for sparse interpolation of multivariate polynomials.* Theoretical Computer Science, 2008. **409**(2): p. 180-185.
85. Vercauteren, T., et al., *Symmetric log-domain diffeomorphic registration: A demons-based approach*, in *Medical Image Computing and Computer-Assisted Intervention–MICCAI 2008*. 2008, Springer. p. 754-761.
86. Vercauteren, T., et al., *Diffeomorphic demons: efficient non-parametric image registration.* Neuroimage, 2009. **45**(1 Suppl): p. S61-72.
87. Kroon, D.-J., *Matlab Central.* Retrieved, 2011. **11**(20): p. 2011.
88. Liu, J.S., *Monte Carlo strategies in scientific computing*. 2008: Springer Science & Business Media.
89. Brock, K., et al., *Accuracy of finite element model-based multi-organ deformable image registration.* Medical physics, 2005. **32**(6): p. 1647-1659.
90. Sharp, G., et al., *GPU-based streaming architectures for fast cone-beam CT image reconstruction and demons deformable registration.* Physics in medicine and biology, 2007. **52**(19): p. 5771.
91. Zhen, X., et al., *Deformable image registration of CT and truncated cone-beam CT for adaptive radiation therapy.* Physics in medicine and biology, 2013. **58**(22): p. 7979.
92. Segars, W., et al., *Realistic CT simulation using the 4D XCAT phantom.* Medical physics, 2008. **35**(8): p. 3800-3808.
93. Segars, W.P. and B.M. Tsui, *MCAT to XCAT: The evolution of 4-D computerized phantoms for imaging research.* Proceedings of the IEEE, 2009. **97**(12): p. 1954-1968.
94. Segars, W., et al., *4D XCAT phantom for multimodality imaging research.* Medical physics, 2010. **37**(9): p. 4902-4915.
95. Lorensen, W.E. and H.E. Cline. *Marching cubes: A high resolution 3D surface construction algorithm*. in *ACM siggraph computer graphics*. 1987. ACM.
96. Ho, C., et al. *Cubical marching squares: Adaptive feature preserving surface extraction from volume data*. in *Computer Graphics Forum*. 2005. Wiley Online Library.
97. Harms Sr, W.B., et al., *A software tool for the quantitative evaluation of 3D dose calculation algorithms.* Medical physics, 1998. **25**(10): p. 1830-1836.
98. Depuydt, T., A. Van Esch, and D.P. Huyskens, *A quantitative evaluation of IMRT dose distributions: refinement and clinical assessment of the gamma evaluation.* Radiotherapy and Oncology, 2002. **62**(3): p. 309-319.
99. Spezi, E. and D.G. Lewis, *Gamma histograms for radiotherapy plan evaluation.* Radiotherapy and oncology, 2006. **79**(2): p. 224-230.

100. Gu, X., X. Jia, and S.B. Jiang, *GPU-based fast gamma index calculation.* Phys Med Biol, 2011. **56**(5): p. 1431-41.
101. Zhen, X., et al., *CT to cone-beam CT deformable registration with simultaneous intensity correction.* Phys Med Biol, 2012. **57**(21): p. 6807-26.
102. Wells, W.M., et al., *Multi-modal volume registration by maximization of mutual information.* Medical image analysis, 1996. **1**(1): p. 35-51.
103. Skouson, M.B., Q. Guo, and Z.-P. Liang, *A bound on mutual information for image registration.* Medical Imaging, IEEE Transactions on, 2001. **20**(8): p. 843-846.
104. Pluim, J.P., J.A. Maintz, and M.A. Viergever, *Mutual-information-based registration of medical images: a survey.* Medical Imaging, IEEE Transactions on, 2003. **22**(8): p. 986-1004.
105. Torkkola, K., *Feature extraction by non parametric mutual information maximization.* The Journal of Machine Learning Research, 2003. **3**: p. 1415-1438.
106. Zhang, L., D. Zhang, and X. Mou, *FSIM: a feature similarity index for image quality assessment.* Image Processing, IEEE Transactions on, 2011. **20**(8): p. 2378-2386.
107. Castillo, R., et al., *A framework for evaluation of deformable image registration spatial accuracy using large landmark point sets.* Physics in medicine and biology, 2009. **54**(7): p. 1849.
108. Leow, A., et al. *Inverse consistent mapping in 3D deformable image registration: its construction and statistical properties*. in *Information Processing in Medical Imaging*. 2005. Springer.
109. Oliveira, F.P. and J.M.R. Tavares, *Medical image registration: a review.* Computer methods in biomechanics and biomedical engineering, 2014. **17**(2): p. 73-93.
110. Liu, Z. and G. Vunjak-Novakovic, *Modeling tumor microenvironments using custom-designed biomaterial scaffolds.* Current Opinion in Chemical Engineering, 2016. **11**: p. 94-105.
111. Weidner, N., et al., *Tumor angiogenesis and metastasis—correlation in invasive breast carcinoma.* New England Journal of Medicine, 1991. **324**(1): p. 1-8.
112. Brannon-Peppas, L. and J.O. Blanchette, *Nanoparticle and targeted systems for cancer therapy.* Advanced drug delivery reviews, 2004. **56**(11): p. 1649-1659.
113. Andreas, K., M. Sittinger, and J. Ringe, *Toward in situ tissue engineering: chemokine-guided stem cell recruitment.* Trends in biotechnology, 2014. **32**(9): p. 483-492.
114. Capeller, B., et al., *Evaluation of tartrate-resistant acid phosphatase (TRAP) 5b as serum marker of bone metastases in human breast cancer.* Anticancer research, 2002. **23**(2A): p. 1011-1015.
115. Byrne, A.T., et al., *Vascular endothelial growth factor-trap decreases tumor burden, inhibits ascites, and causes dramatic vascular remodeling in an ovarian cancer model.* Clinical Cancer Research, 2003. **9**(15): p. 5721-5728.
116. Hu, L., et al., *Vascular endothelial growth factor trap combined with paclitaxel strikingly inhibits tumor and ascites, prolonging survival in a human ovarian cancer model.* Clinical Cancer Research, 2005. **11**(19): p. 6966-6971.
117. Tew, W., et al. *VEGF-Trap for patients (pts) with recurrent platinum-resistant epithelial ovarian cancer (EOC): preliminary results of a randomized, multicenter phase II study*. in *ASCO Annual Meeting Proceedings*. 2007.
118. Tang, L., *Cancer Cell Trap*, 2013, Google Patents.

119. Blehm, B.H., et al., *In vivo optical trapping indicates kinesin's stall force is reduced by dynein during intracellular transport.* Proceedings of the National Academy of Sciences, 2013. **110**(9): p. 3381-3386.
120. Wegman, E.J., S.C. Schwartz, and J.B. Thomas, *Topics in non-Gaussian signal processing*. 2012: Springer Science & Business Media.
121. Ray, P., A.K. Maitra, and A. Basuray. *Entropy-based wavelet de-noising for partial discharge measurement application*. in *2016 IEEE First International Conference on Control, Measurement and Instrumentation (CMI)*. 2016. IEEE.
122. Misiti, M., et al., *Wavelets and their Applications*. 2013: John Wiley & Sons.
123. Alpaydin, E., *Introduction to machine learning*. 2014: MIT press.
124. Schmidhuber, J., *Deep learning in neural networks: An overview.* Neural Networks, 2015. **61**: p. 85-117.
125. Hady, M.F.A. and F. Schwenker, *Semi-supervised learning*, in *Handbook on Neural Information Processing*. 2013, Springer. p. 215-239.
126. LeCun, Y., Y. Bengio, and G. Hinton, *Deep learning.* Nature, 2015. **521**(7553): p. 436-444.
127. Cichocki, A. and R. Unbehauen, *Robust learning algorithm for blind separation of signals.* Electronics Letters, 1994. **30**(17): p. 1386-1387.
128. Szu, H.H., B.A. Telfer, and S.L. Kadambe, *Neural network adaptive wavelets for signal representation and classification.* Optical Engineering, 1992. **31**(9): p. 1907-1916.
129. Kulluk, S., L. Ozbakir, and A. Baykasoglu, *Training neural networks with harmony search algorithms for classification problems.* Engineering Applications of Artificial Intelligence, 2012. **25**(1): p. 11-19.
130. Green, R.C., L. Wang, and M. Alam, *Training neural networks using central force optimization and particle swarm optimization: insights and comparisons.* Expert Systems with Applications, 2012. **39**(1): p. 555-563.
131. Porter, W.A., *Comparative performance of polynomial signal extraction.* Circuits, Systems, and Signal Processing, 1982. **1**(1): p. 93-104.
132. Porter, W.A., *Multiple signal extraction by polynomial filtering.* Mathematical systems theory, 1979. **13**(1): p. 237-254.
133. Yang, X., et al., *Automated segmentation of the parotid gland based on atlas registration and machine learning: a longitudinal MRI study in head-and-neck radiation therapy.* International Journal of Radiation Oncology* Biology* Physics, 2014. **90**(5): p. 1225-1233.
134. Chao, H.-M., D. Chao, and N. Chao, *Methods for volumetric contouring with expert guidance*, 2010, Google Patents.
135. Chen, H.-C., et al., *Automated contouring error detection based on supervised geometric attribute distribution models for radiation therapy: A general strategy.* Medical physics, 2015. **42**(2): p. 1048-1059.
136. Huang, Y.-L. and D.-R. Chen. *Automatic contouring for breast tumors in 2-D sonography*. in *Engineering in Medicine and Biology Society, 2005. IEEE-EMBS 2005. 27th Annual International Conference of the*. 2006. IEEE.
137. Masory, O., *Improving contouring accuracy of NC/CNC systems with additional velocity feed forward loop.* Journal of Manufacturing Science and Engineering, 1986. **108**(3): p. 227-230.

138. Zhang, L., et al., *FSIM: a feature similarity index for image quality assessment.* IEEE Trans Image Process, 2011. **20**(8): p. 2378-86.
139. Lewis, J. *Fast normalized cross-correlation*. in *Vision interface*. 1995.
140. Geroski, D.H. and H.F. Edelhauser, *Drug delivery for posterior segment eye disease.* Investigative ophthalmology & visual science, 2000. **41**(5): p. 961-964.
141. Steinbrook, R., *The price of sight—ranibizumab, bevacizumab, and the treatment of macular degeneration.* New England Journal of Medicine, 2006. **355**(14): p. 1409-1412.
142. Amselem, L., et al., *Intravitreal bevacizumab (Avastin) for choroidal metastasis secondary to breast carcinoma: short-term follow-up.* Eye, 2007. **21**(4): p. 566-567.
143. Kane, F.E., et al., *Iluvien™: a new sustained delivery technology for posterior eye disease.* 2008.
144. Geroski, D.H. and H.F. Edelhauser, *Transscleral drug delivery for posterior segment disease.* Advanced drug delivery reviews, 2001. **52**(1): p. 37-48.
145. Ahmed, I., et al., *Physicochemical determinants of drug diffusion across the conjunctiva, sclera, and cornea.* Journal of pharmaceutical sciences, 1987. **76**(8): p. 583-586.
146. Ahmed, I. and T. Patton, *Importance of the noncorneal absorption route in topical ophthalmic drug delivery.* Investigative ophthalmology & visual science, 1985. **26**(4): p. 584-587.
147. Thrimawithana, T.R., et al., *Drug delivery to the posterior segment of the eye.* Drug discovery today, 2011. **16**(5): p. 270-277.
148. Sanborn, G.E., et al., *Sustained-release ganciclovir therapy for treatment of cytomegalovirus retinitis: use of an intravitreal device.* Archives of Ophthalmology, 1992. **110**(2): p. 188-195.
149. Fortoul, V., P. Denis, and L. Kodjikian, *Anatomical and functional recurrence after dexamethasone intravitreal implants: a 6-month prospective study.* Eye, 2015.
150. Barnes, J., *High performance liquid chromatography*. 1992: John Wiley & Sons.
151. Sparkman, O.D., *Mass spectrometry desk reference.* Journal of the American Society for Mass Spectrometry, 2000. **11**(12): p. 1144.
152. Grulkowski, I., et al., *Retinal, anterior segment and full eye imaging using ultrahigh speed swept source OCT with vertical-cavity surface emitting lasers.* Biomedical optics express, 2012. **3**(11): p. 2733-2751.
153. Witkin, A., et al., *High Speed Ultrahigh Resolution Optical Coherence Tomography of Intraretinal Pigment Epithelium Migration in Non-Exudative Age-Related Macular Degeneration.* Investigative Ophthalmology & Visual Science, 2010. **51**(13): p. 342-342.
154. Coleman, D.J., et al., *High-resolution ultrasonic imaging of the posterior segment.* Ophthalmology, 2004. **111**(7): p. 1344-1351.
155. Jan, M.-L., et al., *A three-dimensional registration method for automated fusion of micro PET-CT-SPECT whole-body images.* Medical Imaging, IEEE Transactions on, 2005. **24**(7): p. 886-893.
156. Christoforidis, J.B., et al., *PET/CT Imaging of I-124–Radiolabeled Bevacizumab and Ranibizumab after Intravitreal Injection in a Rabbit Model.* Investigative ophthalmology & visual science, 2011. **52**(8): p. 5899-5903.
157. Li, S.K., M. J Lizak, and E.K. Jeong, *MRI in ocular drug delivery.* NMR in biomedicine, 2008. **21**(9): p. 941-956.

158. Sakurai, E., et al., *Effect of particle size of polymeric nanospheres on intravitreal kinetics.* Ophthalmic research, 2000. **33**(1): p. 31-36.
159. Yasukawa, T., et al., *Drug delivery systems for vitreoretinal diseases.* Progress in retinal and eye research, 2004. **23**(3): p. 253-281.
160. Kim, H., S.B. Robinson, and K.G. Csaky, *Investigating the movement of intravitreal human serum albumin nanoparticles in the vitreous and retina.* Pharmaceutical research, 2009. **26**(2): p. 329-337.
161. Gargesha, M., et al. *Enhanced volume rendering techniques for high-resolution color cryo-imaging data*. in *SPIE Medical Imaging*. 2009. International Society for Optics and Photonics.
162. Braet, F., et al., *Contribution of high-resolution correlative imaging techniques in the study of the liver sieve in three-dimensions.* Microscopy research and technique, 2007. **70**(3): p. 230-242.
163. Costa, R.r.A., et al., *Optical coherence tomography 3: automatic delineation of the outer neural retinal boundary and its influence on retinal thickness measurements.* Investigative ophthalmology & visual science, 2004. **45**(7): p. 2399-2406.
164. Eroglu, F., et al., *Evaluation of choroidal thickness using enhanced depth imaging by spectral-domain optical coherence tomography in patients with pseudoexfoliation syndrome.* Eye, 2015.
165. Costa, R.A., et al., *Retinal assessment using optical coherence tomography.* Progress in retinal and eye research, 2006. **25**(3): p. 325-353.
166. Pinz, A., et al., *Mapping the human retina.* Medical Imaging, IEEE Transactions on, 1998. **17**(4): p. 606-619.
167. Zignani, M., et al., *A poly (ortho ester) designed for combined ocular delivery of dexamethasone sodium phosphate and 5-fluorouracil: subconjunctival tolerance and in vitro release.* European journal of pharmaceutics and biopharmaceutics, 2000. **50**(2): p. 251-255.
168. Cheng, L., et al., *Treatment or prevention of herpes simplex virus retinitis with intravitreally injectable crystalline 1-O-hexadecylpropanediol-3-phospho-ganciclovir.* Investigative ophthalmology & visual science, 2002. **43**(2): p. 515-521.
169. Ghate, D., et al., *Pharmacokinetics of intraocular drug delivery by periocular injections using ocular fluorophotometry.* Investigative ophthalmology & visual science, 2007. **48**(5): p. 2230-2237.
170. Fritsch, F.N. and R.E. Carlson, *Monotone piecewise cubic interpolation.* SIAM Journal on Numerical Analysis, 1980. **17**(2): p. 238-246.
171. Baghaie, A. and Z. Yu, *Curvature-Based Registration for Slice Interpolation of Medical Images*, in *Computational Modeling of Objects Presented in Images. Fundamentals, Methods, and Applications*. 2014, Springer. p. 69-80.
172. Luo, B. and E. Hancok. *Slice interpolation using the distance transform and morphing*. in *Digital Signal Processing Proceedings, 1997. DSP 97., 1997 13th International Conference on*. 1997. IEEE.
173. Bozkir, G., et al., *Measurements of axial length and radius of corneal curvature in the rabbit eye.* Acta Medica Okayama, 1997. **51**(1): p. 9-11.
174. Ferreiro, A.M.F., et al., *CUSIMANN: An optimized simulated annealing software for GPUs.* 2012.

175. Peura, M., *Computer vision methods for anomaly removal.* Proc. ERAD 2002, 2002: p. 312-317.
176. Chen, Q., et al., *A double-threshold image binarization method based on edge detector.* Pattern recognition, 2008. **41**(4): p. 1254-1267.
177. Siddon, R.L., *Fast calculation of the exact radiological path for a three-dimensional CT array.* Medical physics, 1985. **12**(2): p. 252-255.
178. Lewiner, T., et al., *Efficient implementation of marching cubes' cases with topological guarantees.* Journal of graphics tools, 2003. **8**(2): p. 1-15.
179. Lopes, A. and K. Brodlie, *Improving the robustness and accuracy of the marching cubes algorithm for isosurfacing.* Visualization and Computer Graphics, IEEE Transactions on, 2003. **9**(1): p. 16-29.
180. Cressie, N., *Statistics for spatial data*. 2015: John Wiley & Sons.
181. Hild, F. and S. Roux, *Comparison of local and global approaches to digital image correlation.* Experimental Mechanics, 2012. **52**(9): p. 1503-1519.
182. Plans, P.A., *Completely Randomized Design.*
183. Saville, D.J. and G.R. Wood, *Randomized block design*, in *Statistical Methods: The Geometric Approach*. 1991, Springer. p. 299-339.
184. Montgomery, D.C., G.C. Runger, and N.F. Hubele, *Engineering statistics*. 2009: John Wiley & Sons.
185. Patel, V. and K. Mistree, *A review on different image interpolation techniques for image enhancement.* IJETAE, 2013. **3**: p. 129-33.
186. Sarfraz, M., M.Z. Hussain, and M. Hussain, *Shape-preserving curve interpolation.* International Journal of Computer Mathematics, 2012. **89**(1): p. 35-53.
187. Hammer, R., et al., *C++ Toolbox for Verified Computing I: Basic Numerical Problems Theory, Algorithms, and Programs*. 2012: Springer Science & Business Media.
188. Cuda, C., *Programming guide*, 2012.
189. Birkner, M., et al., *Adapting inverse planning to patient and organ geometrical variation: algorithm and implementation.* Med Phys, 2003. **30**(10): p. 2822-31.
190. Wu, Q.J., et al., *Adaptive radiation therapy: technical components and clinical applications.* Cancer J, 2011. **17**(3): p. 182-9.
191. Hatton, J., B. McCurdy, and P.B. Greer, *Cone beam computerized tomography: the effect of calibration of the Hounsfield unit number to electron density on dose calculation accuracy for adaptive radiation therapy.* Phys Med Biol, 2009. **54**(15): p. N329-46.
192. Niu, T. and L. Zhu, *Scatter correction for full-fan volumetric CT using a stationary beam blocker in a single full scan.* Med Phys, 2011. **38**(11): p. 6027-38.
193. Yoo, S. and F.F. Yin, *Dosimetric feasibility of cone-beam CT-based treatment planning compared to CT-based treatment planning.* Int J Radiat Oncol Biol Phys, 2006. **66**(5): p. 1553-61.
194. Yang, Y., et al., *Evaluation of on-board kV cone beam CT (CBCT)-based dose calculation.* Phys Med Biol, 2007. **52**(3): p. 685-705.
195. Reeves, T.E., P. Mah, and W.D. McDavid, *Deriving Hounsfield units using grey levels in cone beam CT: a clinical application.* Dentomaxillofac Radiol, 2012. **41**(6): p. 500-8.
196. Chao, M., Y. Xie, and L. Xing, *Auto-propagation of contours for adaptive prostate radiation therapy.* Phys Med Biol, 2008. **53**(17): p. 4533-42.

197. Samant, S.S., et al., *High performance computing for deformable image registration: towards a new paradigm in adaptive radiotherapy.* Med Phys, 2008. **35**(8): p. 3546-53.
198. Xie, Y., et al., *Feature-based rectal contour propagation from planning CT to cone beam CT.* Med Phys, 2008. **35**(10): p. 4450-9.
199. Siewerdsen, J.H. and D.A. Jaffray, *Cone-beam computed tomography with a flat-panel imager: magnitude and effects of x-ray scatter.* Med Phys, 2001. **28**(2): p. 220-31.
200. Siewerdsen, J.H., et al., *A simple, direct method for x-ray scatter estimation and correction in digital radiography and cone-beam CT.* Med Phys, 2006. **33**(1): p. 187-97.
201. Rinkel, J., et al., *A new method for x-ray scatter correction: first assessment on a cone-beam CT experimental setup.* Phys Med Biol, 2007. **52**(15): p. 4633-52.
202. Maltz, J.S., et al., *Algorithm for X-ray scatter, beam-hardening, and beam profile correction in diagnostic (kilovoltage) and treatment (megavoltage) cone beam CT.* IEEE Trans Med Imaging, 2008. **27**(12): p. 1791-810.
203. Zhu, L., et al., *Scatter correction for cone-beam CT in radiation therapy.* Med Phys, 2009. **36**(6): p. 2258-68.
204. Sun, M., et al., *Correction for patient table-induced scattered radiation in cone-beam computed tomography (CBCT).* Med Phys, 2011. **38**(4): p. 2058-73.
205. Ou, W., and Christophe Chefd'Hotel, *Polynomial intensity correction for multimodal image registration.* IEEE Trans Med Imaging, 2009. **Biomedical Imaging: From Nano to Macro**(IEEE International Symposium on. IEEE, 2009).
206. Guimond, A., et al., *Three-dimensional multimodal brain warping using the demons algorithm and adaptive intensity corrections.* IEEE Trans Med Imaging, 2001. **20**(1): p. 58-69.
207. Hou, J., et al., *Deformable planning CT to cone-beam CT image registration in head-and-neck cancer.* Medical Physics, 2011. **38**(4): p. 2088.
208. Nithiananthan, S., et al., *Demons deformable registration of CT and cone-beam CT using an iterative intensity matching approach.* Medical Physics, 2011. **38**(4): p. 1785.
209. Lawson, J.D., et al., *Quantitative evaluation of a cone-beam computed tomography-planning computed tomography deformable image registration method for adaptive radiation therapy.* J Appl Clin Med Phys, 2007. **8**(4): p. 2432.
210. Elstrom, U.V., et al., *Daily kV cone-beam CT and deformable image registration as a method for studying dosimetric consequences of anatomic changes in adaptive IMRT of head and neck cancer.* Acta Oncol, 2010. **49**(7): p. 1101-8.
211. Lou, Y., et al., *Joint CT/CBCT deformable registration and CBCT enhancement for cancer radiotherapy.* Med Image Anal, 2013. **17**(3): p. 387-400.
212. Kim, J., et al., *A novel approach for establishing benchmark CBCT/CT deformable image registrations in prostate cancer radiotherapy.* Phys Med Biol, 2013. **58**(22): p. 8077-97.
213. Kim, J., et al., *Prostate localization on daily cone-beam computed tomography images: accuracy assessment of similarity metrics.* Int J Radiat Oncol Biol Phys, 2010. **77**(4): p. 1257-65.
214. Gu, X., et al., *A contour-guided deformable image registration algorithm for adaptive radiotherapy.* Phys Med Biol, 2013. **58**(6): p. 1889-901.
215. Schreibmann, E. and L. Xing, *Image registration with auto-mapped control volumes.* Med Phys, 2006. **33**(4): p. 1165-79.

216. Gu, X., et al., *Implementation and evaluation of various demons deformable image registration algorithms on a GPU.* Phys Med Biol, 2010. **55**(1): p. 207-19.
217. Schreiner, J., C.E. Scheidegger, and C.T. Silva, *High-quality extraction of isosurfaces from regular and irregular grids.* IEEE Trans Vis Comput Graph, 2006. **12**(5): p. 1205-12.
218. Yang, J.H., C.S. Kim, and S.U. Lee, *Semi-regular representation and progressive compression of 3-D dynamic mesh sequences.* IEEE Trans Image Process, 2006. **15**(9): p. 2531-44.
219. Ogawa, T. and M. Haseyama, *Missing intensity interpolation using a kernel PCA-based POCS algorithm and its applications.* IEEE Trans Image Process, 2011. **20**(2): p. 417-32.
220. Bolz, J., Ian Farmer, Eitan Grinspun, and Peter Schröoder, *Sparse matrix solvers on the GPU: conjugate gradients and multigrid.* In ACM Transactions on Graphics (TOG), 2003. **22**(3): p. 917-924.
221. Correa, C.D., Deborah Silver, and Min Chen. , *Volume deformation via scattered data interpolation.* Proceedings of the Sixth Eurographics/Ieee, 2007. **VGTC conference on Volume Graphics.**(Eurographics Association).
222. Wang, H., et al., *Validation of an accelerated 'demons' algorithm for deformable image registration in radiation therapy.* Phys Med Biol, 2005. **50**(12): p. 2887-905.
223. Rogelj, P. and S. Kovacic, *Symmetric image registration.* Med Image Anal, 2006. **10**(3): p. 484-93.
224. Li, T., Xiang Li, Jing Wang, Junhai Wen, Hongbing Lu, Jiang Hsieh, and Zhengrong Liang, *Nonlinear sinogram smoothing for low-dose X-ray CT.* Nuclear Science, IEEE Transactions, 2004. **5**(51): p. 2505-2513.
225. Wang, J., et al., *Penalized weighted least-squares approach to sinogram noise reduction and image reconstruction for low-dose X-ray computed tomography.* IEEE Trans Med Imaging, 2006. **25**(10): p. 1272-83.
226. Pratx, G. and L. Xing, *GPU computing in medical physics: a review.* Med Phys, 2011. **38**(5): p. 2685-97.
227. Naumov, M., *Incomplete-LU and Cholesky preconditioned iterative methods using CUSPARSE and CUBLAS.* Nvidia white paper, 2011.
228. Montanari, D., et al., *Comprehensive evaluations of cone-beam CT dose in image-guided radiation therapy via GPU-based Monte Carlo simulations.* Phys Med Biol, 2014. **59**(5): p. 1239-53.
229. Jia, X., P. Ziegenhein, and S.B. Jiang, *GPU-based high-performance computing for radiation therapy.* Phys Med Biol, 2014. **59**(4): p. R151-82.
230. Townson, R.W., et al., *GPU-based Monte Carlo radiotherapy dose calculation using phase-space sources.* Phys Med Biol, 2013. **58**(12): p. 4341-56.
231. Jia, X., et al., *A GPU tool for efficient, accurate, and realistic simulation of cone beam CT projections.* Med Phys, 2012. **39**(12): p. 7368-78.
232. Jia, X., et al., *GPU-based fast Monte Carlo dose calculation for proton therapy.* Phys Med Biol, 2012. **57**(23): p. 7783-97.
233. Jia, X., et al., *GPU-based fast Monte Carlo simulation for radiotherapy dose calculation.* Phys Med Biol, 2011. **56**(22): p. 7017-31.
234. Jia, X., et al., *GPU-based iterative cone-beam CT reconstruction using tight frame regularization.* Phys Med Biol, 2011. **56**(13): p. 3787-807.

235. Jia, X., et al., *GPU-based fast low-dose cone beam CT reconstruction via total variation.* J Xray Sci Technol, 2011. **19**(2): p. 139-54.
236. Gu, X., et al., *A GPU-based finite-size pencil beam algorithm with 3D-density correction for radiotherapy dose calculation.* Phys Med Biol, 2011. **56**(11): p. 3337-50.
237. Men, C., X. Jia, and S.B. Jiang, *GPU-based ultra-fast direct aperture optimization for online adaptive radiation therapy.* Phys Med Biol, 2010. **55**(15): p. 4309-19.
238. Jia, X., et al., *Development of a GPU-based Monte Carlo dose calculation code for coupled electron-photon transport.* Phys Med Biol, 2010. **55**(11): p. 3077-86.
239. Jia, X., et al., *GPU-based fast cone beam CT reconstruction from undersampled and noisy projection data via total variation.* Med Phys, 2010. **37**(4): p. 1757-60.
240. Men, C., et al., *GPU-based ultrafast IMRT plan optimization.* Phys Med Biol, 2009. **54**(21): p. 6565-73.
241. Tewarson, R.P., *Sparse matrices*. 1973: Academic Press.
242. Pissanetzky, S., *Sparse Matrix Technology-electronic edition*. 1984: Academic Press.
243. Lester, H. and S.R. Arridge, *A survey of hierarchical non-linear medical image registration.* Pattern recognition, 1999. **32**(1): p. 129-149.
244. Maintz, J.A. and M.A. Viergever, *A survey of medical image registration.* Medical image analysis, 1998. **2**(1): p. 1-36.
245. Trier, Ø.D., A.K. Jain, and T. Taxt, *Feature extraction methods for character recognition-a survey.* Pattern recognition, 1996. **29**(4): p. 641-662.